Development and Characterization of NiTi Joining Methods and Metal Matrix Composite Transducers with Embedded NiTi by Ultrasonic Consolidation

A Thesis

Presented in Partial Fulfillment of the Requirements for

the Degree Master of Science in the

Graduate School of The Ohio State University

By

Ryan M. Hahnlen, B.S.

* * * * *

The Ohio State University

2009

Master's Examination Committee:

Dr. Marcelo Dapino, Adviser

Dr. Somnath Ghosh

Approved by

____

Adviser

Graduate Program in
Mechanical Engineering

© Copyright by

Ryan M. Hahnlen

2009

ABSTRACT

Nickel-Titanium (NiTi) is a shape memory alloy that, depending upon composition, can exhibit shape memory or superelastic properties, recovering up to 8% deformation. Utilizing the shape memory effect it is possible to use NiTi as an actuator replacing traditional mechanical systems with a light-weight system using a fewer number of moving parts. In addition to strain recovery, NiTi undergoes significant changes in its material properties, including elastic modulus and electrical resistivity. With these changes in material properties, it is possible to create NiTi based transducers. Currently, NiTi is limited to niche applications due primarily to difficulty in machining and joining NiTi to traditional structural materials.

The goal of this thesis is to develop and characterize consistent methods of creating adaptive structures using NiTi. The research presented consists of two parts; the first deals with the development and characterization of cost-effective methods of joining NiTi and common aluminum and steel alloys. Laser welding, tungsten inert gas welding, and ultrasonic soldering were used to create joints between NiTi and itself, aluminum 2024, O1 tool steel, and 304 stainless steel. Where applicable, joints were subject to mechanical testing and analysis using optical microscopy.

The second part explores the development and characterization of NiTi/Al metal matrix composite transducers constructed using Ultrasonic Additive Manufacturing

(UAM), a low temperature solid-state process also referred to as ultrasonic consolidation. An aluminum UAM matrix was first characterized through mechanical testing and analysis using optical microscopy. Using UAM, aluminum matrix composites with embedded NiTi wires were created with up to a 13.4% NiTi cross sectional area ratio. The composites were tested to characterize their stiffness as a function of temperature. A model was also developed using the Brinson constitutive model in order to predict the stiffness and strain sensing properties of current and future UAM NiTi/Al composites.

ACKNOWLEDGMENTS

I would like to begin by acknowledging those who have helped me reach where I am. Without the efforts of many others, I would not have been able to reach this point in my academic career. I would first like to thank my advisor, Professor Marcelo Dapino, for giving me the opportunity to work on such fascinating and rewarding projects. I would also like to thank Professor Somnath Ghosh for serving on my exam committee.

This research would not have been possible without Dr. Karl Graff, Matt Short, and Tim Frech from the Edison Welding Institute as well as Dr. Tad Calkins and Jim Mabe from the Boeing Company. Close collaboration with these companies has been possible thanks to the Smart Vehicle Concept center (www.smartvehiclecenter.org), a National Science Foundation Industry & University Collaborative Research Center. I would also like to thank the SVC for providing my funding through a fellowship and the SVC industrial advisory board for their continued support of this research.

To my colleagues at the Smart Materials and Structures Lab, thank you for your help, advice, and friendship. To Neil Gardner in the student machine shop, thanks for all your machining and motorcycle advice. Also I'd like to thank Professor Babu and David Schick, from the OSU welding engineering department, for their assistance with and explanation of material and metallurgical concerns during the course of this research.

I would not have been successful in my endeavors without the love and support of my family. To my brother and sister, grandparents, aunts, uncles, and cousins, thank you for your support, nurturing, and for helping to make me who I am today. Special thanks go to my fiancée, Marie, for her support and encouragement during my graduate studies. Most importantly, I thank my parents, Bill and Kyle, for raising me, encouraging me to be inquisitive, supporting all that I do, and much, much more. Thank you.

VITA

June 8, 1984	Born - Toledo, Ohio
June 2002	Honors Diploma, Maumee High School
June 2007	B.S. Mechanical Engineering Cum Laude, The Ohio State University
2008 - Present	NSF I/UCRC Smart Vehicle Concepts Center Fellow, The Ohio State University

FIELDS OF STUDY

Major Field: Mechanical Engineering

Studies in Smart Materials and Structures: Dr. Marcelo Dapino

Major Field: Mechanical Engineering

TABLE OF CONTENTS

Page

Abstract ii

Acknowledgments iv

Vita vi

List of Tables xi

List of Figures xiii

Chapters:

1. Introduction 1

    1.1 Thesis Organization 1
    1.2 Shape Memory Alloys 2
    1.3 NiTi Machining and Joining Issues 8
    1.4 Joining Techniques 11
        1.4.1 Laser Welding 11
        1.4.2 Tungsten Inert Gas (TIG) Welding 12
        1.4.3 Ultrasonic Soldering (USS) 13
    1.5 Ultrasonic Additive Manufacturing (UAM) 14

2. Joining of NiTi and Structural Materials 22

    2.1 Joint Characterization Methods 22
        2.1.1 Laser Welding 22
        2.1.2 Tungsten Inert Gas (TIG) Welding 23
        2.1.3 Ultrasonic Soldering (USS) 27
    2.2 Joint Characterization Results 39

    2.2.1 Laser Welding 39
    2.2.2 Tungsten Inert Gas (TIG) Welding 41
    2.2.3 Ultrasonic Soldering (USS) 42
  2.3 Discussion of Results 50
    2.3.1 Laser Welding 50
    2.3.2 Tungsten Inert Gas (TIG) Welding 53
    2.3.3 Ultrasonic Soldering (USS) 53

3. NiTi/Al Composites by Ultrasonic Consolidation 64

  3.1 Ultrasonic Additive Manufacturing (UAM) Composite Characterization Methods 64
    3.1.1 Al 3003 H-18 Matrix 64
    3.1.2 Nickel-Titanium 70
    3.1.3 NiTi/Al Composite 71
  3.2 Ultrasonic Additive Manufacturing (UAM) Composite Characterization Results 75
    3.2.1 Al 3003 H-18 Matrix 75
    3.2.2 Nickel-Titanium 78
    3.2.3 NiTi/Al Composite 80
  3.3 Ultrasonic Additive Manufacturing (UAM) NiTi/Al Composite Modeling 81
    3.3.1 Constitutive Modeling 81
    3.3.2 NiTi Wire Modeling 86
    3.3.3 Composite Sensing 88
    3.3.4 Composite Stiffness 90
  3.4 Discussion of Results 91
    3.4.1 UAM Composite Characterization 91
    3.4.2 UAM Composite Modeling 101

4. Conclusions and Future Work 107

  4.1 Laser Welding 107
  4.2 Tungsten Inert Gas Welding 108
  4.3 Ultrasonic Soldering 109
  4.4 Ultrasonic Additive Manufacturing 110
    4.4.1 Matrix Characterization 110
    4.4.2 Active Composites 110

Appendices:

A. Fixture, Sample, and Testing Jig Drawings 112

B. NiTi/304 SS Laser Weld Section Micrographs 130

C. USS Force versus Displacement Plots 137

D. UAM Force versus Displacement Plots 145

Bibliography 149

LIST OF TABLES

Table **Page**

2.1 NiTi/304 SS Laser Weld Parameters. 24

2.2 Laser weld penetration and cracking. 40

2.3 SonicSolder^{TM} tensile test results. 43

2.4 Al 2024/Al 2024 lap shear test results. 45

2.5 O1/O1 tool steel lap shear test results. 45

2.6 304 SS/304 SS lap shear test results. 45

2.7 NiTi lap shear test results. 47

2.8 Equivalent stresses in Al 2024 lap shear tests. 55

2.9 Equivalent stresses in O1 tool steel lap shear tests. 55

2.10 Equivalent stresses in 304 SS lap shear tests. 55

2.11 Equivalent stresses in NiTi containing lap shear tests. 58

2.12 Material properties used to calculate thermally induced stresses in USS joints. 60

2.13 Thermally induced stresses in NiTi containing USS lap shear joints. 60

3.1 UAM process parameters for matrix mechanical testing samples. . . 65

3.2 1-1 UAM specimen testing results. 75

3.3 3-2 UAM specimen testing results. 77

3.4 1-2 UAM specimen testing results. 78

3.5 UAM bond area as determined by fracture surface analysis. 82

3.6 Material properties of 90 °C Flexinol as derived from experiment. . . 82

3.7 UAM active composite stiffness test results. 83

3.8 Additional material properties used for sensing and stiffness models. 87

3.9 Distance of failure surface from top, samples 3 and 6 not statistically considered. 95

3.10 Comparison of Al 3003-H18 UAM matrix and solid Al 3003-H18 strength. 97

LIST OF FIGURES

Figure **Page**

1.1 Twinned martensite reorienting under stress to create detwinned martensite. 3

1.2 The transformation between austenite and twinned martensite has no associated strain or shape change. 3

1.3 The application of stress to twinned martensite produces a residual strain which is recovered when the NiTi transforms to austenite. . . 4

1.4 Schematic representation of martensitic volume fraction as a function of temperature. 5

1.5 Effect of stress on transition temperatures. 6

1.6 Stress-strain curve displaying the shape memory effect and residual strain. 7

1.7 Superelastic stress strain curve. 8

1.8 Fusion weld of NiTi and SS alloy exhibiting cold cracking in the weld [10]. 10

1.9 Schematic representation of the laser welding process. 12

1.10 Schematic representation of the ultrasonic soldering process. 14

1.11 Schematic representation of ultrasonic metal welding, a solid-state joining process which forms the basis for UAM. 15

1.12 In the UAM process, successive layers of metal tape are bonding together for creating metallic composites with seamlessly embedded materials and features. 16

1.13 Ultrasonic transducer, booster, and horn system, tape feed mechanism, and integrated CNC mill. 17

1.14 (a) Micrograph of 0.004" (100 μm) diameter sigma fibers embedded in aluminum [17]. (b) Aluminum UAM build with embedded copper block. (c) Fiber optics embedded between aluminum tapes. (d) An X-ray image of a UAM build with arbitrary multi-level internal channels made using subtractive processes. (Photographs (b) and (c) courtesy of Solidica, Inc., Image (d) courtesy of EWI) 19

1.15 Micrograph of 0.003" (75 μm) diameter shape memory NiTi wire fully embedded in Al 3003-H18 UAM matrix utilizing only plastic flow of the matrix material. 20

1.16 The 10 kW UAM test bed system at EWI has increased embedding capabilities. 21

2.1 (a) Cutaway diagram of assembled 304 SS/NiTi tube sample; (b) Photograph of assembled sample before welding. 23

2.2 Diagram of prepared 304 SS plate for TIG welding to NiTi. 25

2.3 Prepared NiTi and 304 SS plates before TIG welding. 25

2.4 EDM pattern for cutting tensile samples from 304 SS/NiTi TIG weld, all dimensions in inches. 26

2.5 Bulk SonicSolder^{TM} tensile specimens. 27

2.6 Dimensions for SonicSolder^{TM} shear specimen, all dimensions in inches. 28

2.7 (a)Diagram of compressive shear testing jig; (b) Shear test photograph. 29

2.8 Diagram of USS lap shear specimen. 31

2.9 Al 2024/Al 2024 USS lap shear specimen. 31

2.10 O1 tool steel/O1 tool steel USS lap shear specimen. 32

2.11 304 SS/304 SS USS lap shear specimen. 32

2.12 NiTi/NiTi USS lap shear specimen. 33

2.13 NiTi/Al 2024 USS lap shear specimen. 33

2.14 NiTi/O1 tool steel USS lap shear specimen. 34

2.15 NiTi/304 SS USS lap shear specimen. 34

2.16 NiTi tube and Al 2024 saddles used to create NiTi/Al 2024 torsion sample. 36

2.17 USS NiTi/Al 2024 torsion sample cooling jig (a) saddle alignment portion and (b) saddle spacing gauge. 37

2.18 (a) First NiTi/Al 2024 USS torsion sample with symmetric saddles; (b) Second NiTi/Al 2024 USS torsion samples with extended saddles. 37

2.19 Torsion testing adapters for USS NiTi/Al 2024 torsion specimens. . 38

2.20 NiTi/304 SS laser weld 2. 40

2.21 NiTi/304 SS TIG weld 1. 41

2.22 NiTi/304 SS TIG weld 2. 42

2.23 Bulk SonicSolder^{TM} tensile sample 6 force versus displacement test. 43

2.24 Bulk SonicSolder^{TM} shear sample force versus displacement test. . . 44

2.25 Al2024/Al 2024 USS shear sample 4 showing void areas. 46

2.26 USS torsion sample 1 torque versus angular displacement test 1. . . 48

2.27 Deformed NiTi/Al 2024 torsion specimen after testing. 48

2.28 USS torsion sample 1 torque versus angular displacement test 2. . . 49

2.29 USS torsion sample 2 torque versus angular displacement test. . . . 49

2.30 USS NiTi/Al 2024 joint cross section. 50

2.31 USS NiTi/Al 2024 joint cross section. 51

2.32 Laser weld section showing cracks due to misalignment of NiTi and 304 SS tube walls due to eccentricity in the outer and inner diameters of the 304 SS. 52

2.33 Differential element of solder in USS lap shear joints. 54

2.34 Differential element of solder in USS torsion joints. 61

3.1 UAM sample identification convention. 65

3.2 Tape and load orientation of 1-1 UAM samples. 66

3.3 UAM 1-1 samples (a) nominal dimensions and (b) reduced shear area modified in anticipation of high shear strength of UAM bond. 67

3.4 Tape and load orientation of 3-2 UAM samples. 68

3.5 3-2 UAM test specimen. 68

3.6 Tape and load orientation of 1-2 UAM samples. 69

3.7 1-2 UAM test specimen. 69

3.8 UAM embedded wire grips holding and alignment plate. 72

3.9 UAM embedding baseplate with sacrificial baseplate and NiTi wire grips. 72

3.10 UAM NiTi/Al 6061 composite with eight embedded 0.004" diameter NiTi wires. 73

3.11 UAM NiTi/Al 6061 composite with six embedded 0.008" diameter NiTi wires. 73

3.12 UAM NiTi/Al 6061 composite dog bone sample with 4.5% NiTi cross sectional area ratio. 74

3.13 UAM 1-1 sample 1 force versus displacement test plot. 76

3.14 UAM 3-2 sample 4 force versus displacement test plot. 77

3.15 UAM 1-2 sample 1 force versus displacement test plot. 79

3.16 UAM 3-2 sample 8 fracture surface before image processing, dark regions are previously bonded regions. 80

3.17 UAM 3-2 sample 8 fracture surface after image processing, red regions are bond fracture surfaces. 81

3.18 NiTi wire change in resistance versus temperature for (a) an unloaded wire and (b) a wire under a 2.7 lbs axial load. 83

3.19 NiTi wire model change in resistance versus temperature for (a) 0 lbs axial load and (b) 2.7 lbs axial load. 88

3.20 NiTi/Al UAM composite sensing model for (a) 4.5% NiTi area ratio and (b) 13.4% NiTi area ratio. 89

3.21 NiTi/Al UAM composite stiffness model for (a) 4.5% NiTi area ratio and (b) 13.4% NiTi area ratio. 91

3.22 Failure surfaces of (a) UAM 1-1 sample and (b) solid Al 3003-H14 sample. 92

3.23 UAM 3-2 sample 6 showing an atypical fracture surface pattern. . . 94

3.24 UAM 3-2 samples showing similar failure locations. 95

3.25 UAM 1-2 sample failure showing necking at gauge length. 96

3.26 The UAM horn textures the top surface of each tape leaving the bottom surface to be deformed through plastic deformation due to discrete contact with the mating tape below. This intimate contact leads to bonding. 98

3.27 UAM 3-2 sample fracture surface showing plastic deformation and mill striations. 99

3.28 Bottom fracture surface of UAM 1-1 sample 1 showing nearly complete surface deformation due to contact with the horn. 100

3.29 Voids in UAM samples are fracture initiation sites resulting in (a) mode I fracture in 3-2 samples and (b) mode II fracture in 1-1 samples.101

3.30 Solid Al 6061 stiffness model compared to calculated stiffness of NiTi/Al UAM (a) 4.5% NiTi area ratio composite and (b) 13.4% NiTi area ratio composite. 104

A.1 Ultrasonic soldering fixture used to create consistent USS joints with a nominal thickness of 0.003”. 113

A.2 Bottom half of USS torsion sample cooling fixture. 114

A.3 Top half of USS torsion sample cooling fixture. 115

A.4 Nominal dimensions for reduced area UAM 1-1 samples. 116

A.5 Nominal dimensions for bulk shear sample, lap shear samples, and UAM 1-1 samples. 117

A.6 Nominal dimensions for UAM 3-2 samples. 118

A.7 Nominal dimensions for UAM 1-2 samples. 119

A.8 USS Al 2024 torsion short saddle. 120

A.9 USS NiTi/Al 2024 torsion sample with short saddles. 121

A.10 USS Al 2024 torsion long saddle. 122

A.11 USS NiTi/Al 2024 torsion sample with long saddles. 123

A.12 Tensile test bottom grip use for bulk solder and UAM 3-2 tests. . . 124

A.13 Tensile test bottom grip use for bulk solder and UAM 3-2 tests. . . 125

A.14 Shear testing jig back half used for bulk solder, USS lap shear, and UAM tests. 126

A.15 Shear testing jig front half used for bulk solder, USS lap shear, and UAM tests. 127

A.16 Shear testing jig, insert used to ensure proper fit of shear sample. . . 128

A.17 Torsion testing grip adapter for USS torsion samples. 129

B.1 Laser weld sample 1a micrograph. 131

B.2 Laser weld sample 1b micrograph. 131

B.3 Laser weld sample 2a micrograph. 132

B.4 Laser weld sample 2b micrograph. 132

B.5 Laser weld sample 3a micrograph. 133

B.6 Laser weld sample 3b micrograph. 133

B.7 Laser weld sample 4a micrograph. 134

B.8 Laser weld sample 4b micrograph. 134

B.9 Laser weld sample 5a micrograph. 135

B.10 Laser weld sample 5b micrograph. 135

B.11 Laser weld sample 6a micrograph. 136

B.12 Laser weld sample 6b micrograph. 136

C.1 Solid SonicSolder^{TM} force versus displacement sample comparison plots.137

C.2 Solid SonicSolder^{TM} shear sample force versus displacement plot. . . 138

C.3 USS Al 2024 lap shear force versus displacement comparison plots. No surface treatment. 138

C.4 USS Al 2024 lap shear force versus displacement comparison plots. Joined after 50 μm SiC grit blast and methanol rinse. 139

C.5 USS O1 tool steel lap shear force versus displacement comparison plots. No surface treatment. 139

C.6 USS O1 tool steel lap shear force versus displacement comparison plots. Joined after 50 μm SiC grit blast and methanol rinse. 140

C.7 USS 304 SS lap shear force versus displacement comparison plots. No surface treatment. 140

C.8 USS 304 SS lap shear force versus displacement comparison plots. Joined after 50 μm SiC grit blast and methanol rinse. 141

C.9 USS NiTi/Al 2024 lap shear force versus displacement comparison plots. Joined after 50 μm SiC grit blast and methanol rinse. 141

C.10 USS NiTi/O1 tool steel lap shear force versus displacement comparison plots. Joined after 50 μm SiC grit blast and methanol rinse. . . 142

C.11 USS NiTi/304 SS lap shear force versus displacement comparison plots. Joined after 50 μm SiC grit blast and methanol rinse. 142

C.12 USS NiTi/Al 2024 torsion joint 1 angular displacement versus torque plot 1. 143

C.13 USS NiTi/Al 2024 torsion joint 1 angular displacement versus torque plot 2. 143

C.14 USS NiTi/Al 2024 torsion joint 2 angular displacement versus torque plot. 144

D.1 UAM 1-1 sample 1 force versus displacement plot. 145

D.2 UAM 1-1 sample 2 force versus displacement plot. 146

D.3 UAM 1-1 sample 3 force versus displacement plot. 146

D.4 UAM 1-1 sample 4 force versus displacement plot. 147

D.5 UAM 3-2 force versus displacement sample comparison plots. 147

D.6 UAM 1-2 force versus displacement sample comparison plots. 148

CHAPTER 1

INTRODUCTION

1.1 Thesis Organization

The following thesis is divided into two parts. The first part investigates the joining of shape memory NiTi to aluminum 2024 (Al 2024), O1 tool steel, and 304 stainless steel (304 SS). The joining methods investigated include laser welding, Tungsten Inert Gas (TIG) welding, and Ultrasonic Soldering (USS). Section 2.1 discusses the sample construction and joint characterization methods. Section 2.2 give the results of characterization efforts which are further discussed in section 2.3.

The second part investigates the development and characterization of NiTi/Al composites using Ultrasonic Additive Manufacturing (UAM), a new solid state process that uses ultrasonic metal welding to create metal parts and metal matrix composites. Section 3.1 describes the samples created and the experiments performed for characterization of the Al matrix, embedded NiTi, and NiTi/Al active composites. Section 3.2 gives the results of UAM characterization efforts. Modeling of the NiTi, the NiTi/Al composite sensing properties, and NiTi/Al composite stiffness is discussed in section 3.3. Section 3.4 discusses the results of UAM characterization efforts and compares experimental and modeling results.

Section 4 summarizes results from both parts and discusses future work for the development and characterization for NiTi joining methods and UAM composite NiTi/Al transducers.

1.2 Shape Memory Alloys

Shape Memory Alloys (SMAs) are a class of smart materials that can be plastically deformed and then recover their original shape upon heating above the material's austenitic finish temperature. NiTi is a particular shape memory alloy that can be strained up to 8% and fully recover all deformation [24]. The ability to recover large amounts of strain is due to the crystalline structure of the alloy transforming between its two phases, martensite and austenite. When in its martensitic phase, NiTi can take on two general forms, self accommodating, or "twinned", martensite and "detwinned" martensite.

Both martensitic forms have monoclinic crystalline structures, however in the twinned form, the crystals form a lattice of alternating monoclinic orientations. With the application of stress, the twinned structure detwins as the individual crystals reorient to lie in the same direction, as seen in Figure 1.1.

The austenite phase of NiTi consists of cubic crystalline structures. NiTi fully transforms into austenite when it is subjected to temperatures above its austenitic finish temperature, denoted A_f. When transforming between the twinned martensite variant and austenite phases, there is no net shape change or strain recovery in the bulk material, Figure 1.2, however when the detwinned martensite variant is heated above A_f, strain from the initial detwinning of martensite is recovered as it transforms into austenite. With no applied stress, as the temperature falls below the martensite

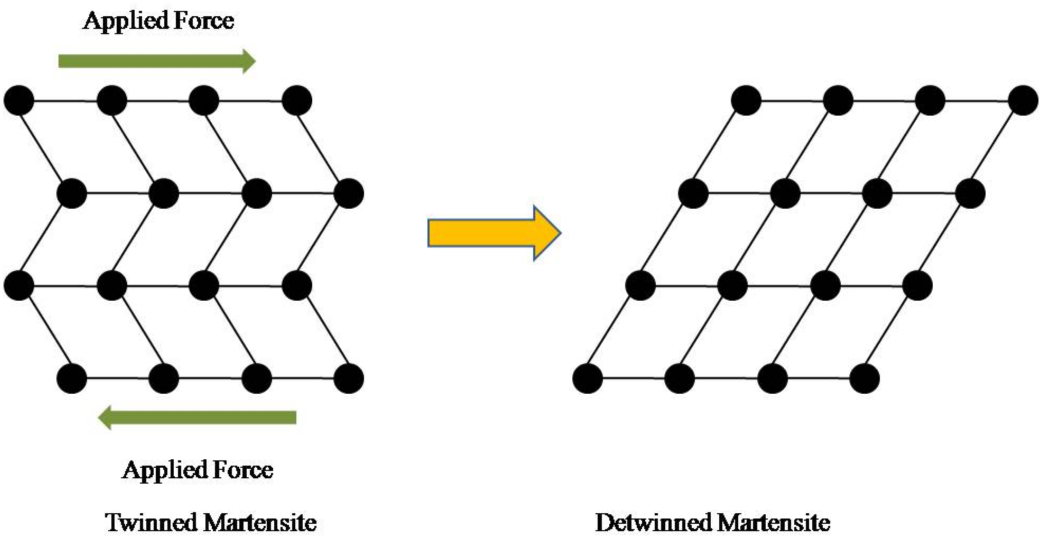
Applied Force
Applied Force
Twinned Martensite
Detwinned Martensite

Figure 1.1: Twinned martensite reorienting under stress to create detwinned martensite.

finish temperature, M_f, the cubic austenite phase is fully transformed into the twinned variant of martensite, as illustrated in Figure 1.3.

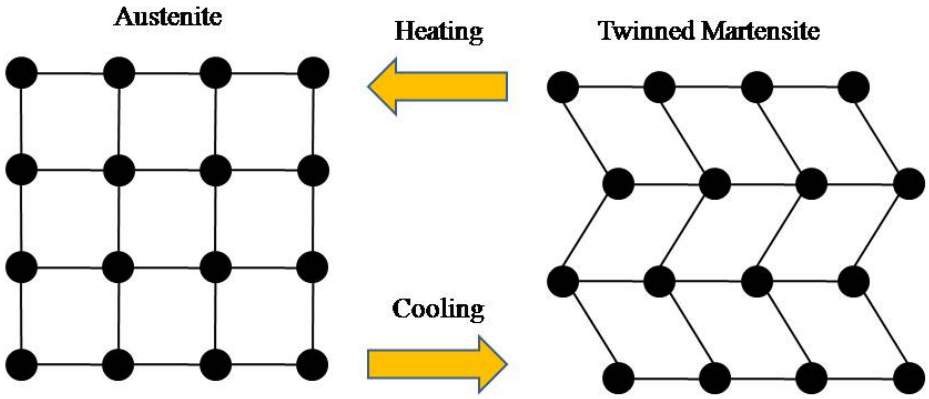
Austenite
Heating
Twinned Martensite
Cooling

Figure 1.2: The transformation between austenite and twinned martensite has no associated strain or shape change.

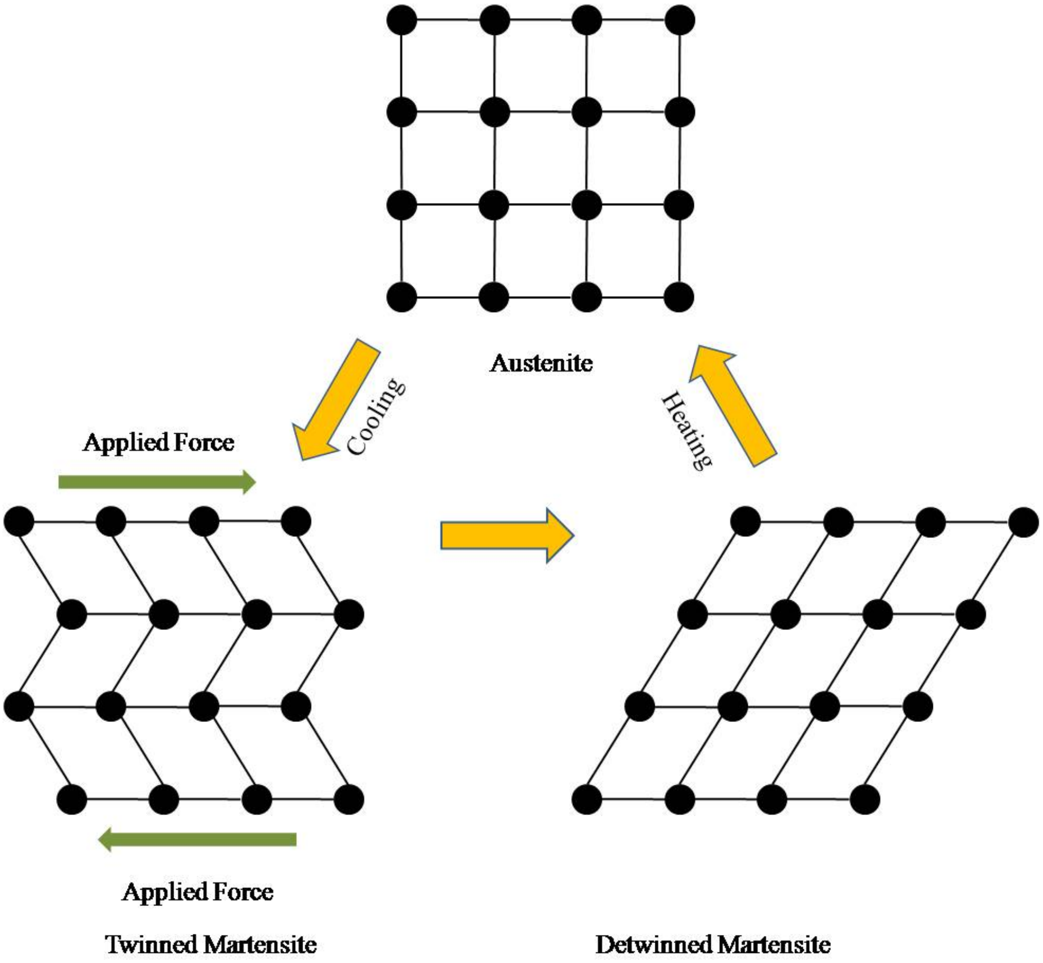
Austenite
Cooling
Heating
Applied Force
Applied Force
Twinned Martensite
Detwinned Martensite

Figure 1.3: The application of stress to twinned martensite produces a residual strain which is recovered when the NiTi transforms to austenite.

The phase transformation of SMAs happens over four transition temperatures, M_f, M_s, A_s, and A_f. During the martensite to austenite (M-A) transition the SMA initially starts out as pure martensite, said to have a martensitic volume fraction, ξ, equal to 1. Once the temperature of the SMA reaches the austenite start temperature, A_s, the volume fraction decreases until the temperature reaches A_f. At this point the SMA is fully austenitic and has $\xi = 0$. Upon cooling, the process is reversed, however the austenite to martensite (A-M) transition takes place over the temperature range between the martensitic start and finish temperatures, M_s and M_f, respectively. A schematic representation of volume fraction at a function of temperature is seen in Figure 1.4.

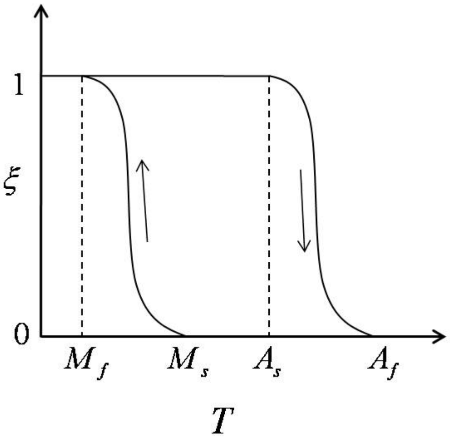

Figure 1.4: Schematic representation of martensitic volume fraction as a function of temperature.

The application of stress on an SMA changes the transformation temperatures, schematically represented in Figure 1.5. As stress increases, the martensitic and austenitic transformation temperatures increase by their respective stress influence coefficients, C_M and C_A, as seen below:

$$M_f^\sigma = M_f + \frac{\sigma}{C_M} \tag{1.1}$$

$$M_s^\sigma = M_s + \frac{\sigma}{C_M} \tag{1.2}$$

$$A_s^\sigma = A_s + \frac{\sigma}{C_A} \tag{1.3}$$

$$A_f^\sigma = A_f + \frac{\sigma}{C_A}. \tag{1.4}$$

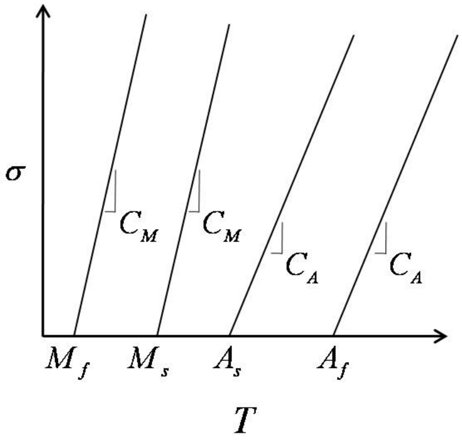

Figure 1.5: Effect of stress on transition temperatures.

The temperature at which the phase transformations occur relative to the operating temperature determines the behavior of an SMA. If the ambient temperature is below M_f the shape memory effect will be observed upon loading and thermal cycling. Stress is first applied to detwin the martensite phase of the SMA. If the stress is released after the martensitic has begun detwinning, only the elastic strain will be recovered and a residual strain will remain, as seen in Figure 1.6. This strain is called the recoverable strain. Upon heating above A_f, the strain due to detwinning is recovered and the wire returns to its original shape.

If the ambient temperature is above A_f the SMA will exhibit superelastic behavior upon loading. The application of stress causes the transformation temperatures to increase. With the application of sufficient stress, the austenitic phase will transform into detwinned martensite as M_s^σ and M_f^σ increase above the ambient temperature. This results in a combination of elastic and transformation, or "pseudoelastic", strain.

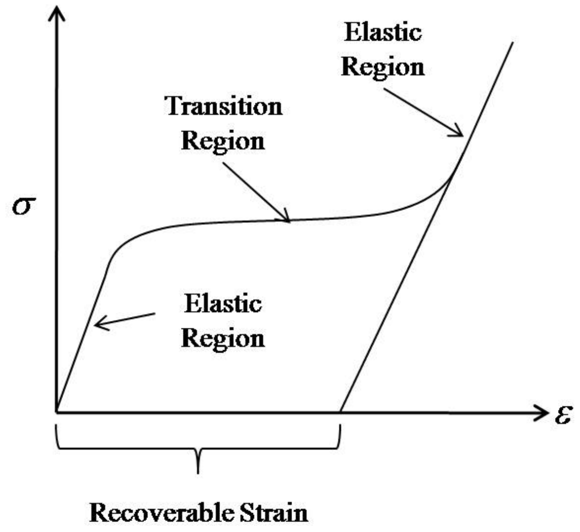

Figure 1.6: Stress-strain curve displaying the shape memory effect and residual strain.

Upon the removal of stress, the SMA will transform back to austenite and retain its original shape as seen in Figure 1.7.

When an SMA is purely austenitic or martensitic, stress-strain behavior can be modeled as a linear elastic material. However, this is not the case in the transition regions or as the martensitic phase is detwinning. There are several models that describe the behavior of the volume fraction between transition temperatures and as the material detwins. The research presented uses the Brinson 1-D constitutive model [2] to determine volume fraction as a function of applied stress and temperature. The modeling of NiTi used in this research will be further discusses in section 3.3.

Utilizing the strain recovery associated with the martensite to austenite phase transformation, NiTi can be used as an actuator. Since there are no moving parts, NiTi has the capability to be used as a reliable actuator replacing large, heavy motors,

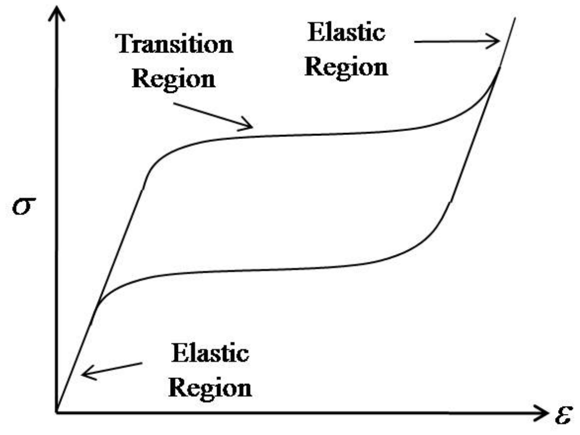

Figure 1.7: Superelastic stress strain curve.

gear trains, and hydraulic systems. In addition to strain recovery, the phase transitions of NiTi create significant changes in some material properties. For instance, there are significant differences in the electrical resistivities and elastic moduli of martensitic and austenitic NiTi. These large property changes make it possible to use NiTi in stress/strain sensing and stiffness tuning applications. By using sensing and actuation properties in tandem, active structures could be constructed using NiTi that could adapt to changes in their environment.

1.3 NiTi Machining and Joining Issues

Machining of NiTi alloys has proven to be very difficult due to the high ductility, work hardening characteristics, and the non-linear stress-strain behavior of the material. These characteristics can cause poor surface finish, irregular chip breakage, and high tool wear [35]. The build-up of heat in traditional machining processes can also locally affect thermo-mechanical properties of the NiTi work piece. Electric Discharge

Machining (EDM) is commonly used to create NiTi parts, however this process is relatively expensive when compared to traditional machining processes. Much of the expense of using NiTi can be eliminated if a reliable and efficient way of joining it to traditional structural materials, such as aluminum or steel alloys, is used; however the concept of joining NiTi to itself and dissimilar materials presents several challenges.

When welding NiTi, there are two general points of concern. The first is the loss of cold work which negatively influences the shape memory or superelastic effects of the alloy due to excessive heating of the material. Oxygen contamination is the second primary concern. Oxygen and other contaminates such as sulfur, nitrogen, or hydrogen can cause embrittlement and decreased strength in NiTi alloys. In addition, the transition temperatures of NiTi alloys are very sensitive to composition and can be affected by impurities. It is possible to regain some of the cold work in a work piece by subjecting it to a post weld heat treatment after the welding process is completed. Oxygen contamination can also be avoided through the use of an inert atmosphere surrounding the joint area during the welding process [34].

The fusion welding of Ti-rich NiTi alloys has a unique concern in the appearance of solidification or hot cracking. Hot cracking occurs due to solidification temperature range of an alloy. An alloy is different from a pure metal in the sense that different alloy compositions will solidify at different temperatures. Thus, rather than a single temperature, complete solidification of an alloy occurs over a temperature range sometimes referred to as the freezing zone [34]. When a NiTi weld pool is cooling, a network of solid alloy forms in the liquid portion of the weld pool. The remaining liquid portion in Ti-rich alloys is usually $TiNi_2$, a brittle alloy. When the solidifying compounds begin to form grain structures, the liquid $TiNi_2$ can infiltrate the

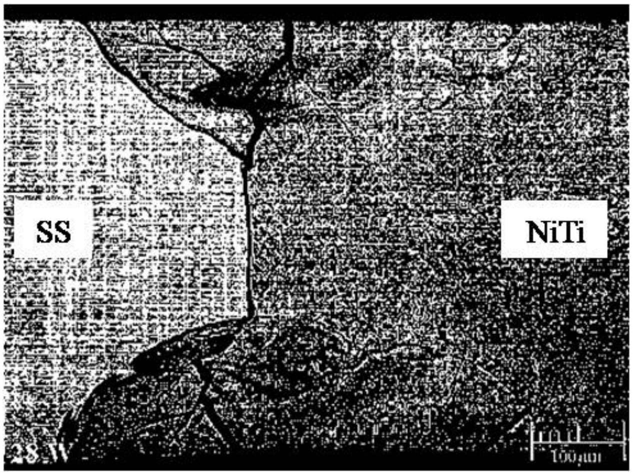

Figure 1.8: Fusion weld of NiTi and SS alloy exhibiting cold cracking in the weld [10].

grain boundaries. As the weld cools, the solid lattice is put under stress as the entire work piece is shrinking in volume. The stress creates cracks at the grain boundaries that then fill with more liquid alloy. As the liquid cools and solidifies the additional shrinking leaves cracks at the grain boundaries. These serve as starter cracks that can propagate through the weld and cause joint failure. In severe cases, the weld may fail completely as it cools after the initial welding process [34].

Cold cracking is a phenomenon that occurs when joining titanium alloys to ferrous alloys. The titanium and iron form brittle intermetallics such as $TiFe$ and $TiFe_2$ [36]. These intermetallics have low strength at room temperature. Fusion welding NiTi to steel readily creates these intermetallics which form along the weld line. As with hot cracking, the contracting volume of the work piece places the intermetallics phases under stress and causes cracks to propagate during cooling, seen in Figure 1.8 [10]. These cracks often result in total weld failure as the joint cools to room temperature.

As described in US patent 6,875,949, a NiTi/steel weld can be successfully made with Ni-rich filler pieces. The addition of Ni dilutes the weld pool and reduces the relative amounts of molten Ti and Fe in the joint; this helps avoid the formation of intermetallic compounds [10]. The use of a Ta or V interlayer has also been suggested to prevent undesired intermetallics from forming by creating a barrier between the Ti and Fe [34]. However the addition of an interlayer increases the complexity of the welding process [10].

Soldering is an attractive method for joining NiTi because soldering uses filler metals that melt at or below 450 °C [30, 32]. With relatively low temperatures, soldering avoids the loss of cold work that must be recovered when using fusion welding processes. However, soldering NiTi is challenging due to the tenacious oxide that forms on Ti and Ti-alloys [8, 38].

1.4 Joining Techniques

1.4.1 Laser Welding

Laser welding is a fusion welding process which utilizes a directed laser beam to heat and melt the base metal of the work pieces. The key benefit to laser welding over traditional fusion welding methods is a narrow Heat Affected Zone (HAZ). The narrow HAZ is due to the focused nature of the laser beam itself, allowing the melting and coalescence of the base metals to take place in a narrow region using localized heating of the base metal.

Laser welding can be accomplished in two modes: a slower, pulsed beam mode, and a fast, constant beam mode. The pulsed beam is generally used for butt welds and gives a resulting weld width of approximately twice the weld depth, as seen in

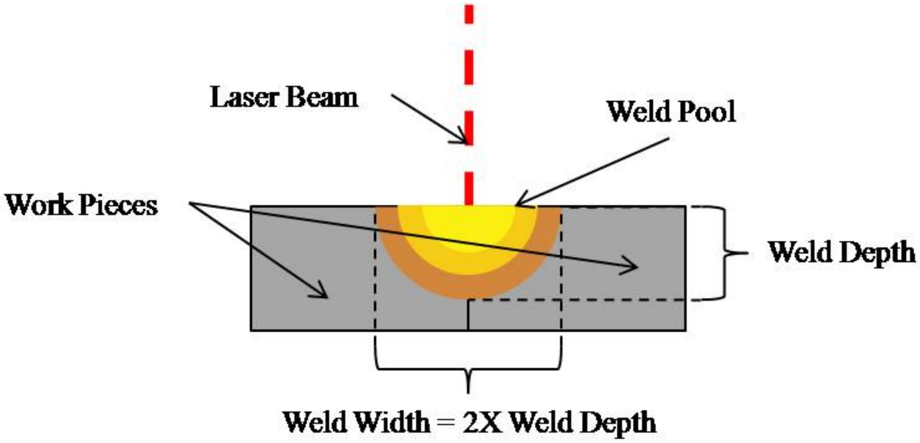

Figure 1.9: Schematic representation of the laser welding process.

Figure 1.9. For deeper penetration, the duty cycle of the laser can be increased up to 100%, a constant beam. When increasing the penetration of the weld, the HAZ becomes larger and the benefit to laser welding dissipates as more base metal is heated through thermal conduction.

Laser welding is currently used to create superelastic NiTi/stainless steel joints for medical instruments [9]. The main limitation to laser welding is available power, resulting in a limitation to weld thickness. Using laser welding, NiTi/NiTi joints up to 0.045” (1.15 mm) thick have been created [6].

1.4.2 Tungsten Inert Gas (TIG) Welding

Tungsten Inert Gas (TIG) welding is a common form of fusion welding used to create joints in a wide variety of metals. TIG is generally used for macro-scale joining operations with work pieces significantly thicker than those possible with laser welding.

In the TIG welding process, an electrical circuit is established between the base material, which is the ground, and the welding unit. The process utilizes an electrical arc from a tungsten electrode to melt the base metals and allow them to coalesce in the weld pool. Generally, TIG is performed with a non-consumable electrode and a constant current DC arc. During welding a shielding gas, such as argon, flows around the electrode and over the weld to protect from oxidation and the formation of weld scale.

TIG is able to join thicker materials because there is more available power relative to laser welding. However, the increased power and relatively large application area, as compared to laser welding, results in a significantly larger HAZ and increased work piece temperatures yielding a greater loss of cold work.

1.4.3 Ultrasonic Soldering (USS)

Ultrasonic Soldering (USS) is a soldering process that utilizes ultrasonic vibrations of soldering iron to create cavitations in the liquid solder resting on the base metal. As the cavitations implode they impinge upon the surface of the base metal breaking up surface oxide layers and cleaning the faying surface, Figure 1.10. The removal of surface oxides increases the wetting of the faying surface by the solder [32]. In many cases, the USS process allows solder to wet otherwise not-wetting materials such as ceramics, glass, titanium, and aluminum [8].

The USS procedure is accomplished on a hot plate that brings the work pieces above the melting temperature of the solder. This assures that the solder is in its liquid phase and able to produce cavitations from the ultrasonic vibrations and avoids the formation of “cold joints”.

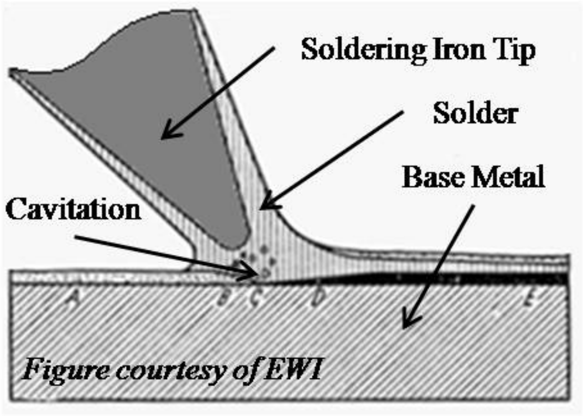

Figure 1.10: Schematic representation of the ultrasonic soldering process.

SonicSolder^{TM}, the solder used in this research, is a Sn-based Pb-free solder that has been developed by Edison Welding Institute (EWI) for use with USS [31]. SonicSolder^{TM} contains an active element, Al, which allows the solder alloy to react with the base metal and improve adhesion [8].

1.5 Ultrasonic Additive Manufacturing (UAM)

Ultrasonic Additive Manufacturing (UAM) is a new manufacturing process that incorporates the principles of ultrasonic metal welding and subtractive processes to create metal parts with arbitrary shapes and seamlessly embedded materials [7]. Ultrasonic metal welding is a solid-state welding process that allows joining of metallic materials far below their respective melting temperatures. This is accomplished by using a sonotrode to apply a normal force at the interface between two metal work pieces. Ultrasonic transducers drive the transversely vibrating tip of the sonotrode which imparts a motion to the top work piece and creates a relative, friction-like action at the interface of the two work pieces. This motion causes shear deformations of contacting surface asperities, dispersing interface oxides and ultimately bringing clean metal-to-metal contact and adhesion between the surfaces [33]. A diagram of the ultrasonic metal welding process is seen in Figure 1.11.

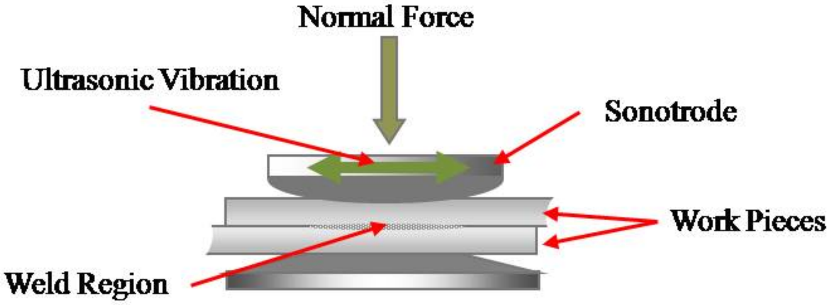

Figure 1.11: Schematic representation of ultrasonic metal welding, a solid-state joining process which forms the basis for UAM.

Ultrasonic metal welding has been adapted into a rotating transducer, booster, and horn system for UAM, creating a new and distinct manufacturing process with capabilities not possible to achieve with the conventional ultrasonic metal welding processes. As shown in Figure 1.12, instead of a spot contact, vibrations generated by a piezoelectric ultrasonic transducer are transmitted into the parts through a rolling sonotrode. The vibrations propagate longitudinally from the transducer to the sonotrode through tuned waveguides. Normal force is applied to the vibrating sonotrode as it rolls along the work piece and the vibrations transmitted to the weld interface cause a solid-state bond between the parts. Current UAM systems achieve the most effective bonding on thin metal layers of approximately 0.006” (152 μm) thickness. The UAM system therefore employs an automated feed mechanism for allowing successive layers of metal tapes, drawn from a continuous spool, to be

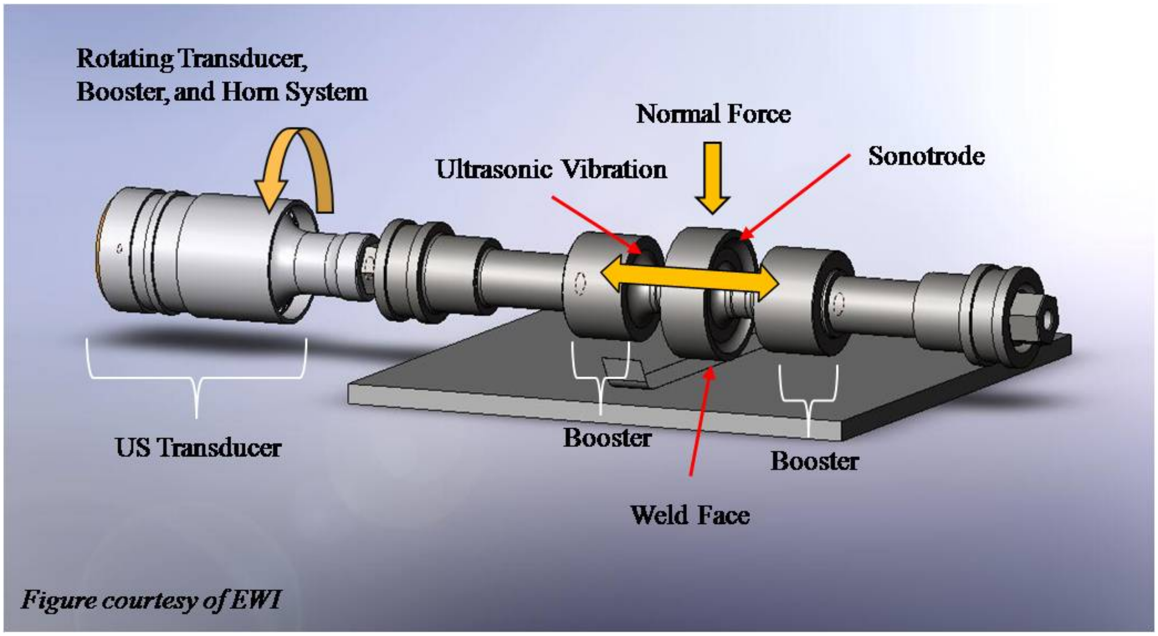
Rotating Transducer,
Booster, and Horn System
Normal Force
Ultrasonic Vibration
Sonotrode
US Transducer
Booster
Booster
Weld Face
Figure courtesy of EWI

Figure 1.12: In the UAM process, successive layers of metal tape are bonding together for creating metallic composites with seamlessly embedded materials and features.

bonded together for creating larger bulk builds. A subtractive CNC machining stage is also fully automatic and integrated within the UAM system as seen in Figure 1.13.

Research has found that the locally generated heat due to ultrasonic vibration during the UAM process is typically between 30-50% of the metling temperature of the base metal [20]. Being a relatively low-temperature process, UAM offers unprecedented opportunities to create parts with embedded smart materials (e.g., shape memory alloys, fiber optics, polymers, etc.) and electronic components. Further, the subtractive stage integrated within the newest UAM systems allows for the simultaneous incorporation of arbitrarily shaped internal features such as cooling channels or designed anisotropies.

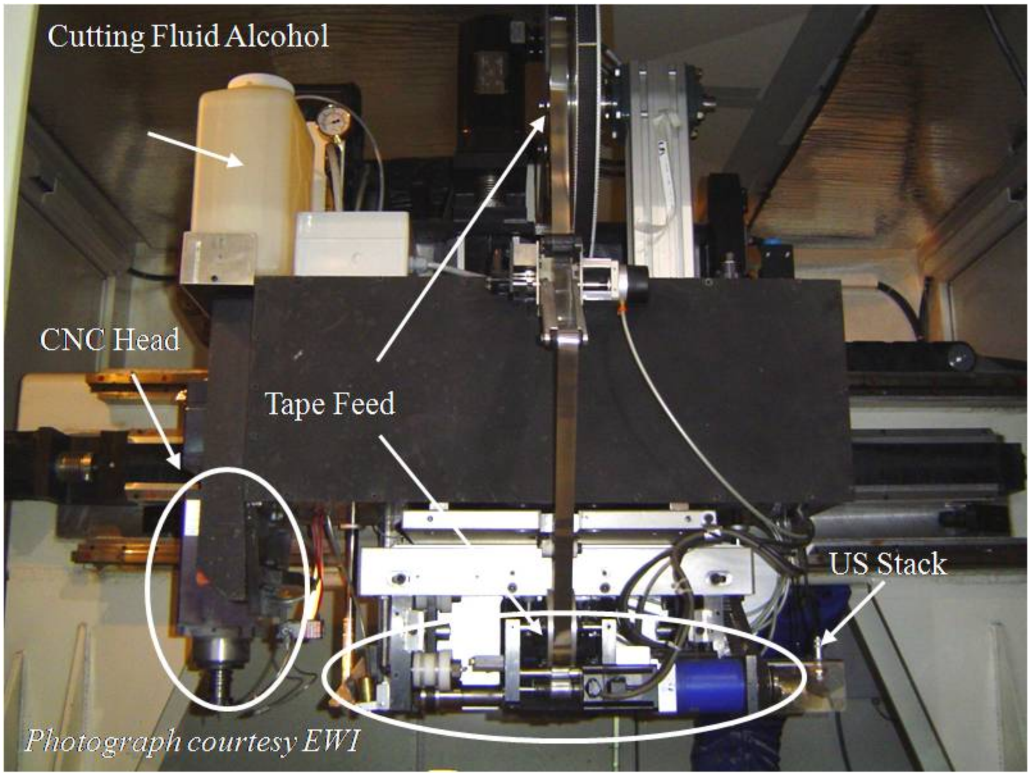
Cutting Fluid Alcohol
CNC Head
Tape Feed
US Stack
Photograph courtesy EWI

Figure 1.13: Ultrasonic transducer, booster, and horn system, tape feed mechanism, and integrated CNC mill.

UAM, also referred to as ultrasonic consolidation, makes it possible to not only embed hard reinforcement materials, such as sigma fibers (TiB fibers with a tungsten core and SiC casing) but also brittle materials such as fiber optics, Figure 1.14(a) and (c). UAM has also been utilized to embed and join dissimilar materials, such as copper and aluminum, Figure 1.14(b), and to create materials with arbitrary internal spaces, Figure 1.14(d). Possibilities of advanced UAM builds include augmented structural panels with embedded reinforcement that could be monitored for damage using embedded sensors, or thermal control using embedded thermocouples for sensing with integrated internal channels for on-demand cooling at specific locations. With UAM it is possible to have a multifunctional build capable of meeting structural, sensing, motion control, and stiffness control requirements. In addition to sensors and fibers, UAM offers the opportunity to embed entire electronic components or circuit boards, allowing for sophisticated data acquisition, control, or monitoring systems to be fully integrated into a structural package.

Embedding materials using UAM can be accomplished through one of two general procedures, depending on the shape and size of the embedded objects. Common to both methods, the UAM process is paused at the desired height of the embedded material. In the first, and most simple, method the embedded material is oriented as desired and the next tape layer is welded as normal. This method relies entirely upon the normal force and ultrasonic vibrations to plastically deform and flow the matrix material around the embedded object and has been used to embed wires up to 0.004" (100 μm) in diameter [17]. As seen in Figure 1.15, this method has proven to work well for round, small diameter NiTi wires, though as the wire diameter increases, more normal force and ultrasonic power are required to produce sufficient material

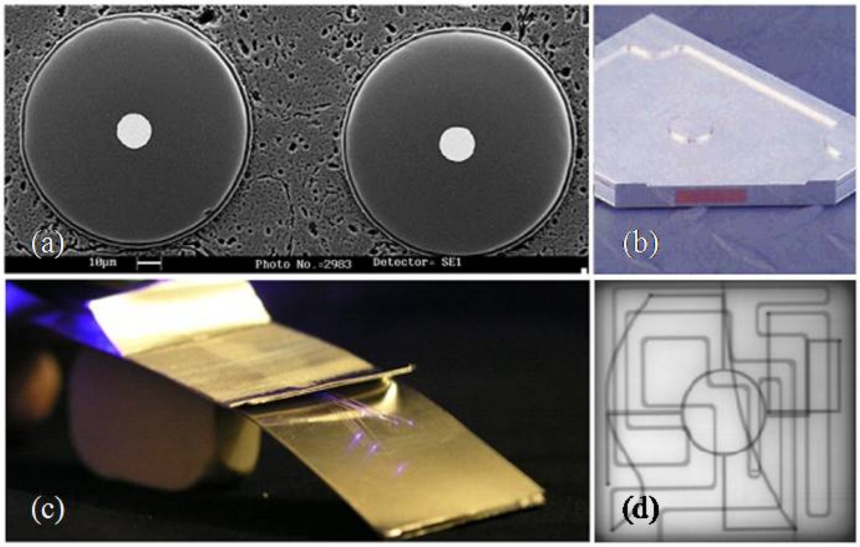

Figure 1.14: (a) Micrograph of 0.004” (100 μm) diameter sigma fibers embedded in aluminum [17]. (b) Aluminum UAM build with embedded copper block. (c) Fiber optics embedded between aluminum tapes. (d) An X-ray image of a UAM build with arbitrary multi-level internal channels made using subtractive processes. (Photographs (b) and (c) courtesy of Solidica, Inc., Image (d) courtesy of EWI)

flow to fully envelop the embedded material. A UAM test bed at EWI, seen in Figure 1.16 has up to 10 kW of available ultrasonic power which allows for the embedding of larger diameter wires.

The second method of embedding involves machining a pocket in the previously consolidated layers. Once the embedded objects are placed in the machined pocket, successive tapes are welded on top to fully enclose the embedded material. This method is used for embedded materials or objects of large size or irregular shape and has been proven as a viable way of embedding sensors and electric components [29].

The strength of UAM bonds have previously been quantified using peel tests [18, 19, 20]. Using peel test data, it has been shown that under ideal weld parameters, including normal force, vibration amplitude, and weld speed, the bond between tapes

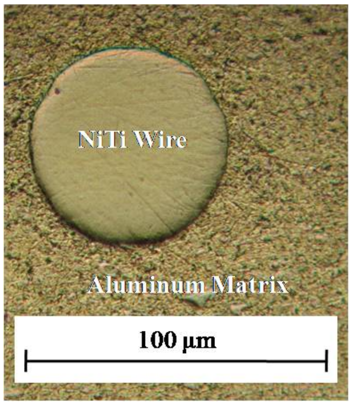

Figure 1.15: Micrograph of 0.003" (75 μm) diameter shape memory NiTi wire fully embedded in Al 3003-H18 UAM matrix utilizing only plastic flow of the matrix material.

joined using UAM can be stronger than the parent material, often causing the work pieces to break before the joint fails [18, 20]. This method works well to compare the bond strength of samples made with different bonding parameters, however it lacks a direct comparison to commonly used material properties such as ultimate tensile strength and ultimate yield strength.

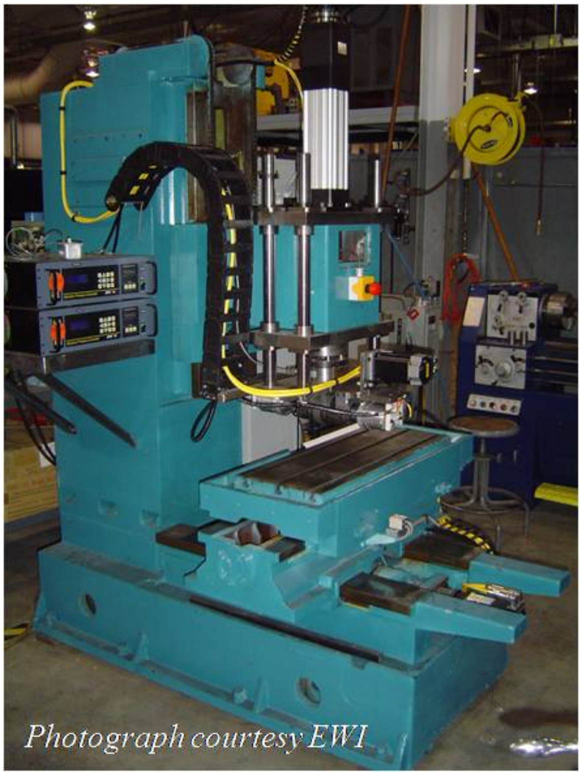
Photograph courtesy EWI

Figure 1.16: The 10 kW UAM test bed system at EWI has increased embedding capabilities.

CHAPTER 2

JOINING OF NITI AND STRUCTURAL MATERIALS

2.1 Joint Characterization Methods

2.1.1 Laser Welding

Previous success with laser welding NiTi to stainless steel [6, 36] made the process a strong starting point to expand the state-of-the-art. To investigate laser welding, tube based butt joints were created with 304 SS tubes and NiTi tubes (55% wt. Ni). As outline in Hall's patent [9], Ni filler was used to dilute the weld pool and reduce the occurrence of intermetallics. 304 SS was chosen because it is one of the most common stainless steel alloys noted for its corrosion resistance, formability, and good weldability [4]. By readily joining NiTi to such a common material it could be easily integrated into many applications.

Laser welding was conducted on a Trumpf PowerWeld 200 W average power pulsed laser system which uses a neodymium-doped yttrium aluminum garnet (Nd:YAG) laser rod. Samples were made by placing the 304 SS tubes, a 0.015" thick Ni washer, and NiTi tube over a tungsten mandrel, as seen in Figure 2.1. The Ni washer was sized to create an approximate 1:1:1 ratio of molten 304 SS, Ni, and NiTi in the weld pool. The mandrel was used to axially and radially align all three pieces. Tack welds

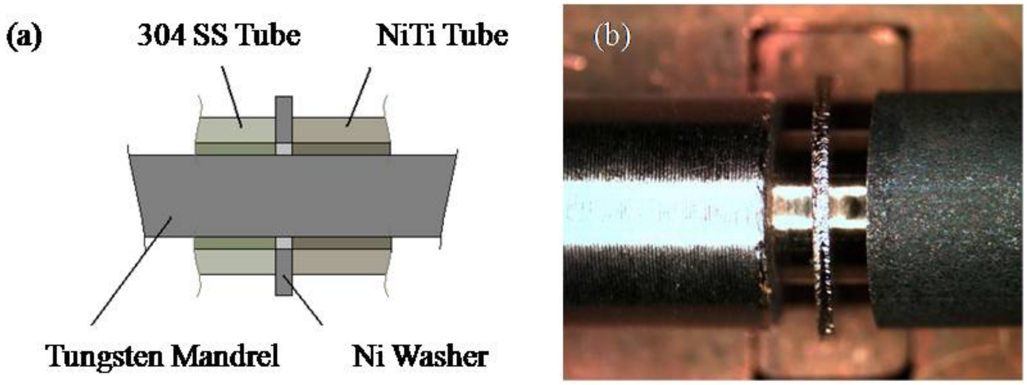

Figure 2.1: (a) Cutaway diagram of assembled 304 SS/NiTi tube sample; (b) Photograph of assembled sample before welding.

were first made to hold all pieces in place during the final series of welds around the joint circumference.

Different welds were created by varying the laser peak power, pulse length, pulse energy, and average power as seen in Table 2.1. Weld parameters for sample 2 were repeated due to geometric misalignment of sample pieces. After welding, specimens were visually examined for cracks. All weld specimens were then mounted, sectioned and polished to observe the weld penetration, estimated HAZ size, and look for possible cracks. Optical micrographs were taken of each section and weld penetration and HAZ extension were measured using a Java based image processing software called ImageJ [26].

2.1.2 Tungsten Inert Gas (TIG) Welding

The experimental plan to join NiTi to structural materials using TIG welding focused on applying the Ni filler concept to create joints with 1/4” thick NiTi (55% wt. Ni) and 304 SS plates. The same grade of stainless steel was chosen as the

Weld	Peak Power [kW]	Pulse Length [ms]	Pulse Energy [J]	Average Power [W]
1	1.7	9.8	16.6	12
2	1.8	12	21.6	15
3	1.8	14	25.2	18
4	1.8	12	21.6	15
5	1.8	12	21.6	15
6	1.8	12	21.6	15

Table 2.1: NiTi/304 SS Laser Weld Parameters.

structural material for TIG welding in order to adapt what was learned from laser welding in an effort to expand the state-of-the-art of fusion welding NiTi.

Plate based fusion welds are commonly evaluated through tensile tests, bending tests, and fatigue tests. For preliminary testing, tensile tests were determined to be the most expedient tests to conduct and obtain an quantification of joint strength. Both bending and fatigue tests are more relevant from a system integration perspective and therefore are not considered for initial evaluation of TIG welds.

To first determine weld parameters, joint geometries, and the ability to incorporate sufficient Ni filler, sample 304 SS/304 SS joints were first made. The weld geometry used for sample construction was a double bevel weld with 45 ° bevels on both sides of one of the 304 SS plates with a flat middle section 0.030” thick, as seen in Figure 2.2. Mating 304 SS plates had a flat mating surface made using conventional machining processes while NiTi plates had a flat surface obtained through EDM. This geometry was chosen because it avoids excessive machining of the NiTi and also reduces the amount of molten iron in the weld pool through removal of 304 SS. The bevel also allows for more Ni filler to be pre-placed in the weld region.

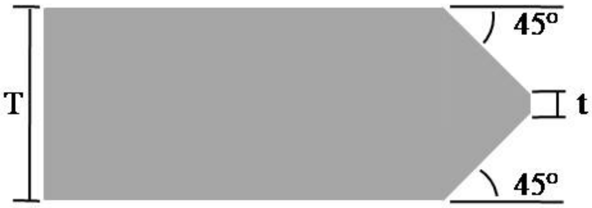

Figure 2.2: Diagram of prepared 304 SS plate for TIG welding to NiTi.

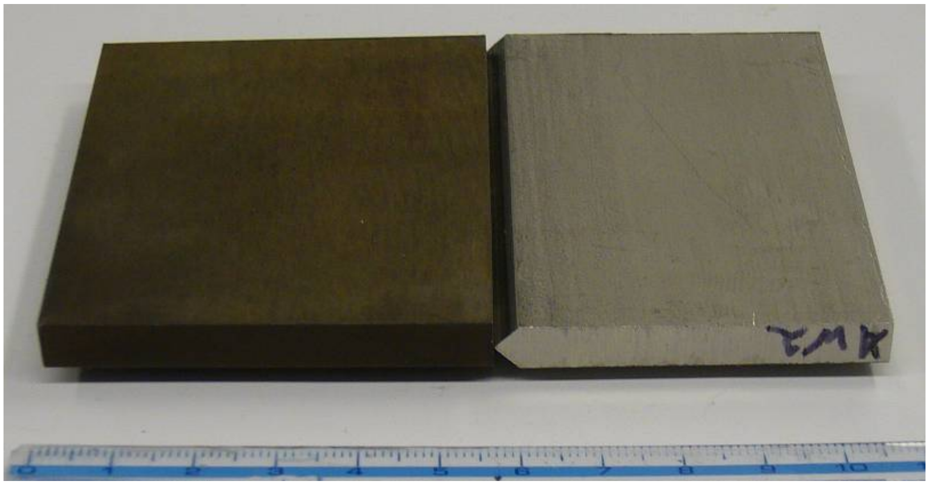

Figure 2.3: Prepared NiTi and 304 SS plates before TIG welding.

The NiTi/304 SS test welds consist of NiTi and 304 SS plates approximately 2” X 3” prepared as described above, seen in Figure 2.3, and welded to form a single plate approximately 4” X 3”. The welded plate was then to be EDM cut in a pattern seen in Figure 2.4 to obtain five dog bone specimens. The NiTi/304 SS dog bones were then to be evaluated through tensile testing.

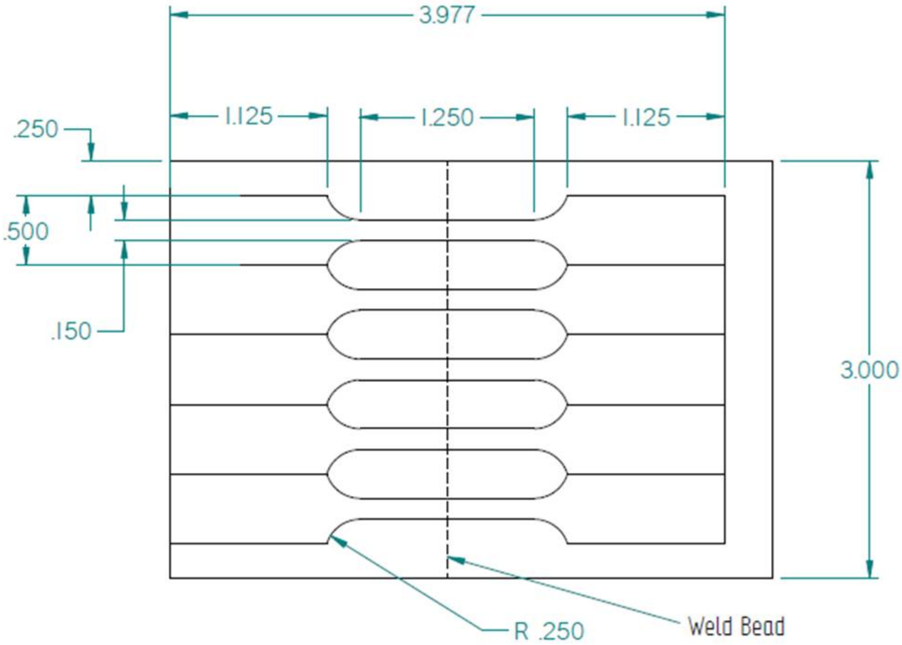
3.977
1.125
1.250
1.125
.250
.500
.150
3.000
R .250
Weld Bead

Figure 2.4: EDM pattern for cutting tensile samples from 304 SS/NiTi TIG weld, all dimensions in inches.

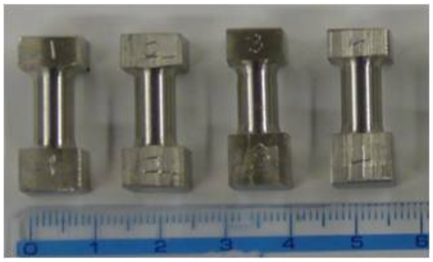

Figure 2.5: Bulk SonicSolder^{TM} tensile specimens.

2.1.3 Ultrasonic Soldering (USS)

2.1.3.1 Bulk Solder Tensile Testing

2.1.3.1.1 Sample Construction The filler metal used in all USS joints, SonicSolder^{TM}, was machined into samples to test its tensile strength. SonicSolder^{TM} tensile test specimens were created with a gauge length of 0.450" and a nominal gauge diameter of 0.250", as seen in Figure 2.5. The tensile samples were machined from a solid cast ingot of SonicSolder^{TM}.

2.1.3.1.2 Sample Testing Tensile strength tests were performed on the solid solder samples. Grips were specially made to place the samples under tensile stress. The tensile grip design can be seen in appendix A. Samples were axially loaded under displacement control. Grip displacement was controlled by a ramp with an average rate of 0.02 in/s. During testing, displacement was measured by the Linear Variable Differential Transformer (LVDT) integrated in the load frame and applied force was measured using a load cell placed in series with the load train.

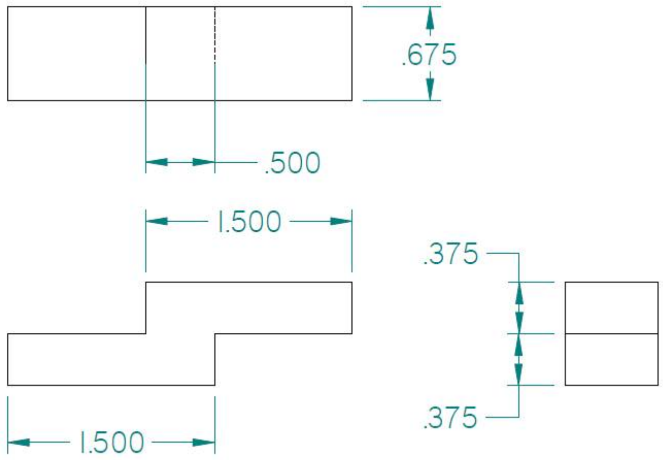

Figure 2.6: Dimensions for SonicSolder^{TM} shear specimen, all dimensions in inches.

2.1.3.2 Bulk Solder Shear Testing

2.1.3.2.1 Sample Construction SonicSolder^{TM} was also used to create a shear specimen as seen in Figure 2.6 with a shear plane measuring 0.675” X 0.500”. The shear specimen was machined from a solid cast ingot of SonicSolder^{TM}.

2.1.3.2.2 Sample Testing Testing of the SonicSolder^{TM} shear specimen utilized a shear testing jig which supported one half of the specimen while applying a direct shear load to the other half as seen in Figure 2.7. This loading scheme causes all resulting shear stress to be transmitted through the shear plane. The design of the shear jig can be seen in appendix A. The test specimen was loaded in compression under displacement control until failure. Ram displacement was controlled by a ramp with an average rate of 0.007 in/s. During testing, displacement was measured by the load frame’s integrated LVDT and applied force was measured using a load cell placed in series with the load train.

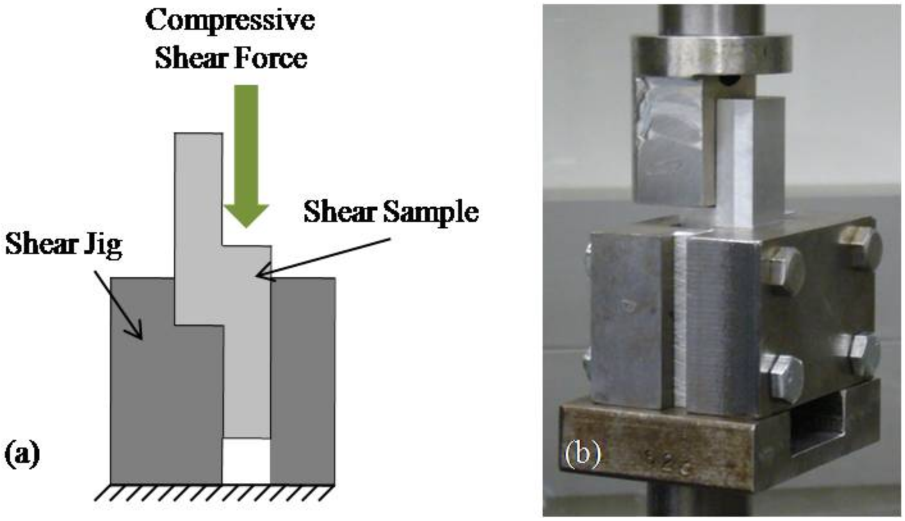

Figure 2.7: (a)Diagram of compressive shear testing jig; (b) Shear test photograph.

2.1.3.3 USS Lap Shear Testing

2.1.3.3.1 Sample Construction A lap shear joint is the typical geometry used for load bearing solder, braze, and adhesive joints [1, 30, 32]. In this geometry, the joint area can be easily increased to augment joint strength. Also, unlike a solder joint in tension, the strength of a soldered lap shear joint is not strongly dependent on the thickness of the solder layer [39]. Since soldering does not involve the melting of base metals, the joining study was expanded to include Al 2024 and O1 tool steel in addition to 304 SS. Al 2024 was chosen because it is a common aerospace alloys noted for its fatigue strength and moderately high yield strength [11]. O1 tool steel is a common oil hardenable steel that is frequently used for tools, dies, and fixtures [14].

In order to test the USS joint shear strength when joined to typical structural materials, joints between two pieces of Al 2024, O1 tool steel, and 304 SS were created and tested. These baseline tests were performed in two groups, one with no surface treatment of the faying surfaces and the second using a 50 μm SiC grit blast of all faying surfaces followed by a methanol rinse to remove any SiC particles and other surface contaminants.

Soldering the lap shear samples was accomplished with a high power USS system at EWI. During soldering, base metal pieces were placed on a hot plate and preheated to 250 °C, approximately 20 °C above the melting point of SonicSolder^{TM} [31], to ensure that the solder was fully melted and allow for cavitation. The faying surfaces were next tinned with SonicSolder^{TM} using the USS iron. Once tinned, the base metals were placed on the soldering jig, which was designed to maintain a nominal solder thickness of 0.003". Drawings of the lap shear soldering jig can be seen in appendix A. Additional solder was placed at the joint interface to allow capillary action to fill any voids and ensure a consistent, void-free, solder joint. The jig and sample were then taken from the hot plate and allowed to cool.

USS lap shear specimens were similar in dimension to the SonicSolder^{TM} bulk shear specimen, discussed in section 2.1.3.2.1, except the overall thickness of the final sample which was greater than the nominal 0.750" to allow for the thickness of the solder joint. Figure 2.8 shows a typical shear test specimen with nominal thickness dimensions. After soldering, samples were machined to realign any surfaces that were not square due to misalignments during the soldering process as well as remove solder flash.

The Al 2024, O1 tool steel, and 304 SS shear samples can be seen in Figures 2.9, 2.10, and 2.11, respectively. The samples pictured have gone through the post soldering flash removal and squaring processes. During the final machining process, two samples, O1/O1 tool steel sample 1 and 304 SS/304 SS sample 4, broke. Both

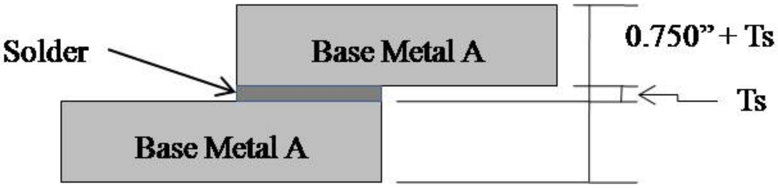

Figure 2.8: Diagram of USS lap shear specimen.

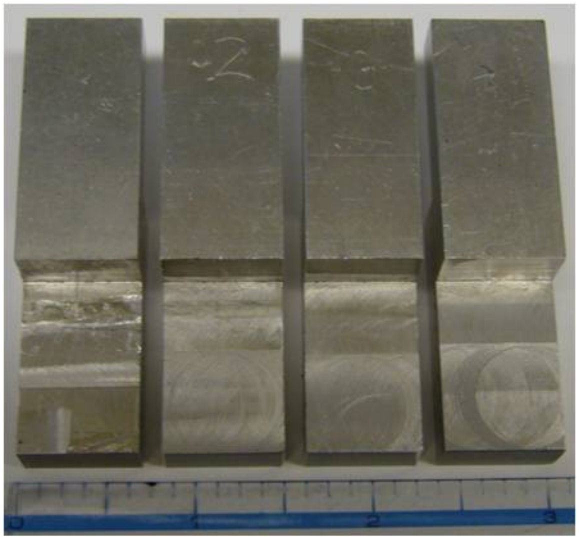

Figure 2.9: Al 2024/Al 2024 USS lap shear specimen.

samples were from the set of joints that had no surface preparation prior to soldering.

Once baseline USS shear strength results were obtained for structural materials, a third set of lap shear joints was made to measure the shear strength of NiTi containing USS joints. NiTi pieces (55% wt. Ni) were jointed to NiTi, Al 2024, O1 tool steel, and 304 SS pieces. Dimensions of the NiTi lap shear joints are slightly different than the previous lap shear joints. The NiTi pieces used were 0.250" thick, however shims

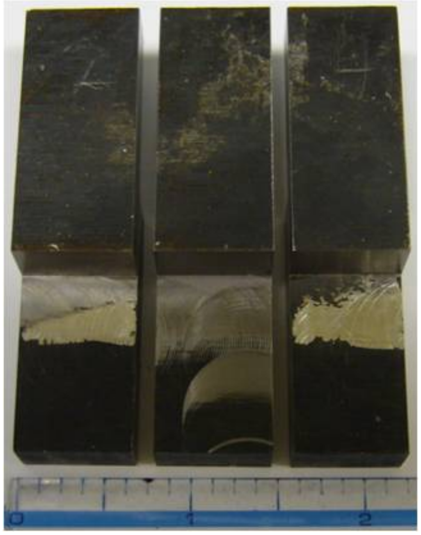

Figure 2.10: O1 tool steel/O1 tool steel USS lap shear specimen.

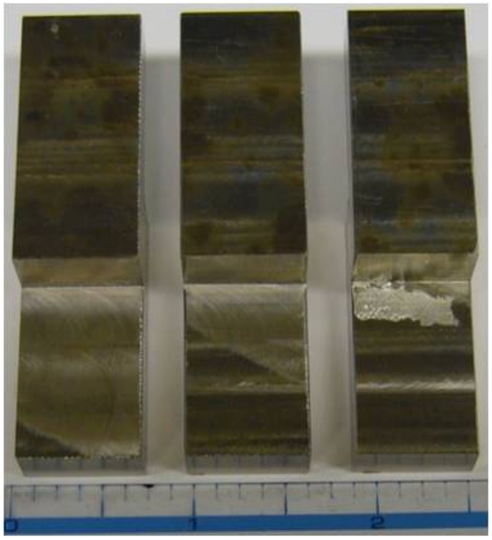

Figure 2.11: 304 SS/304 SS USS lap shear specimen.

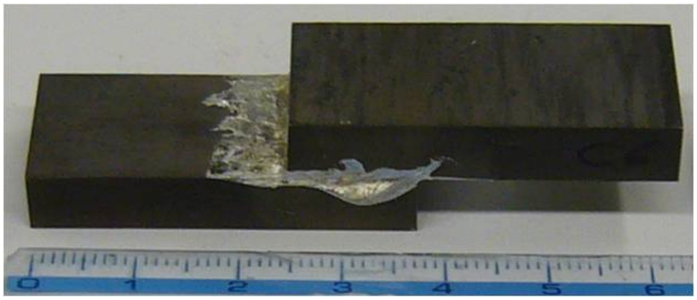

Figure 2.12: NiTi/NiTi USS lap shear specimen.

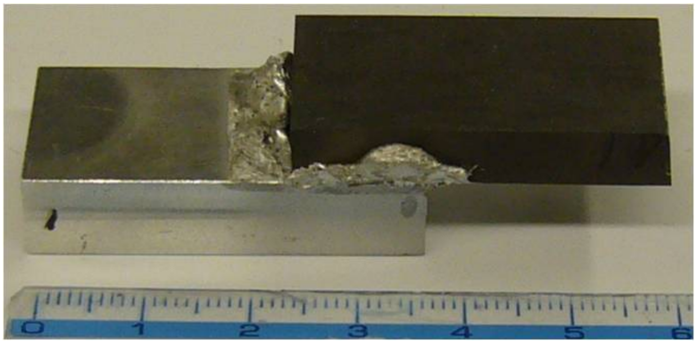

Figure 2.13: NiTi/Al 2024 USS lap shear specimen.

were used in construction to ensure proper solder joint thickness was maintained. In creating NiTi containing joints, all samples were first surface treated with a 50 μm SiC grit blast and rinsed with methanol prior to being soldered. The joining process for NiTi containing lap shear joints was identical to the process for the previous USS joint sets. Figures 2.12, 2.13, 2.14, and 2.15 show NiTi/NiTi, NiTi/Al 2024, NiTi/O1, and NiTi/304 SS solder joints, respectively. These pictures show the joints before solder flash removal.

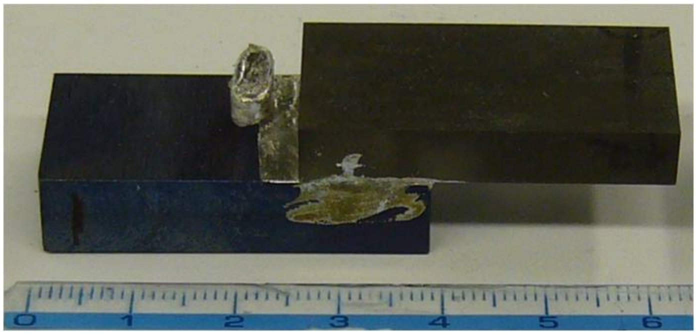

Figure 2.14: NiTi/O1 tool steel USS lap shear specimen.

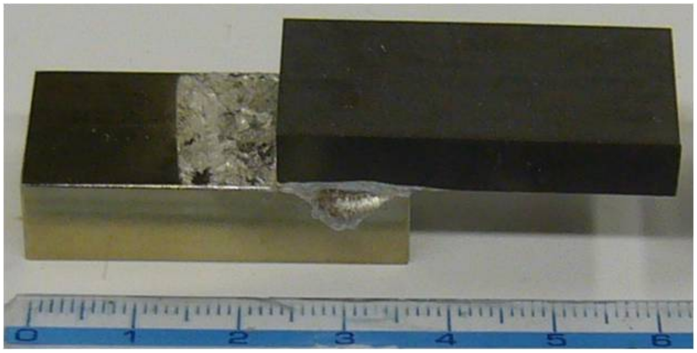

Figure 2.15: NiTi/304 SS USS lap shear specimen.

2.1.3.3.2 Sample Testing Testing the lap shear joints utilizes the same shear testing jig as described in testing the SonicSolder^{TM} shear strength in section 2.1.3.2.2 and appendix A. Test specimens were loaded in compression under displacement control until failure. Displacement was controlled by a ramp of 0.01 in/s. During testing, displacement was measured by the LVDT integrated in the load frame and applied force was measured using a load cell placed in series with the load train.

2.1.3.4 USS Torsional Shear Testing

2.1.3.4.1 Sample Construction Torsional USS test samples were created based upon the results from lap shear tests. The torsion samples consist of a NiTi tube (55% wt. Ni) with a 0.200" nominal outer diameter and 0.135" nominal inner diameter and two sets of Al 2024 saddles, as seen in Figure 2.16. The saddles were designed to maintain a nominal solder thickness of 0.003". Drawings of the saddles and completed samles can be seen in appendix A. The saddles and tube faying surfaces were subject to a 50 μm SiC grit blast and methanol rinse before being soldered. Due to the geometric nature of the saddles, a commercial USS unit was used to solder the torsion specimens. The commercial unit, Sunbonder USM-IV, was used because the iron has a smaller tip that could be used to solder the concave surface of the saddles.

Saddle pieces and the NiTi tube were all placed on a hot plate and preheated to 250 °C. The faying surfaces of the saddle pieces were next tinned with SonicSolder^{TM} using the USS iron. Half of the NiTi tube was tinned as well and placed in two saddle halves. Next, the remaining half of the NiTi tube was tinned and the mating saddle halves were set in place.

Once all pieces were assembled, the torsion specimen was placed in a pre-heated cooling jig, as seen in Figure 2.17. The cooling jig aligned both sets of saddles and

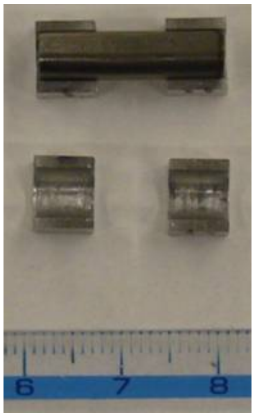

Figure 2.16: NiTi tube and Al 2024 saddles used to create NiTi/Al 2024 torsion sample.

allowed them to be spaced the proper distance apart. Drawings of the cooling jig and torsional sample pieces can be seen in appendix A. Before cooling, additional solder was placed at all exposed joint interfaces to allow capillary action to fill any voids and ensure consistent, void-free, joints. The jig and sample were then taken from the hot plate and allowed to cool. After the sample cooled, excess solder flash was removed.

Two different samples were created. The first, seen in Figure 2.18 (a), had two identical saddle sets 0.250" long on either side of a 0.250" unbonded tube length. After testing the first sample, a second sample, seen in Figure 2.18 (b), was made using one 0.250" long saddle set and one 0.375" long saddle set leaving a 0.125" length of tube unbonded. The difference in saddle length was made to ensure joint failure at the 0.250" long saddle joint.

2.1.3.4.2 Sample Testing Torsion samples were tested in a 2-axis hydraulic load frame. Specialized grip adapters were used to transmit torque applied by the frame

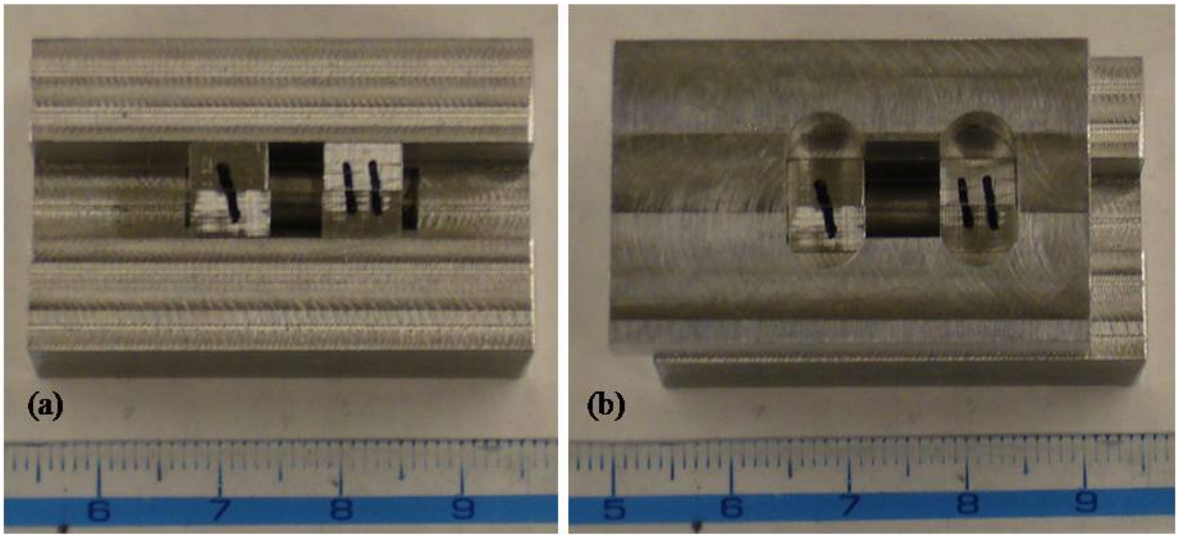

Figure 2.17: USS NiTi/Al 2024 torsion sample cooling jig (a) saddle alignment portion and (b) saddle spacing gauge.

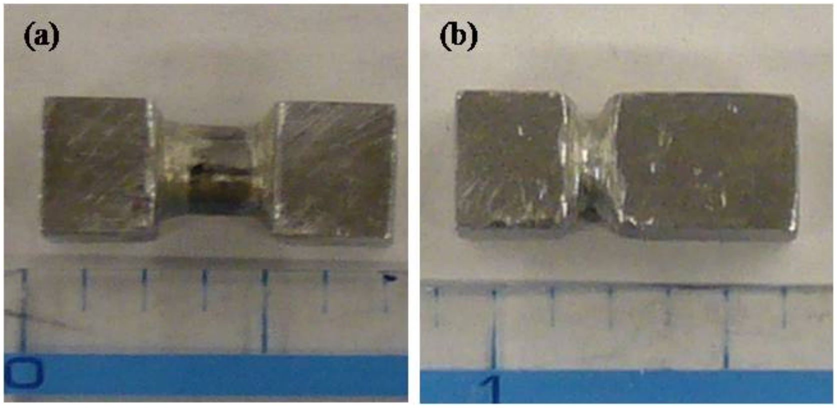

Figure 2.18: (a) First NiTi/Al 2024 USS torsion sample with symmetric saddles; (b) Second NiTi/Al 2024 USS torsion samples with extended saddles.

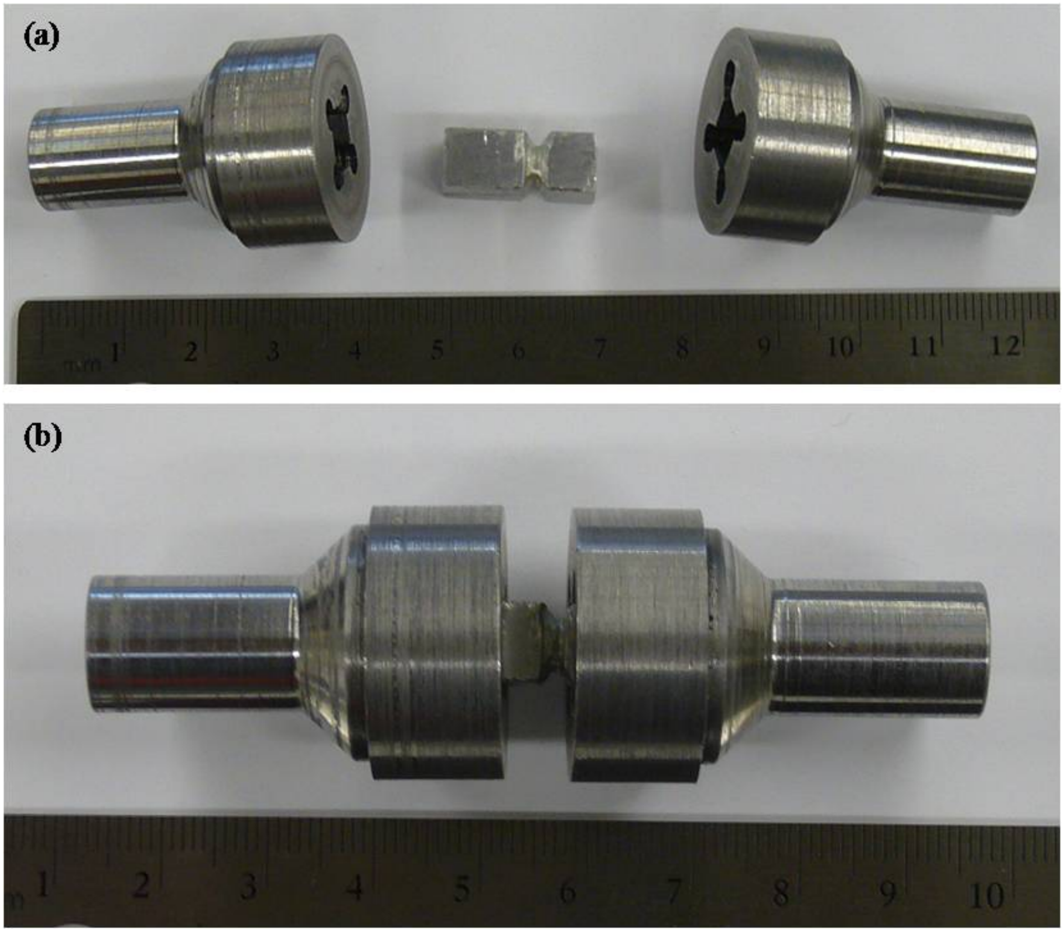

Figure 2.19: Torsion testing adapters for USS NiTi/Al 2024 torsion specimens.

to the solder joint, as seen in Figure 2.19. The design of the torsion sample grip adapters can be seen in appendix A.

During testing, the samples were given a compressive preload. The 15 lbs compressive preload was used to ensure the sample remained in the torsional grips. Samples were subjected to a torsion generated by an angular displacement ramp while measuring angle of twist, axial force, and torsion. The first sample was tested by applying a 35 ° angular displacement ramp over a 2 minute period. The second test of the first sample and the second sample test had the angular displacement increased to 60 ° over a 2 minute period. Angle of twist measurements were taken from the integrated angular displacement sensor while axial and torsional forces were measured from a load cell in series with the load train.

2.1.3.5 USS Sample Sectioning

Two NiTi/Al 2024 USS joint were constructed for the purpose of mounting, sectioning, and polishing to observe interaction between the NiTi and Al 2024 with the SonicSolder^{TM}. Al 2024 samples were machined with a 0.003" recess to control solder thickness. Faying surfaces of the NiTi and Al 2024 pieces were treated with a 50 μm SiC grit blast and methanol rinse prior to joining. One of the resulting joints was hot mounted in a polymer matrix while the second was cold mounted in an epoxy matrix.

2.2 Joint Characterization Results

2.2.1 Laser Welding

Half of the NiTi/304 SS laser weld, welds 1, 2, and 5, showed no cracks through initial visual inspection. Typical weld penetration ranged from 0.012" to 0.022" with the maximum penetration in sample 2, shown in Figure 2.20. However, through micrographic analysis of its section, it was found that weld 2 also had a crack on the NiTi side of the weld bead. The average HAZ extensions from the weld pool were found to be between 2.76×10^{-4} in and 5.24×10^{-4} in. A summary of results for the welds can be seen in Table 2.2. All laser weld micrographs can be seen in appendix B.

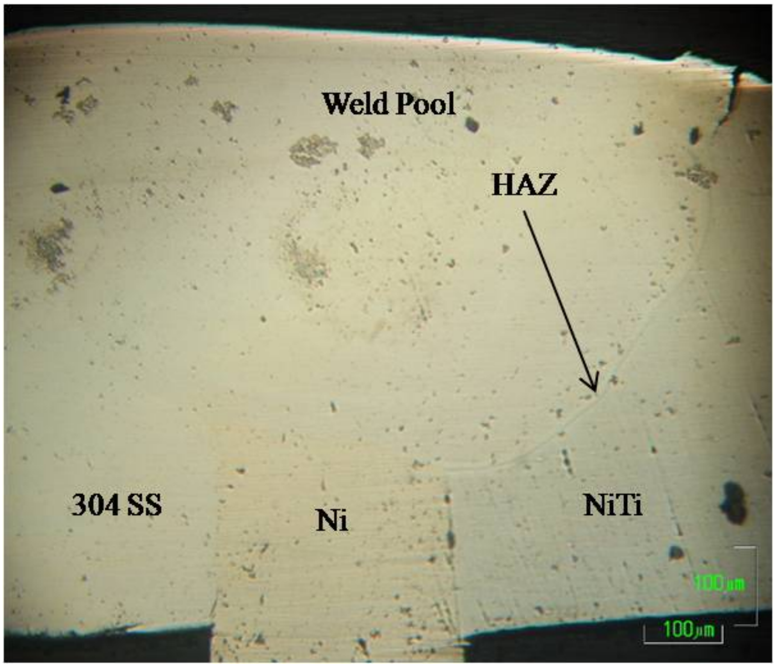
Weld Pool
HAZ
304 SS
Ni
NiTi
100µm
100µm

Figure 2.20: NiTi/304 SS laser weld 2.

Weld	Maximum Penetration [in]	Average HAZ Extension [in]	Cracks Noted
1	0.017	2.76×10^{-4}	No
2	0.022	3.02×10^{-4}	Yes
3	0.019	5.14×10^{-4}	Yes
4	0.012	3.83×10^{-4}	Yes
5	0.020	5.24×10^{-4}	No
6	0.017	4.23×10^{-4}	Yes

Table 2.2: Laser weld penetration and cracking.

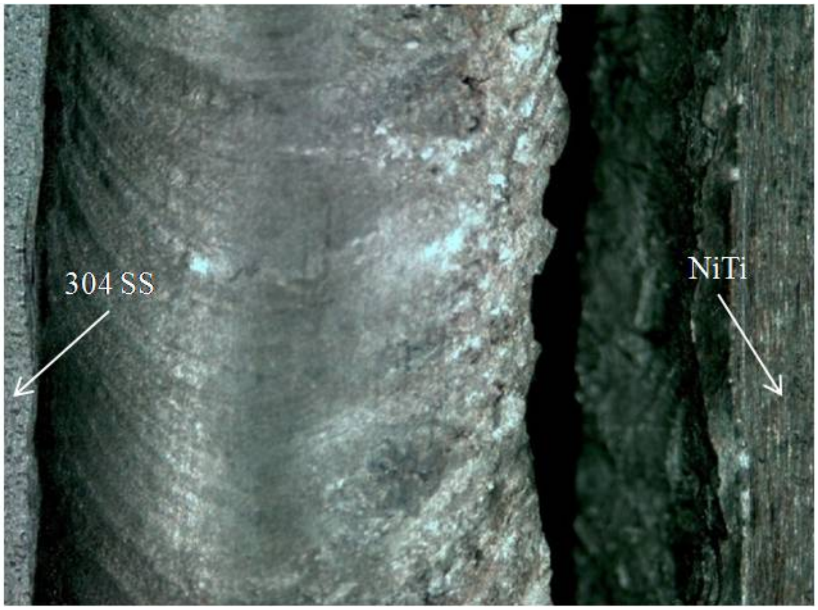

Figure 2.21: NiTi/304 SS TIG weld 1.

2.2.2 Tungsten Inert Gas (TIG) Welding

Two attempts were made to create NiTi/304 SS plate butt welds. Both test joints failed, developing cracks during cooling that ran the length of the weld. The first weld was attempted with an approximate 1:1:1 ratio of molten 304 SS, Ni filler, and NiTi in the weld pool, as done with NiTi/304 SS laser weld. Weld 1 cracked along the weld bead on the NiTi side of the weld as seen in Figure 2.21. The crack developed along the entire length during cooling and resulted in a near zero weld strength.

The second attempt added more Ni filler and also moved the position of the welding arc closer to the NiTi side to allow for more molten NiTi and less molten Fe in the weld pool. This weld also began cracking as it cooled. As seen in Figure 2.22, TIG weld 2 had a transverse crack that first started at the middle of the joint beginning at the NiTi side. After further development of the transverse crack, a

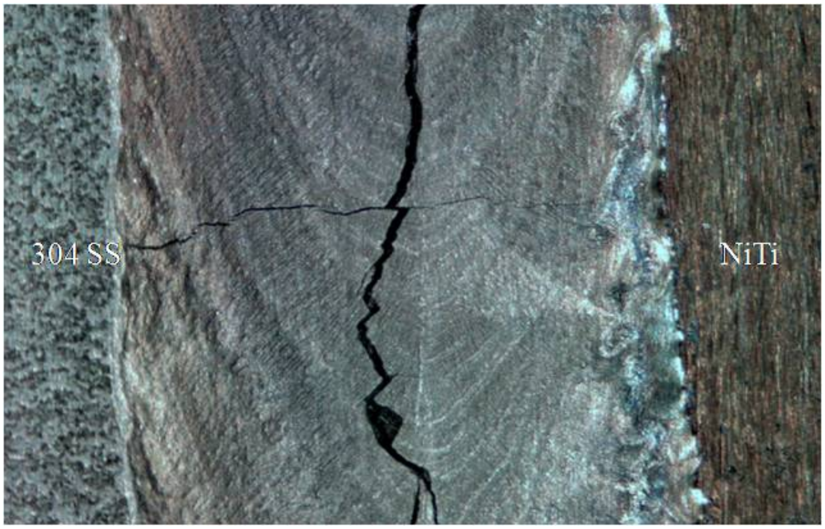

Figure 2.22: NiTi/304 SS TIG weld 2.

longitudinal crack down the length of the weld occurred at the center of the weld bead. Both the transverse and longitudinal crack run across the entire weld bead in their respective directions.

2.2.3 Ultrasonic Soldering (USS)

2.2.3.1 Bulk Solder Tensile Testing

The ultimate tensile strength of the bulk SonicSolder^{TM} tests can be seen in Table 2.3. A typical force versus displacement plot can be seen in Figure 2.23. As seen in the table, all tests were consistent and gave an average ultimate tensile strength of 7.80 ksi with a coefficient of variance, C_v, of 2.05%. All force versus displacement plots can be seen in appendix C. While several samples did not rupture, clear maximum values are observed in all solder tensile tests.

Sample	Ultimate Tensile Strength [ksi]
1	8.06
2	7.85
3	8.00
4	7.78
5	7.66
6	7.70
7	7.74
8	7.61
Average	7.80
Standard Deviation	0.16
C_v	2.05%

Table 2.3: SonicSolder^{TM} tensile test results.

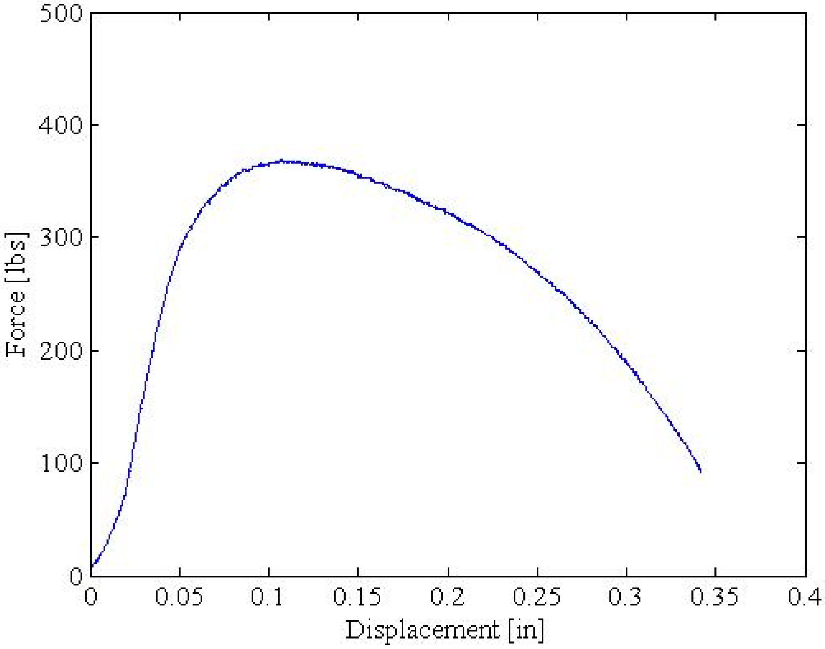

Figure 2.23: Bulk SonicSolder^{TM} tensile sample 6 force versus displacement test.

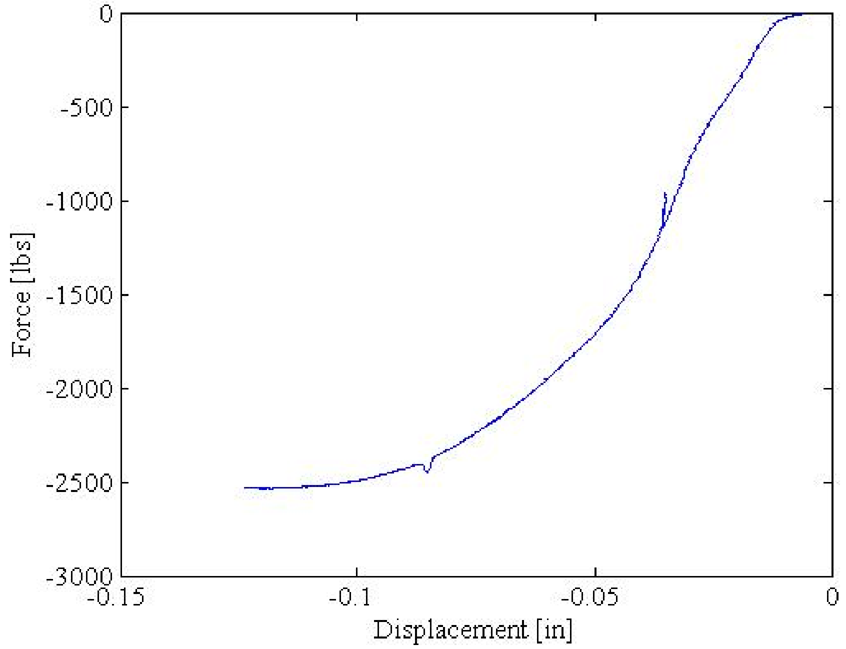

Figure 2.24: Bulk SonicSolder^{TM} shear sample force versus displacement test.

2.2.3.2 Bulk Solder Shear Testing

The force versus displacement plot of bulk Sonic Solder is seen in Figure 2.24. The results of the test indicate the shear yield strength of bulk Sonic Solder is 7.40 ksi. The shear sample did not rupture but did undergo substantial plastic deformation.

2.2.3.3 USS Lap Shear Testing

The results for the USS lap shear tests for Al 2024/Al 2024 pairs, O1/O1 tool steel pairs, and 304 SS/304 SS pairs are seen in Tables 2.4, 2.5, and 2.6, respectively. All force versus displacement plots for each USS material pair can be seen in appendix C.

Al 2024/Al 2024	Ultimate Shear Stress [ksi]	
Sample	No Surface Prep	Surface Prep
1	-	10.7
2	10.1	11.0
3	9.37	11.0
4	1.97	11.3
Average	9.74	11.0
Standard Deviation	0.52	0.24
C_v	5.30%	2.23%

Table 2.4: Al 2024/Al 2024 lap shear test results.

O1/O1 tool steel	Ultimate Shear Stress [ksi]	
Sample	No Surface Prep	Surface Prep
1	-	5.24
2	3.05	4.95
3	0.54	5.48
4	2.05	
Average	1.88	5.22
Standard Deviation	1.26	0.26
C_v	67.2%	5.08%

Table 2.5: O1/O1 tool steel lap shear test results.

304 SS/304 SS	Ultimate Shear Stress [ksi]	
Sample	No Surface Prep	Surface Prep
1	1.11	6.05
2	0.34	4.63
3	0.26	2.91
4	-	
Average	0.57	4.53
Standard Deviation	0.47	1.57
C_v	82.2%	34.6%

Table 2.6: 304 SS/304 SS lap shear test results.

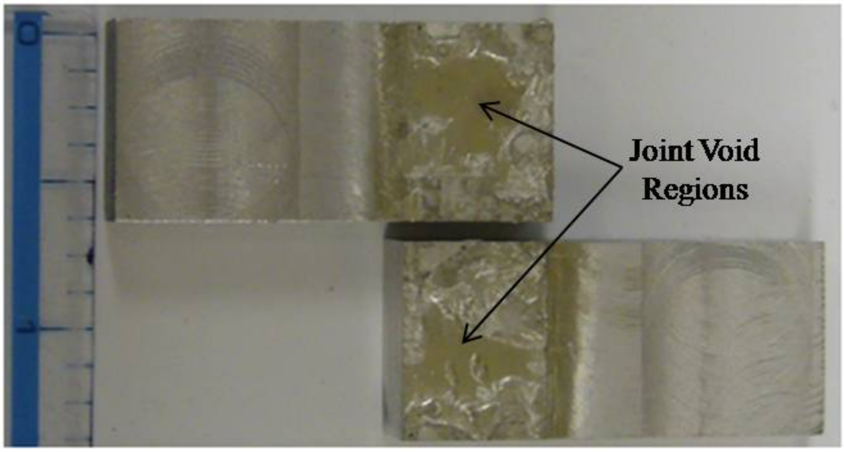

Figure 2.25: Al2024/Al 2024 USS shear sample 4 showing void areas.

Without surface treatment, Al 2024/Al 2024 lap shear joints have an average ultimate shear strength of 9.74 ksi with a C_v of 5.30%. With surface treatment, the average ultimate shear strength is 11.0 ksi with a C_v of 2.23%. Force data for Al 2024/Al 2024 joint 1 with no surface treatment was lost due to an error in testing. Al 2024/Al 2024 joint 4 with no surface preparation was discarded as an outlier because the fracture surface, seen in Figure 2.25, shows a large void was present in the solder joint. This void was due to an error in manufacturing the sample and is therefore not representative of the strength of an Al 2024 USS joint.

The O1/O1 tool steel lap shear joints have an average ultimate shear strength of 1.88 ksi and C_v of 67.2% without surface treatment. With the application of surface treatment, the average ultimate shear strength is 5.22 ksi with a C_v of 5.08%.

Similarly, 304 SS USS lap shear joints have an average ultimate shear strength of 570 psi with a C_v of 82.2% when soldered with no surface treatment. With surface treatment the average ultimate shear strength is 4.35 ksi with a C_v of 34.6%.

NiTi	Ultimate Shear Stress [ksi]			
Sample	NiTi	Al 2024	O1 tool steel	304 SS
1	4.43	7.52	5.86	6.80
2	4.12	8.37	4.31	5.27
3	4.92	7.51	6.00	5.59
Average	4.49	7.80	5.39	5.89
Standard Deviation	0.40	0.49	0.94	0.81
C_v	8.98%	6.33%	17.4%	13.7%

Table 2.7: NiTi lap shear test results.

Table 2.7 shows the ultimate shear stress for all NiTi containing USS lap shear joints. As seen from the results, the average USS is 4.49 ksi for NiTi/NiTi joints with a C_v of 8.89%, 7800 psi for NiTi/Al 2024 joints with a C_v of 6.33%, 5390 psi for NiTi/O1 tool steel with a C_v of 17.4%, and 5890 psi for NiTi/304 SS joints with a C_v of 13.7%.

2.2.3.4 USS Torsional Shear Testing

The angular displacement versus torque plot for the first NiTi/Al 2024 torsion sample can be seen in Figure 2.26. The peak torque was found to be 67.3 in-lbs. The torsion sample did not break on the first test and when removed from the load frame had significant residual angular displacement, as seen in Figure 2.27. A second torsional test resulted in a failure of the solder joint after a peak torque of 32.5 in-lbs. The angular displacement versus torque plot for the second test can be seen in Figure 2.28.

The angular displacement versus torque plot for the second NiTi/Al 2024 torsion sample can be seen in Figure 2.29. The peak torque for this test was found to be 49.6 in-lbs resulting in failure of the solder joint at the short saddle set.

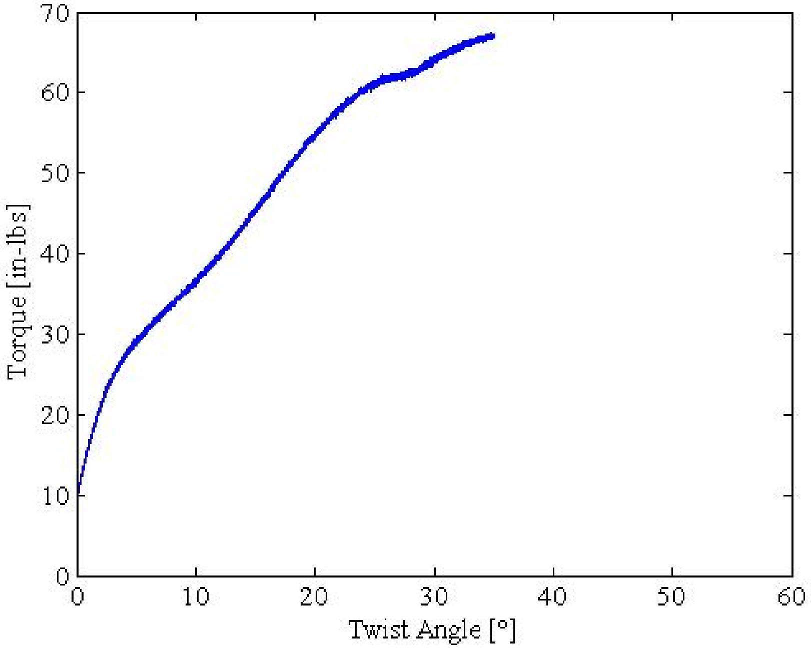

Figure 2.26: USS torsion sample 1 torque versus angular displacement test 1.

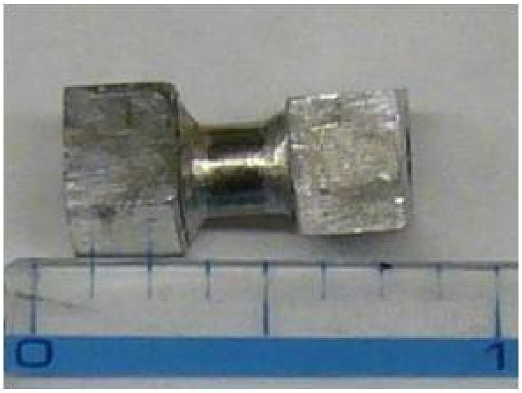

Figure 2.27: Deformed NiTi/Al 2024 torsion specimen after testing.

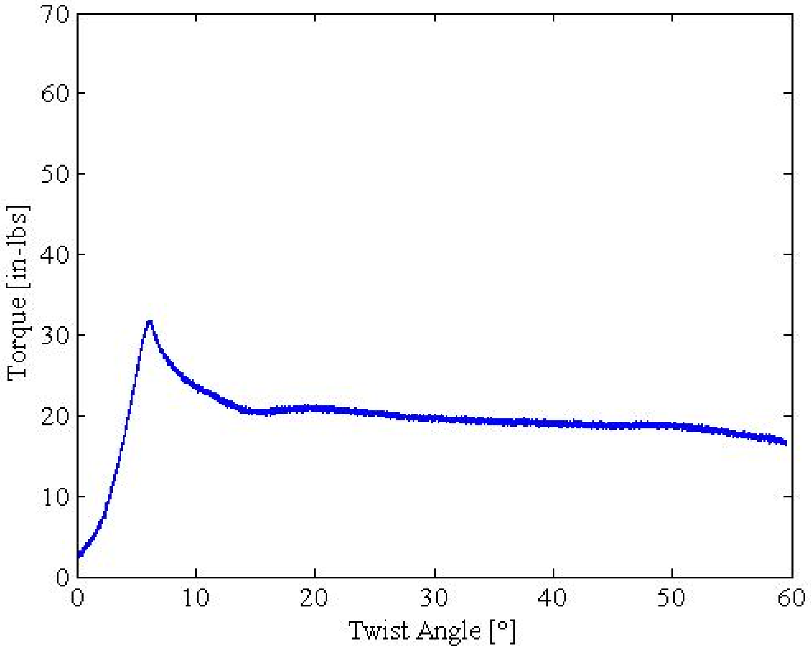

Figure 2.28: USS torsion sample 1 torque versus angular displacement test 2.

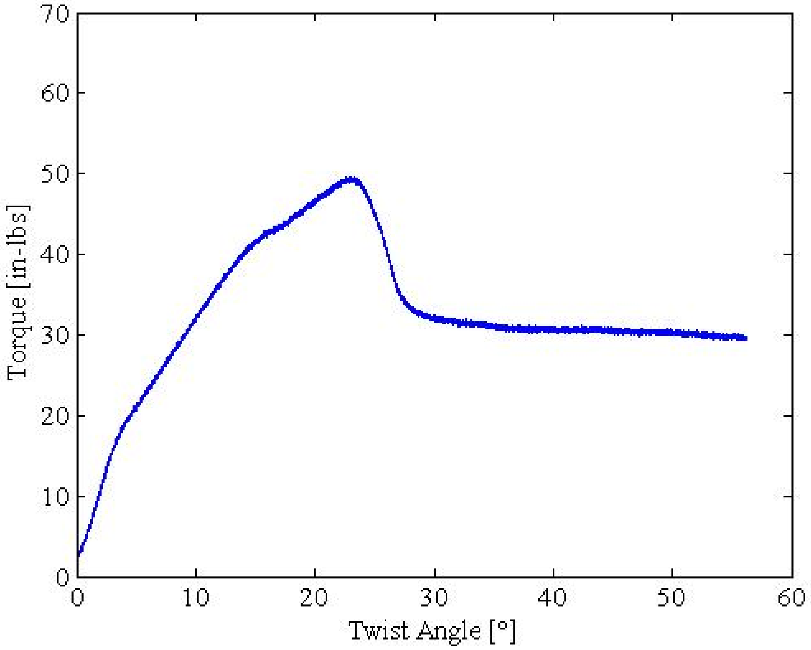

Figure 2.29: USS torsion sample 2 torque versus angular displacement test.

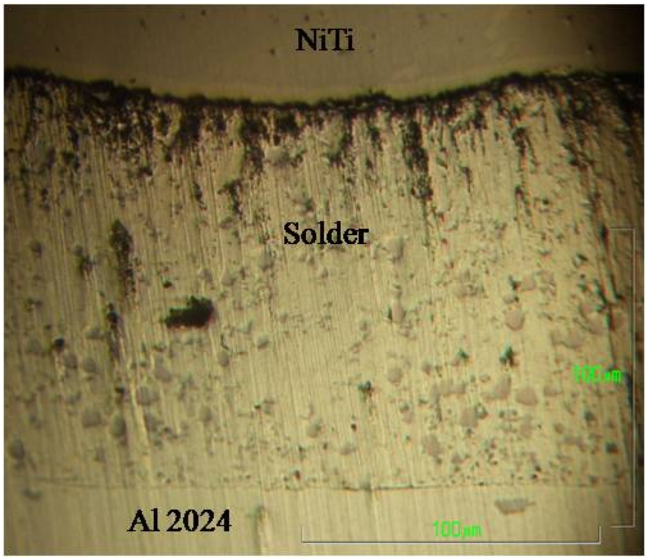

Figure 2.30: USS NiTi/Al 2024 joint cross section.

2.2.3.5 USS Sample Sectioning

Figure 2.30 shows a micrograph of the hot mounted NiTi/Al 2024 USS joint section. The solder joint shows a uniform thickness of 0.005" and maintains intimate contact with both base metals throughout the joint. The joint did not show external signs of cracking, however in some regions, as seen in Figure 2.31, long cracks have developed. The cold mounted joint, however showed no cracking in the main joint area and only a small amount of cracking at the periphery of the sample.

2.3 Discussion of Results

2.3.1 Laser Welding

Several of the initial NiTi/304 SS laser welded tube samples had poor weld quality due to poor dimensional tolerances of the NiTi and 304 SS tubes. After machining the 304 SS pieces, some of the tubes had an eccentricity between the outer diameter

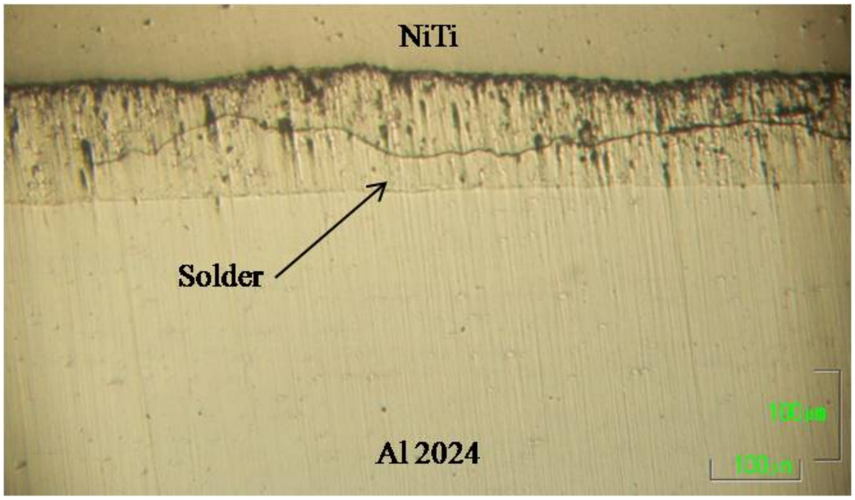

Figure 2.31: USS NiTi/Al 2024 joint cross section.

and inner diameter. This resulted in alignment issues when welding which in turn affected local composition of the weld pool. Often, the deviation from the target 1:1:1 weld pool composition as well as internal stresses caused by welding misaligned pieces resulted in visible cracks appearing after welding, several of which can be seen in sample cross sections such as seen in Figure 2.32.

While some laser weld samples exhibited cracks, all samples remained intact through the welding, sectioning, and mounting processes. Two samples, samples 1 and 5, did not initially exhibit any cracking. The largest penetration noted was approximately 2/3 of the tube wall thickness, 0.022”. By using samples with tighter dimensional tolerances, thicker weld penetration with no cracks should be possible.

The small estimated HAZ in all welds indicates that only a narrow region of the NiTi material next to the weld pool is affected by the laser welding process. The less NiTi that is affected by the welding process, the less effect the process will have on the thermo-mechanical properties of the NiTi piece and active component as a whole.

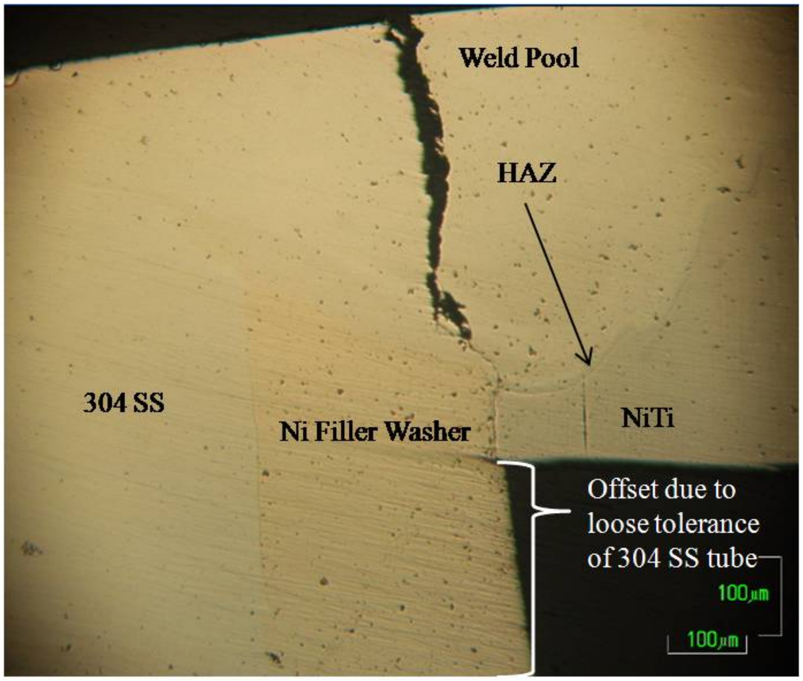
Weld Pool
HAZ
304 SS
Ni Filler Washer
NiTi
Offset due to loose tolerance of 304 SS tube
100µm
100µm

Figure 2.32: Laser weld section showing cracks due to misalignment of NiTi and 304 SS tube walls due to eccentricity in the outer and inner diameters of the 304 SS.

2.3.2 Tungsten Inert Gas (TIG) Welding

The failure of the macro-scale TIG welded NiTi/304 SS samples indicates that there was not sufficient dilution of the weld pool. The behavior of the welds as they cooled suggests that failure is due to cold cracking, crack propagation caused by the formation of Ti-Fe intermetallics and residual stresses. The geometry of the weld likely caused intermetallics to form at the point of contact between the NiTi and 304 SS plates. A new geometry could be designed in which the double-bevel of the 304 SS plate is changed to a flat edge, identical to the NiTi mating plate. This would avoid direct contact of the two plates and allow for more Ni filler to be molten in the weld pool.

2.3.3 Ultrasonic Soldering (USS)

2.3.3.1 Bulk Solder Characterization

The characterization SonicSolder^{TM} shows that the filler metal used in all USS joints is very ductile, typical of soldering filler metals. Since solder joints rely on alloying between the base metals and filler metal as their main mechanism of strength [32], the tensile or shear strength of the bulk solder should be the lower strength limit of a well bonded joint. If joint failure strengths are lower than the bulk solder strength, it may indicate poor adhesion of the solder to one or both base metals.

2.3.3.2 USS Lap Shear Testing

2.3.3.2.1 Passive Metal Lap Shear Tests The results for USS lap shear tests on Al 2024, O1 tool steel, and 304 SS show that surface treatment is a necessary step even though the ultrasonic cavitation of the solder is said to break up and disperses surface oxides and contaminants. All three passive material pairs showed an increase

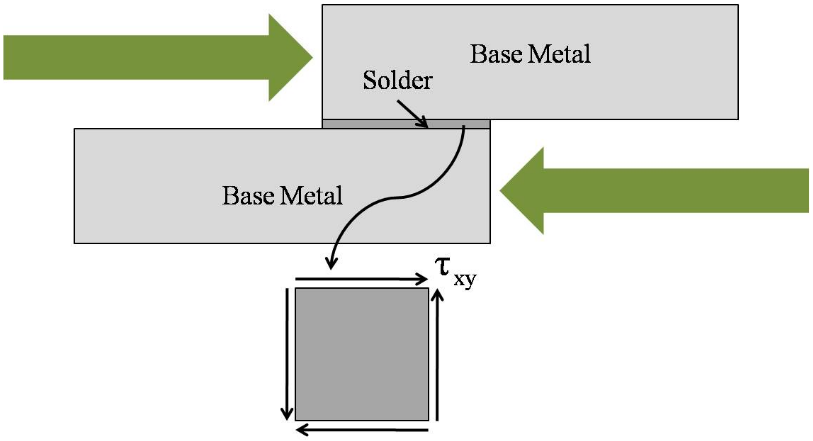

Figure 2.33: Differential element of solder in USS lap shear joints.

in ultimate shear strength and a decrease in their respective coefficients of variance, standard deviation relative to average shear strength, when soldered after being grit blasted with 50 μm SiC and a methanol rinse. This shows that the additional surface preparation made stronger and more consistent joints.

To investigate the nature of the USS bonds, ultimate shear strengths were used to calculate the maximum equivalent von Mises stress for each lap shear sample. The von Mises stress was calculated using 2.1 by considering a differential solder element subject to only pure shear stresses, as seen in Figure 2.33. When subjected to only shear stresses, $\sigma_1, \sigma_2 = \pm\tau_{xy}$, $\sigma_3 = 0$, and the equivalent stress is given by 2.2. The equivalent stresses in Al 2024, O1 tool steel, and 304 SS lap shear joints can be seen in Tables 2.8, 2.9, and 2.10, respectively.

$$\sigma_{eq} = \sqrt{\frac{1}{2}\left[(\sigma_1 - \sigma_2)^2 + (\sigma_2 - \sigma_3)^2 + (\sigma_3 - \sigma_1)^2\right]} \tag{2.1}$$

$$\sigma_{eq} = \sqrt{3}\tau_{xy}. \tag{2.2}$$

Al 2024/Al 2024	Von Mises Equivalent Stress [ksi]	
Sample	No Prep.	Surface Prep.
1	-	18.5
2	17.5	19.1
3	16.2	19.1
4	3.41	19.6
Average	16.9	19.1

Table 2.8: Equivalent stresses in Al 2024 lap shear tests.

O1/O1 tool steel	Von Mises Equivalent Stress [ksi]	
Sample	No Prep	Surface Prep
1	-	9.08
2	5.28	8.57
3	0.94	9.49
4	3.55	
Average	3.26	9.03

Table 2.9: Equivalent stresses in O1 tool steel lap shear tests.

304 SS/304 SS	Von Mises Equivalent Stress [ksi]	
Sample	No Prep	Surface Prep
1	1.92	10.5
2	0.59	8.02
3	0.45	5.05
4	-	
Average	0.99	7.85

Table 2.10: Equivalent stresses in 304 SS lap shear tests.

Using the equivalent and qualitative observation of fracture surfaces, a determination can be made as to how the solder joint failed; in an adhesive or cohesive mode. If the calculated equivalent stress is significantly less than the bulk tensile strength of SonicSolder^{TM}, it indicates that the failure did not occur within the solder itself but rather at the interface of the solder and base metal; an adhesive failure. This can be corroborated if a fracture surface shows a significant amount bare base metal. If both base metal pieces still have solder on the faying surfaces after testing, this indicates that the joint failed cohesively, a failure of the bulk solder between the base metal pieces.

In considering surface preparation, the Al 2024 joints show a marginal increase in maximum equivalent stress; however both joint sets indicate a cohesive failure mode with equivalent stresses in excess of the solder ultimate tensile stress and solder covered fracture surfaces. For O1 tool steel and 304 SS samples, the difference between the strengths of joints with without surface treatments is clearly delineated between adhesive and cohesive failures. Without surface treatment, the equivalent stresses are significantly lower than the strength of the bulk solder and fracture surfaces show large areas of bare base metal. However, with surface treatment, both steel base metals have an average equivalent stress greater than the ultimate tensile strength of the solder.

Both the O1 tool steel and 304 SS lap shear samples are significantly weaker than Al 2024 lap shear samples. The lower strengths seen in the O1 tool steel and 304 SS lap shear specimens without surface treatment may be due to the nature of the surface oxides and hardness of the underlying base metal. When cavitations implode and impinge on Al 2024, the impingements are causing deformation of the Al 2024 under the aluminum oxide layer. The deformation of the supporting base material causes the brittle oxide layer to crack and exposes nascent surfaces of the base metal. Steel alloys typically have elastic moduli three times larger than aluminum alloys. This indicates that the O1 and 304 SS samples would not have deformed as much while being impinged upon from solder cavitations. With less deformation there would likely be less disruption of the oxide surface revealing less nascent metal surface area with which the solder can alloy.

Even with surface treatment, O1 tool steel and 304 SS lap shear joints are still significantly weaker than Al 2024 joints. This may be due to the nature of the alloying between the filler metal and different base metals. Filler metal-base metal alloying is a key component in the strength of solder and braze joints [30, 32]. The Al 2024 lap shear joints are likely the strongest of the three base metal joints because the composition of SonicSolder^{TM} contains a percentage of aluminum. With O1 tool steel and 304 SS, base metal alloying may increase adhesive strength, but the composition of each material may allow for the formation of intermetallic compounds at or near filler metal-base metal interfaces. Where Al may have made the Al 2024 lap joints stronger, Al-Fe intermetallics such as $FeAl_3$ and $FeAl_5$ [27, 28] may create stress concentrations and act as crack initiation points in the steel solder joints.

2.3.3.2.2 NiTi Lap Shear Tests Of all NiTi containing joints, the NiTi/NiTi lap shear joint had the lowest average ultimate shear strength but also had the second lowest coefficient of variance. Furthermore, the calculated equivalent stresses for NiTi/NiTi lap shear joints are near the ultimate tensile strength of bulk SonicSolder^{TM}, as seen in Table 2.11. This may indicate that the solder is not alloying with the NiTi

NiTi	Von Mises Equivalent Stress [ksi]			
Sample	NiTi	Al 2024	O1	304 SS
1	7.67	13.0	10.1	11.8
2	7.14	14.5	7.47	9.13
3	8.52	13.0	10.4	9.68
Average	7.78	13.5	9.34	10.2

Table 2.11: Equivalent stresses in NiTi containing lap shear tests.

or may be forming adverse intermetallic compounds in the solder joint. The other NiTi/base metal pairs show an increase in equivalent stress over the NiTi/NiTi joints.

In joining NiTi to Al 2024, the average shear strength, see in Table 2.7, decreased relative to the Al 2024/Al 2024 joints but increased relative to the NiTi/NiTi joints. A similar comparison for both O1 tool steel and 304 SS containing joints show that the NiTi/passive steel joints have a higher strength than the like base metal joints, O1/O1 tool steel, 304 SS/304 SS, and NiTi/NiTi joints. The coefficients of variance for the steel containing pairs are again the highest of all material pairs. The large coefficients of variance indicate that the strengths for any steel containing lap shear joints are statistically equivalent.

One aspect that concerns the NiTi/passive metal USS joints is the residual stresses due to differential thermal expansion and contraction. Evidence of the residual stresses is seen in the section of a NiTi/Al 224 USS joint shown in section 2.2.3.5. The NiTi/Al 2024 sectioned joint showed several long cracks throughout the joint. These cracks likely occurred due to differential contraction of the NiTi and Al 2024 pieces as they cooled below the melting point of the solder. It assumed that similar cracks appear in the lap shear samples with dissimilar base metals. These long cracks would act as stress concentrators and fracture initiation points resulting in premature failure of the joint.

These findings are applied to the lap shear USS joints containing NiTi and a passive metal in order to estimate the residual stresses in the solder. Stress in the outer fiber of the passive metal, denoted σ_p is calculated by 2.3 and the stress in the outer fiber of the NiTi piece, σ_{NiTi}, is given by 2.4 [37]. These calculations consider bimetal systems, however, they do not take into account the non-linear stress-strain curve of the NiTi material. For this initial analysis, the NiTi is instead treated as a linear elastic material with an elastic modulus equal to E_M. Material properties used in calculating residual stresses are seen in Table 2.12. The stresses are considered to develop when the joint cools from 231 °C, the melting point of SonicSolder^{TM}, [31], to 20 °C.

$$\sigma_p = \frac{-\left(\alpha_{NiTi} - \alpha_p\right)\left(\Delta T\right) E_p}{K_1} \left[3\frac{t_p}{t_{NiTi}} + 2\left(\frac{t_p}{t_{NiTi}}\right)^2 - \frac{E_{NiTi} t_{NiTi}}{E_p t_p} \right], \tag{2.3}$$

and

$$\sigma_{NiTi} = \frac{-\left(\alpha_p - \alpha_{NiTi}\right)\left(\Delta T\right) E_p}{K_1} \left[3\frac{t_p}{t_{NiTi}} + 2 - \frac{E_p}{E_{NiTi}}\left(\frac{t_p}{t_{NiTi}}\right)^3 \right], \tag{2.4}$$

where

$$K_1 = 4 + 6\frac{t_p}{t_{NiTi}} + 4\left(\frac{t_p}{t_{NiTi}}\right)^2 + \frac{E_p}{E_{NiTi}}\left(\frac{t_p}{t_{NiTi}}\right)^3 + \frac{E_{NiTi}}{E_p}\frac{t_{NiTi}}{t_p}. \tag{2.5}$$

By assuming a linear stress gradient from the outer fiber of the passive material and outer fiber of the NiTi in each joint, the stress at the middle of the solder joint was calculated by interpolating the stress at 0.3765" from the outer fiber, $t_p + t_{solder}/2$, of the passive material, as seen in 2.6. The resulting estimated residual stresses are seen in Table 2.13. If the shape memory properties of the NiTi were considered the

Material	NiTi	Al 2024	O1 tool steel	304 SS
t [in]	0.250	0.375	0.375	0.375
α [°C^{-1}]	10.0×10^{-6} [23]	23.2×10^{-6} [16]	11.0×10^{-6} [5]	17.3×10^{-6} [13]
E [ksi]	3770 [12]	9860 [16]	30000 [5]	29000 [13]

Table 2.12: Material properties used to calculate thermally induced stresses in USS joints.

Mating metal	Al 2024	O1 tool steel	304 SS
σ_p[ksi]	-7.73	-1.15	-8.42
σ_{NiTi}[ksi]	-0.79	-0.33	-2.42
σ_{solder}[ksi]	-3.57	-0.66	-4.82

Table 2.13: Thermally induced stresses in NiTi containing USS lap shear joints.

resulting residual stresses would be less than the stresses calculated using linear elastic NiTi due to the detwinning stress plateau in the NiTi stress-strain curve.

$$\sigma_{solder} = \left(\frac{\sigma_{NiTi} - \sigma_p}{t_p + t_{NiTi} + t_{solder}} \right) (t_p + t_{solder}/2) + \sigma_p. \tag{2.6}$$

The resulting compressive stresses for the NiTi/passive material USS lap shear joints would increase the equivalent stresses experienced in the solder joint, however due to the linear estimation of NiTi portion of the joints, this calculation is reserved until further modeling of the system is accomplished.

2.3.3.3 USS Torsional Shear Testing

The initial test on USS torsion sample 1 generated the highest torque, 67.3 in-lbs. The second torsion test did not generate a higher torque indicating that failure initiated as the first test ended. For further consideration, only the first test of sample

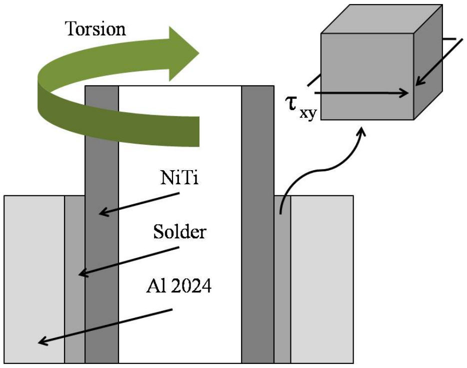

Figure 2.34: Differential element of solder in USS torsion joints.

1 is considered. Torsion sample 2 did fail at the short saddle set, as desired, however the largest experienced torque was only 49.6 in-lbs.

The NiTi/Al 2024 torsional test specimens were considered using von Mises equivalent stresses. A differential solder element in the torsional joint was considered loaded as seen in Figure 2.34. Since the portions of the tubes soldered to the saddles were constrained in their angular deflection, the shear stress was calculated as direct shear rather than torsional shear. Using the surface area of the tinned NiTi tube, equation 2.7, and the peak applied torque divided by the tube radius, 2.8, a maximum torsional stress, τ_{xy}, was calculated by 2.9 and found to be 4.26 ksi for sample 1 and 3.14 ksi for sample 2.

$$A = C \times L = \pi d L \tag{2.7}$$

$$F = \frac{T}{r} \tag{2.8}$$

$$\tau_{xy} = \frac{F}{A} \tag{2.9}$$

The applied axial force resulted in a small shear stress when compared to the shear stress due to applied torque and was therefore ignored in calculating equivalent stresses. Similar to the lap shear joints in section 2.3.3.2.1, the differential element is considered to be subject only to shear stress, τ_{xy}, giving the equivalent stress, $\sigma_{eq} = \sqrt{3}\tau_{xy}$, as calculated in 2.1. The maximum equivalent stresses are found to be 7.38 ksi for torsion sample 1 and 5.44 ksi for torsion sample 2.

The average ultimate tensile stress from the bulk SonicSolder^{TM} tests was 7.80 ksi, as seen in Table 2.3. While the equivalent stress of torsion sample 1 gives a maximum equivalent stress close to the ultimate tensile strength of SonicSolder^{TM}, the average maximum equivalent stresses the of NiTi/Al 2024 lap shear samples, which has a similar differential element, was 13.5 ksi, as seen in Table 2.11, significantly greater than ultimate tensile strength of the bulk solder.

An explanation for the discrepancy of equivalent stresses between the torsional and lap shear NiTi/Al 2024 samples is the method for creating the different joints. The lap shear joints had two flat regions tinned with the EWI USS system while the torsional samples had a convex round surface and concave round surface tinned with a commercial USS system. The commercial system has a smaller tip on the soldering iron but is still designed for soldering flat regions. In attempting to solder the convex surfaces of the saddles, it is likely that the entire surface was not subject to the ultrasonic impingement by the solder cavitations. This would explain both the lower than expected equivalent stresses as well as the variation between the two torsional samples.

In addition to the torsional joint manufacturing issues, the differential thermal contraction of the NiTi and Al 2024 in the torsional joint would have acted differently upon the differential solder element of the torsional joint than that of the lap shear joint. Once joined at temperature, the Al 2024 saddles would contract more than the NiTi tube, creating compressive stresses in the solder in a radial direction. Similar to the lap shear samples, the compressive stress would result in a higher equivalent stress, however without modeling the strain response of the NiTi tube, the equivalent stress calculations would not be accurate.

2.3.3.4 USS Sample Sectioning

The difference in the amount of cracking between the hot and cold mounted USS sections indicates that the mounting process may exacerbate the cracking present due to differential thermal expansion. In the hot mounting process, the sample is heated to a substantial fraction of the melting point of the solder and then is cooled using cold water. This thermal shock likely causes crack growth in the sample, but as observed in the cold mounted sample, cracking is still evident when the hot mounting process is not used. These indicates that the differential thermal expansion of the base metal pieces may be causing initial cracking in the solder joint as it cools, though the extent of the cracking requires further investigation.

CHAPTER 3

NITI/AL COMPOSITES BY ULTRASONIC CONSOLIDATION

3.1 Ultrasonic Additive Manufacturing (UAM) Composite Characterization Methods

3.1.1 Al 3003 H-18 Matrix

Test samples were constructed to measure the bulk mechanical properties of the aluminum matrix in UAM composites. Samples created for mechanical testing are identified by an indicial notation based upon the orientation of the test load relative to the direction of the ultrasonic weld and the type of applied load, as displayed in Figure 3.1. For this convention, a 3-D axis is oriented with the +x direction running parallel to the weld path, the +y direction parallel to the baseplate and perpendicular to the weld direction, and the +z direction starting orthogonal to the baseplate and extending upwards through the UAM layers. The first index, i, indicates whether the applied load is oriented along the x, y, or z axis. The second index, j, indicates what type of load is applied to the sample: 1 indicates a shear load, 2 indicates a tensile load, and 3 indicates a compressive load.

Three types of UAM samples were created to test the bulk properties of an Al 3003-H18 UAM matrix; shear samples (1-1) were designed to test the shear strength

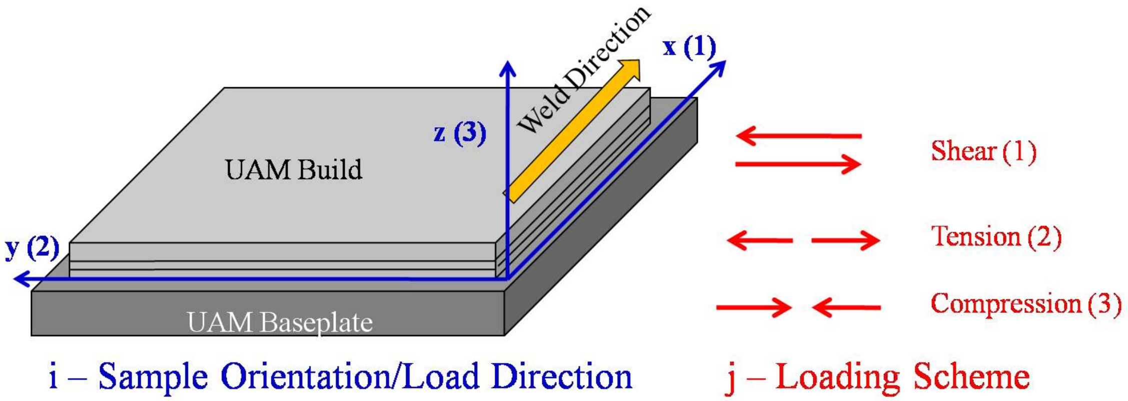
Weld Direction
x (1)
z (3)
UAM Build
y (2)
UAM Baseplate
Shear (1)
Tension (2)
Compression (3)
i – Sample Orientation/Load Direction
j – Loading Scheme

Figure 3.1: UAM sample identification convention.

of a weld interface, transverse tensile samples (3-2) were designed to test the tensile strength of the samples perpendicular to the weld interface, and longitudinal tensile samples (1-2) were designed to test the sample tensile strength parallel to the ultrasonic welds. These orientations were identified as common modes of failure for long fiber reinforced matrices [3]. For all samples, a UAM block was created by successively welding 0.006" thick Al 3003-H18 tapes on an solid Al 3003-H14 baseplate. Each tape was subject to two passes, a tack pass and a final weld pass. Process parameters for each pass are seen in Table 3.1. Each sample was machined from the resulting UAM block by using both integrated and off-line subtractive processes.

Parameter	Tack Pass	Weld Pass
Normal Force [lbs]	78.7	224.8
Amplitude [in]	10.2×10^{-4}	4.7×10^{-4}
Weld Speed [in/s]	1.1	1.3

Table 3.1: UAM process parameters for matrix mechanical testing samples.

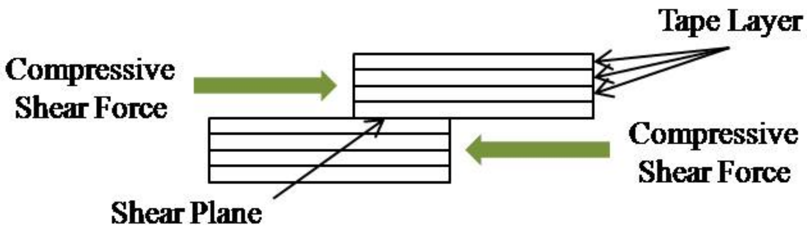

Figure 3.2: Tape and load orientation of 1-1 UAM samples.

3.1.1.1 Shear (1-1) Testing

3.1.1.1.1 Sample Creation 1-1 specimens were built such that a tape interface was along the shear plane, as seen in Figure 3.2. The sample is designed similar to the SonicSolder^{TM} shear specimen and USS lap shear specimens. Nominal dimensions for 1-1 UAM samples are shown in appendix A.

While UAM 1-1 samples originally were machined as seen in Figure 3.3 (a), two UAM 1-1 samples, 1 and 2, were further modified to reduce the shear area. The resulting samples, seen in Figure 3.3 (b), have a nominal shear plane width of 0.250" giving a resulting shear area of 0.125 in^2. This modification was initially thought to be necessary in order to load the samples until failure using given equipment. Using the bulk shear strength of solid Al 3003 H-18, 16 ksi [16], the required force to shear the modified samples was estimated to be 2000 lbs. Upon testing of the 1-1 samples, a lower than expected ultimate shear stress was found. Due to the lower than expected shear stress, the remaining samples, 3 and 4, were tested without additional modifications to avoid possible damage from additional machining processes. Final design dimensions of both types of 1-1 specimens tested can be seen in appendix A.

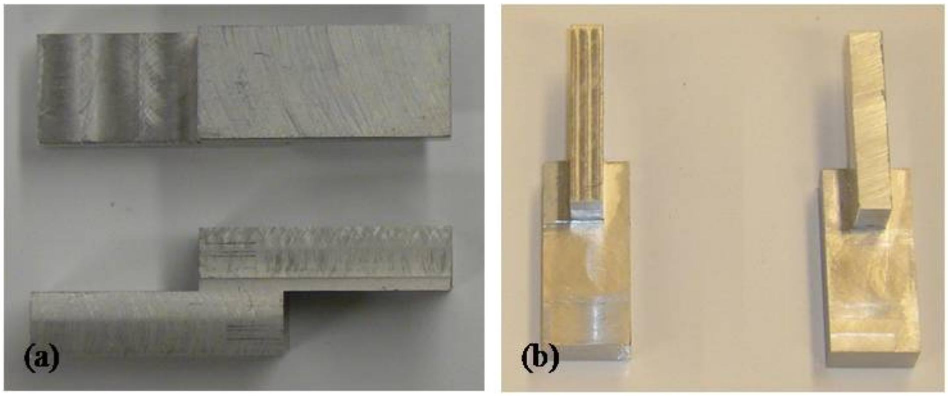

Figure 3.3: UAM 1-1 samples (a) nominal dimensions and (b) reduced shear area modified in anticipation of high shear strength of UAM bond.

3.1.1.1.2 Sample Testing Testing was performed by placing the samples in the same shear jig used for USS bulk solder shear and lap shear testing, described in section 2.1.3.2.2 and appendix A. Test specimens were loaded in compression under displacement control until failure. Displacement was controlled by a ramp with an average rate of 0.01 in/s. During testing, displacement was measured by the LVDT integrated in the load frame and applied force was measured using a load cell placed in series with the load train.

3.1.1.2 Transverse Tensile (3-2) Testing

3.1.1.2.1 Sample Creation 3-2 specimens were built such that tape interfaces were perpendicular to the applied axial force, as seen in Figure 3.4. Nominal dimensions 3-2 UAM samples are seen in appendix A. The additional material on the bottom grip portion of the 3-2 samples is part of the UAM baseplate that was not removed. The addition of the solid baseplate does not have an effect on the gauge

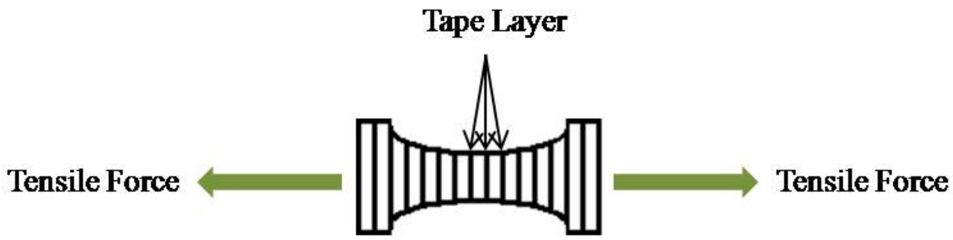

Figure 3.4: Tape and load orientation of 3-2 UAM samples.

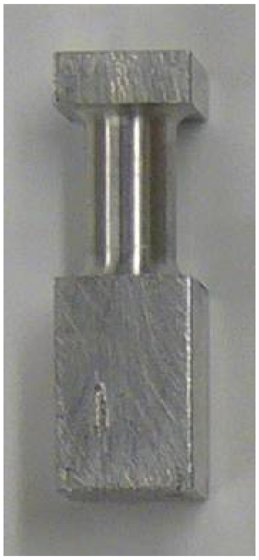

Figure 3.5: 3-2 UAM test specimen.

region nor was it under load during testing. Therefore, the incorporation of the baseplate does not affect obtained mechanical values. A picture of a typical transverse tensile specimen is seen in Figure 3.5.

3.1.1.2.2 Sample Testing Tensile strength tests were performed on the 3-2 samples. The same grips used in the SonicSolder^{TM} tensile tests, section 2.1.3.1.2, were

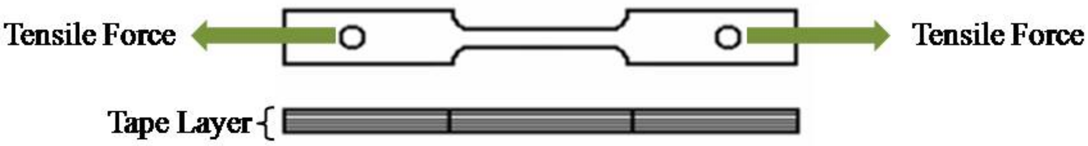

Figure 3.6: Tape and load orientation of 1-2 UAM samples.

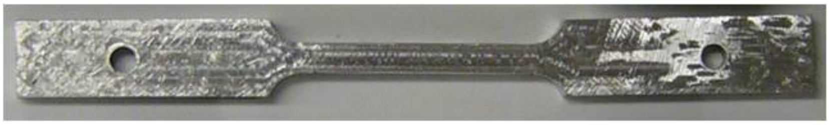

Figure 3.7: 1-2 UAM test specimen.

used to place the 3-2 UAM samples under tensile stress. The tensile grip design can be seen in appendix A. Samples were axially loaded under displacement control until failure. Displacement was controlled by a ramp with an average rate of 0.01 in/s. During testing, displacement was measured by the LVDT integrated in the load frame and applied force was measured using a load cell placed in series with the load train.

3.1.1.3 Longitudinal Tensile (1-2) Testing

3.1.1.3.1 Sample Creation 1-2 specimens were built with tape interfaces parallel to the applied axial force as seen in Figure 3.6. Nominal dimensions of transverse tensile specimens can be seen in appendix A. A picture of a typical transverse tensile specimen is seen in Figure 3.7.

3.1.1.3.2 Sample Testing Tensile strength tests were performed on the 1-2 UAM samples. Specimens were placed in pin grips and loaded axially under displacement control until failure. Displacement was controlled by a ramp with an average rate of 0.02 in/s. During testing, displacement was measured by the LVDT integrated in the load frame and applied force was measured using a load cell placed in series with the load train.

3.1.1.4 UAM Bond Characterization

Optical micrographs of UAM fracture surfaces and were analyzed using ImageJ. Fracture surface micrographs were taken from UAM 1-1 and 3-2 samples under 4X and 10X magnification. A common nominal threshold was applied to all micrographs and results were used to determine the percentage of bond area with respect to total sample area.

3.1.2 Nickel-Titanium

In order to characterize the NiTi alloy used in UAM composites, 90 °C Flexinol, a 0.015” diameter NiTi wire was connected as part of a Wheatstone bridge and placed under mechanical and thermal loading conditions. Voltage change of the bridge was measured using a Vishay signal conditioning amplifier. The amplifier output, proportional to the resistance of the NiTi wire, was monitored while the NiTi wire was thermally cycled from approximately 20 °C to 160 °C both unloaded and under a static 2.7 lbs (12 N) axial load. From the experiment, transition temperatures, stress influence coefficients, and electrical resistivities of the austenite and martensite phases of the NiTi alloy were obtained.

3.1.3 NiTi/Al Composite

3.1.3.1 Sample Construction

Two active composites with 4.5% and 13.4% NiTi cross sectional area ratios were constructed using the 10 kW UAM test bed system at EWI. This system allows for the embedding of up to 0.008” (203 μm) diameter NiTi wires solely through plastic flow of the Al matrix material. This increase in embedding capability it due mostly to the increase in available power. The active composites were created using a normal force of 1200 lbs, vibration amplitude of 11.0×10^{-4} in and a weld speed of 1.4 in/s. The 4.5% and 13.4% composites have eight 0.004” (100 μm) diameter and six 0.008” diameter wires, respectively, embedded between two Al 6061 tapes.

To make each composite, detwinned martensitic NiTi wires were aligned in a set of wire clamps fastened to an alignment plate, as seen in Figure 3.8. The orange material seen in between the grips is a silicon rubber used to help hold the NiTi wires in place during alignment and during the UAM process. A modified baseplate, as seen in Figure 3.9, had two Al 6061 tapes welded onto the sacrificial portion of the plate. The wire clamps were then removed from the alignment plate and placed on the Al 3003 H-14 baseplate with the wires aligned over the previously welded Al 6061 tapes. A final Al 6061 tape was then welded over top of the wires to complete the embedding process.

Both embedded builds were removed with their sacrificial baseplates from the main baseplate, Figures 3.10 and 3.11, to be machined to final dimensions. Both composite samples were machined into dog bone shaped specimens, as seen in Figure 3.12, with gauge width and thicknesses of 0.125” and 0.015”, respectively, resulting in the 4.5% and 13.4% NiTi cross sectional area ratios.

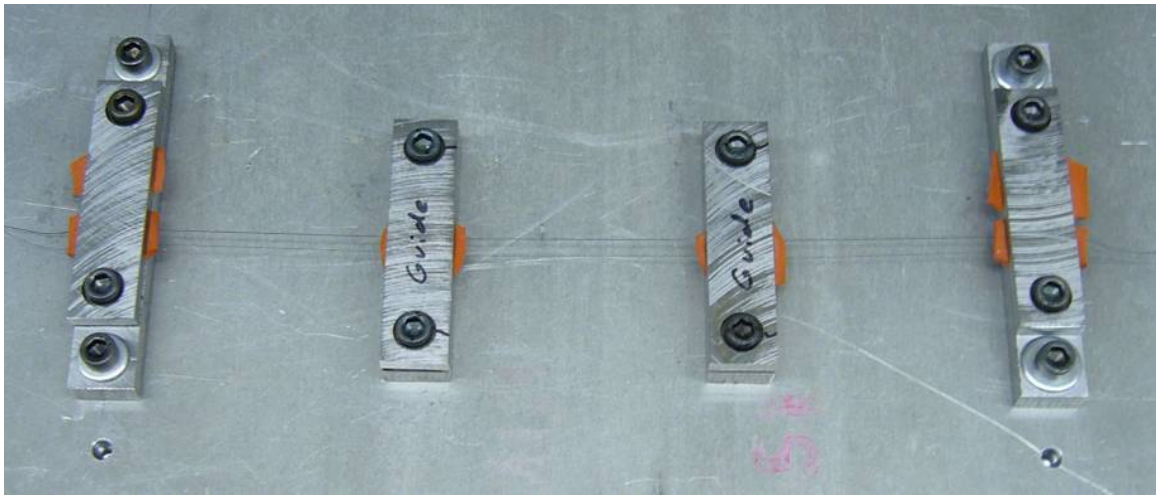
Guide
Guide

Figure 3.8: UAM embedded wire grips holding and alignment plate.

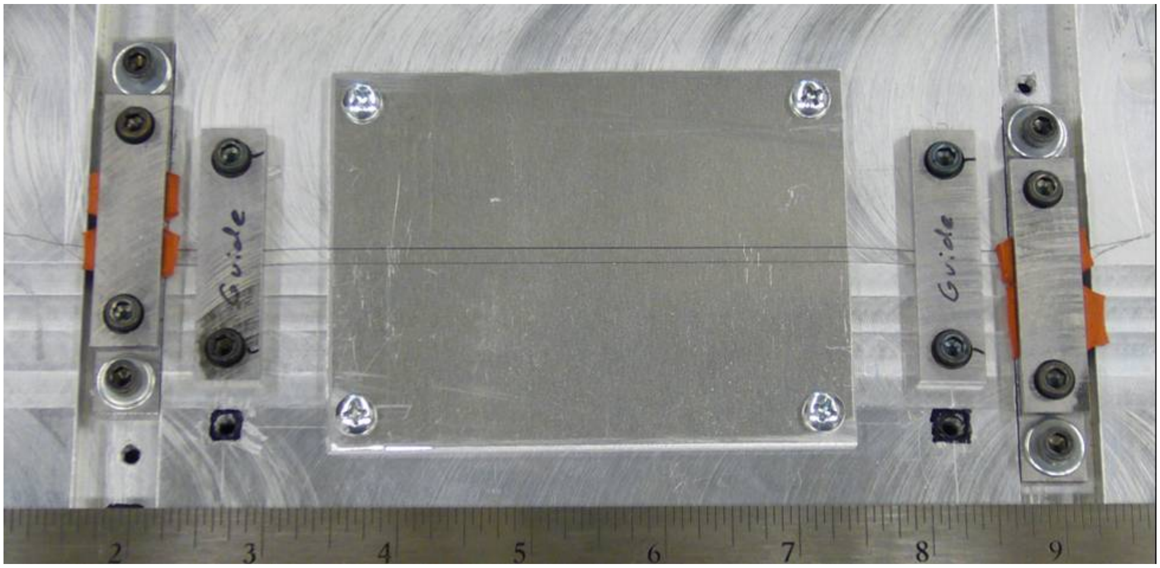
Guide
Guide
2
3
4
5
6
7
8
9

Figure 3.9: UAM embedding baseplate with sacrificial baseplate and NiTi wire grips.

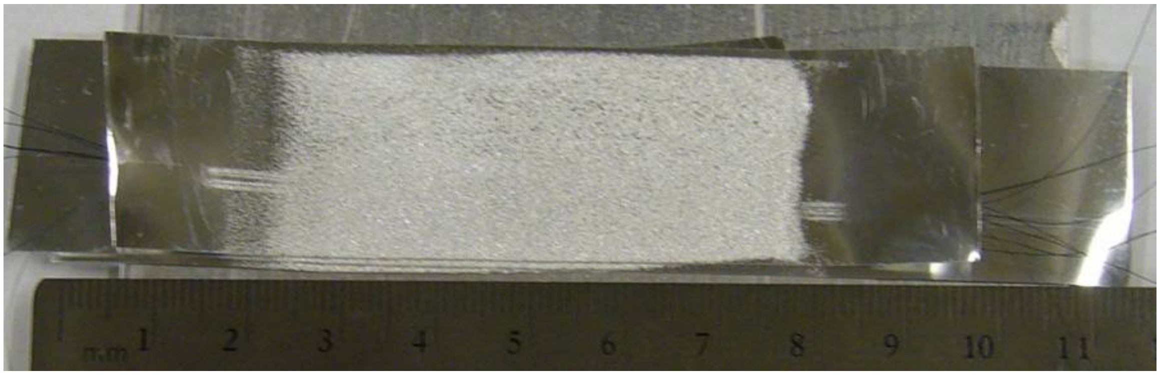

Figure 3.10: UAM NiTi/Al 6061 composite with eight embedded 0.004” diameter NiTi wires.

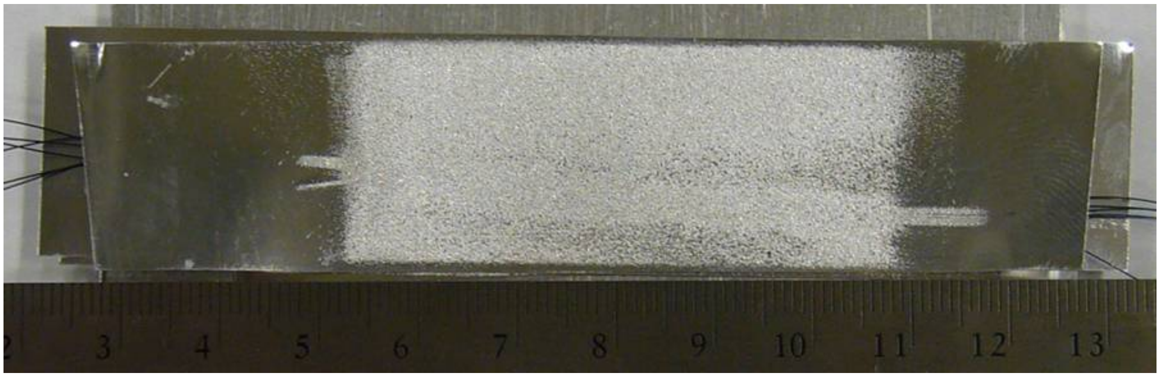

Figure 3.11: UAM NiTi/Al 6061 composite with six embedded 0.008” diameter NiTi wires.

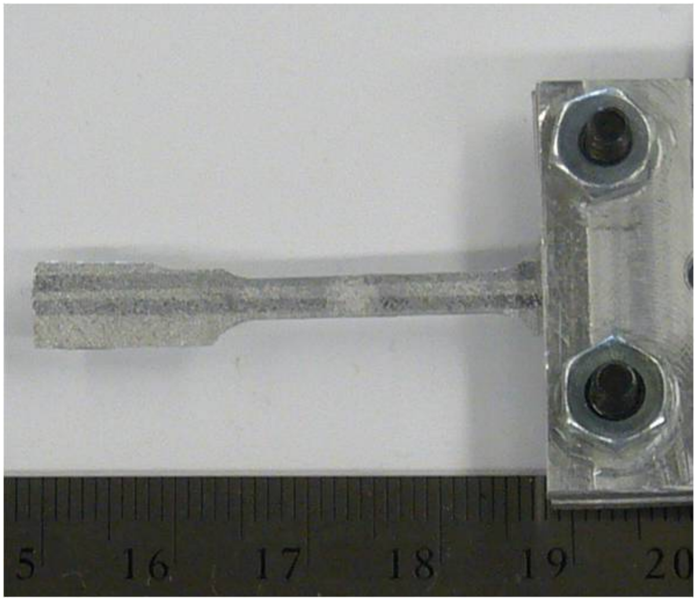

Figure 3.12: UAM NiTi/Al 6061 composite dog bone sample with 4.5% NiTi cross sectional area ratio.

UAM composite NiTi area ratio is defined by:

$$Area\ \ Ratio = \frac{A_{NiTi}}{A_{total}} \tag{3.1}$$

where

$$A_{NiTi} = n\frac{\pi d^2}{4} \tag{3.2}$$

and

$$A_{total} = w \times t. \tag{3.3}$$

For these equations, n is the number of wires, d is the diameter of the wires, w is the width of the composite gauge region, and t is the thickness of the gauge region.

3.1.3.2 Composite Stiffness Testing

Composite stiffness experiments were conducted to test the accuracy of the composite stiffness model, described in section 3.3, and demonstrate proof of the active stiffness concept. During the stiffness experiments, both embedded composites were tested by suspending them vertically and applying a fixed static load of 4.5 lbs (20 N) along the 1-2 orientation. Strain measurements were made at room temperature and again at an elevated temperature of approximately 150 °C to ensure transformation of the embedded NiTi. For each sample the applied load was cycled multiple times at room temperature and at elevated temperature. The displacement data from an MTS 634.31 extensometer was then used to calculate the stiffness of the sample.

3.2 Ultrasonic Additive Manufacturing (UAM) Composite Characterization Results

3.2.1 Al 3003 H-18 Matrix

3.2.1.1 Shear (1-1) Testing

Table 3.2 shows the ultimate shear stresses for all 1-1 UAM samples. As seen from the results, the average ultimate shear stress is 7.64 ksi with a C_v of 16.6%. A typical force versus displacement plot for a 1-1 UAM test is seen in Figure 3.13. Additional 1-1 force versus displacement plots can be seen in appendix D.

Sample	Ultimate Shear Stress [ksi]
1	9.04
2	7.92
3	5.96
4	7.63
Average	7.64
Standard Deviation	1.27
C_v	16.6%

Table 3.2: 1-1 UAM specimen testing results.

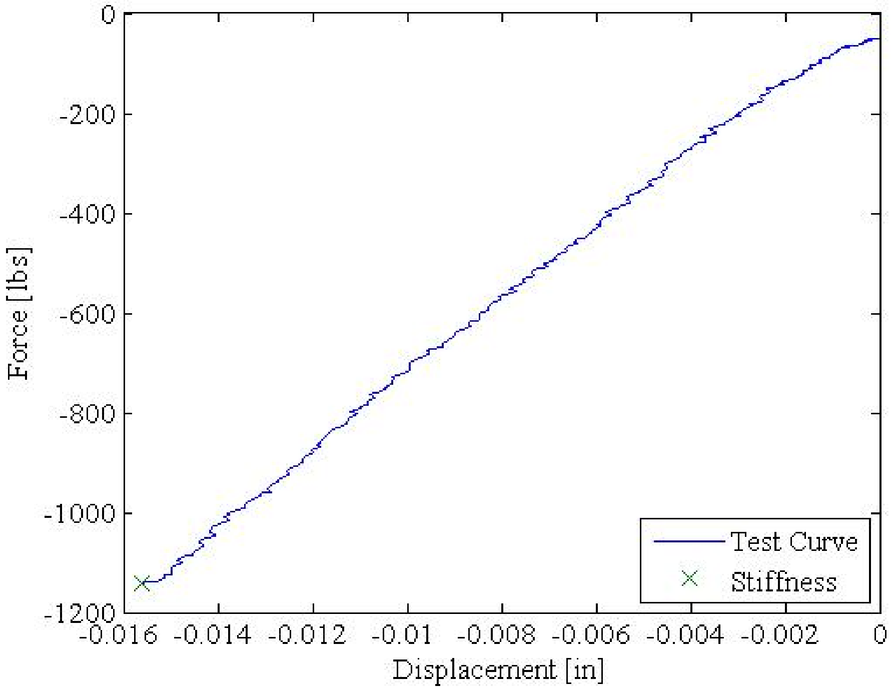

Figure 3.13: UAM 1-1 sample 1 force versus displacement test plot.

3.2.1.2 Transverse Tensile (3-2) Testing

Table 3.3 shows values the ultimate transverse tensile stress for all 3-2 UAM samples. As seen from the results, the average ultimate transverse tensile stress is found to be 4.34 ksi with a C_v of 9.45%. For statistical analysis, samples 3 and 6 were excluded as outliers. The exclusion of samples 3 and 6 is discussed in section 3.4. A typical force versus displacement plot for a 3-2 UAM test is seen in Figure 3.14. Additional 3-2 force versus displacement plots can be seen in appendix D.

Sample	Ultimate Transverse Tensile Stress [ksi]
1	4.12
2	4.52
3	3.72
4	4.16
5	4.66
6	2.77
7	3.72
8	4.83
Average	4.34
Standard Deviation	0.41
C_v	9.45%

Table 3.3: 3-2 UAM specimen testing results.

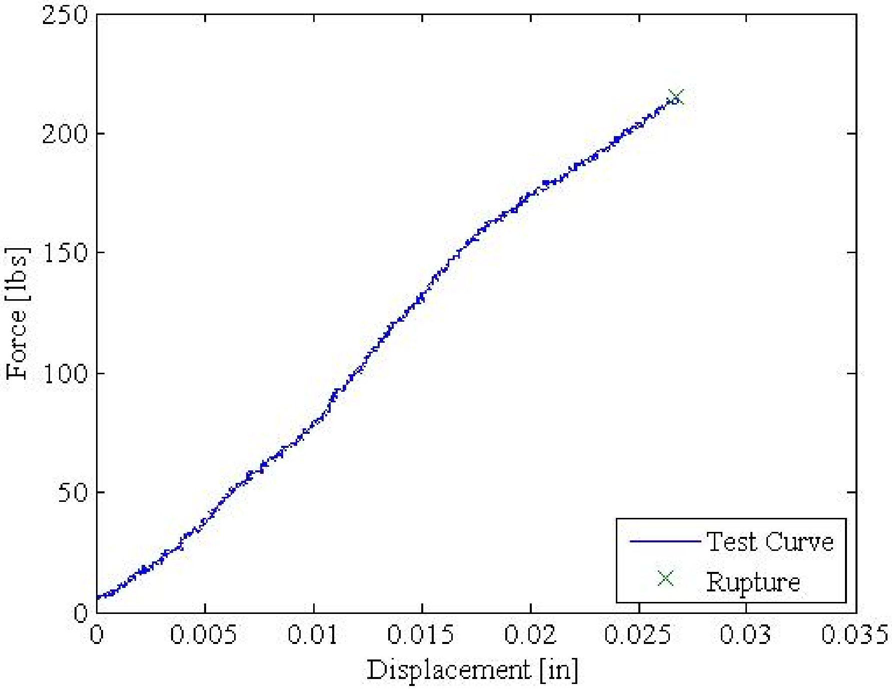

Figure 3.14: UAM 3-2 sample 4 force versus displacement test plot.

3.2.1.3 Longitudinal Tensile (1-2) Testing

Table 3.4 shows values the result for ultimate longitudinal tensile stress for all tested 1-2 UAM samples. As seen from the results, the average ultimate longitudinal tensile stress was found to be 34.2 ksi with a C_v of 2.46%. A typical force versus displacement plot for a 1-2 UAM test is seen in Figure 3.15. Additional 1-2 force versus displacement plots can be seen in appendix D.

Sample	Ultimate Longitudinal Tensile Stress [ksi]
1	32.8
2	34.5
3	34.9
4	34.6
5	34.0
Average	34.2
Standard Deviation	0.84
C_v	2.46%

Table 3.4: 1-2 UAM specimen testing results.

3.2.1.4 UAM Bond Characterization

The results for shear and transverse fracture surface analysis are seen in Table 3.5. As seen in the table, UAM samples have an average bonded area of 66% with a C_v of 2.1%. A sample micrograph before and after applying the image analysis threshold can be seen in Figures 3.16 and 3.17, respectively.

3.2.2 Nickel-Titanium

As shown in Figure 3.18, the resistance response of the NiTi wire is such that regardless of load, the wire exhibits a change in resistance of -3% after transformation

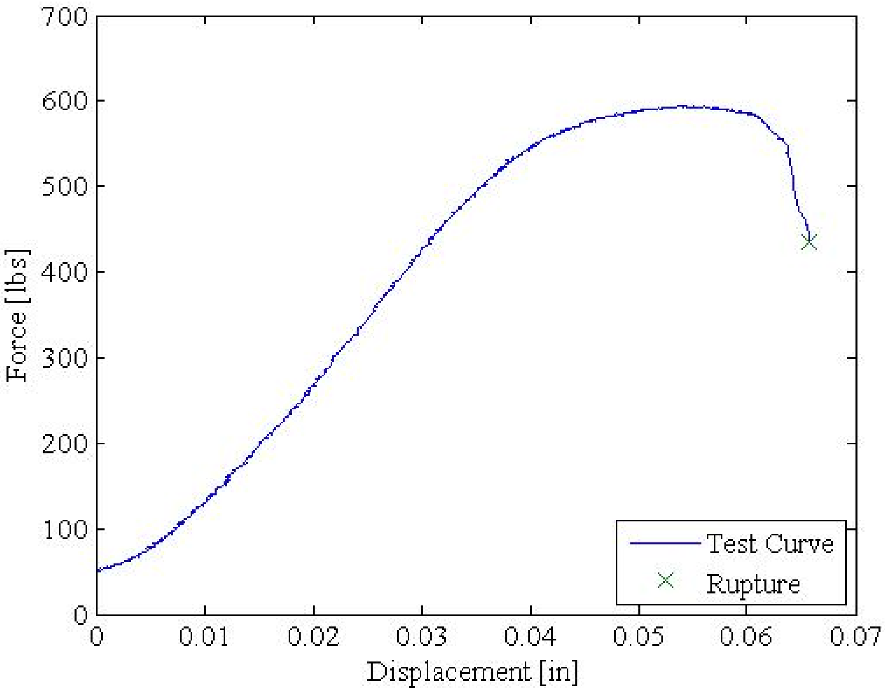

Figure 3.15: UAM 1-2 sample 1 force versus displacement test plot.

to the austenite phase from the room temperature martensite phase. The effect of load is to shift the A_s and A_f temperatures, changing the temperature at which the M-A transition and subsequent large resistance drop take palce, as indicated by the red circle trend. For this particular alloy, the load appears to have little effect on the temperature range at which the A-M transition and subsequent increase in resistance occurs, as indicated by the blue triangle trend. From these experiments, the transition temperatures, their stress influence coefficients, and electrical resistivities were determined, as seen in Table 3.6, for use in the composite models described in section 3.3. The value for C_m was approximated such that load has little effect on the A-M transition as demonstrated in the experiment.

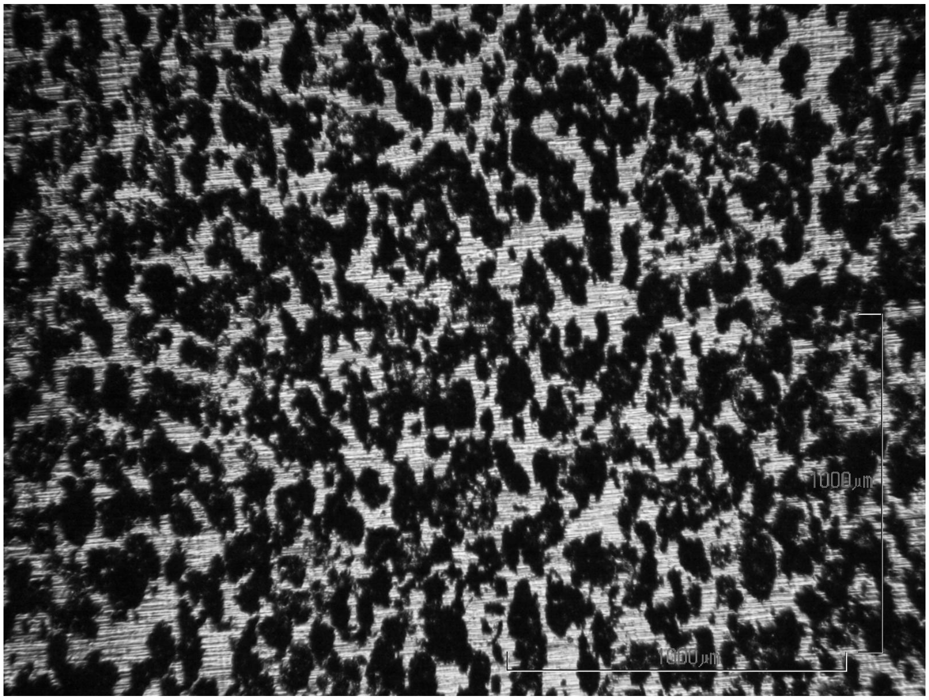

Figure 3.16: UAM 3-2 sample 8 fracture surface before image processing, dark regions are previously bonded regions.

3.2.3 NiTi/Al Composite

3.2.3.1 Composite Stiffness Testing

Initial composite stiffness testing results are shown in Table 3.7. The results show that for the 4.5% area ratio composite, a 6.0% decrease in stiffness relative to room temperature stiffness was observed while the 13.4% area ratio composite exhibited a 5.5% increase in stiffness relative to its room temperature stiffness.

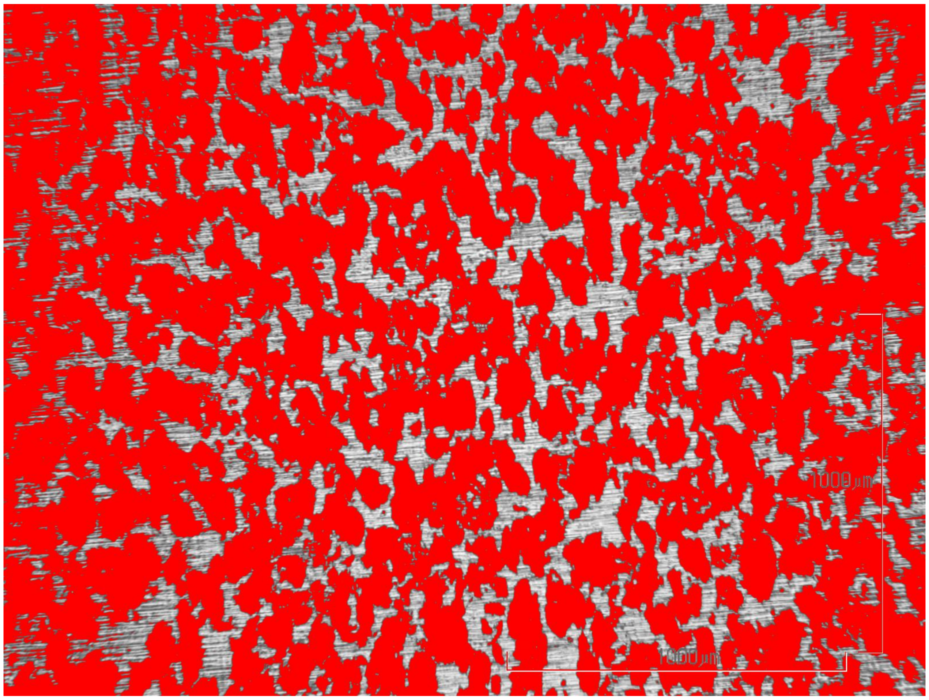

Figure 3.17: UAM 3-2 sample 8 fracture surface after image processing, red regions are bond fracture surfaces.

3.3 Ultrasonic Additive Manufacturing (UAM) NiTi/Al Composite Modeling

3.3.1 Constitutive Modeling

Using the material properties obtained from the NiTi characterization experiment, Table 3.6, and other material properties obtained from literature sources [12, 16, 25], the behavior of the NiTi as well as the sensing and variable stiffness properties of the UAM NiTi/Al composites were modeled. Models were created under two assumptions: first, the NiTi wires behave as 1-D elements, experiencing stress and strain along the axial direction, and second, there is no relative motion at the interface between the embedded NiTi wires and UAM matrix.

Sample	Bonded Area Ratio
1-1 Sample Fracture Surfaces	
1	59%
2	66%
3	68%
4	66%
3-2 Sample Fracture Surfaces	
1	67%
2	63%
3	66%
4	66%
5	67%
6	64%
7	67%
Average	66%
Standard Deviation	1.4%
C_v	2.1%

Table 3.5: UAM bond area as determined by fracture surface analysis.

Property	Value	Description
M_f	55 °C	Martensitic finish temperature
M_s	90 °C	Martensitic start temperature
A_s	65 °C	Austenitic start temperature
A_f	100 °C	Austenitic finish temperature
C_A	435 psi/ °C	Austenitic stress influence coefficient on austenite transition temperatures
C_M	145,000 psi/ °C	Estimated martensitic stress influence coefficient on martensite transition temperatures
ρ_A	0.92 $\mu\Omega$-m	Austenite electrical resistivity
ρ_M	1.07 $\mu\Omega$-m	Martensite electrical resistivity

Table 3.6: Material properties of 90 °C Flexinol as derived from experiment.

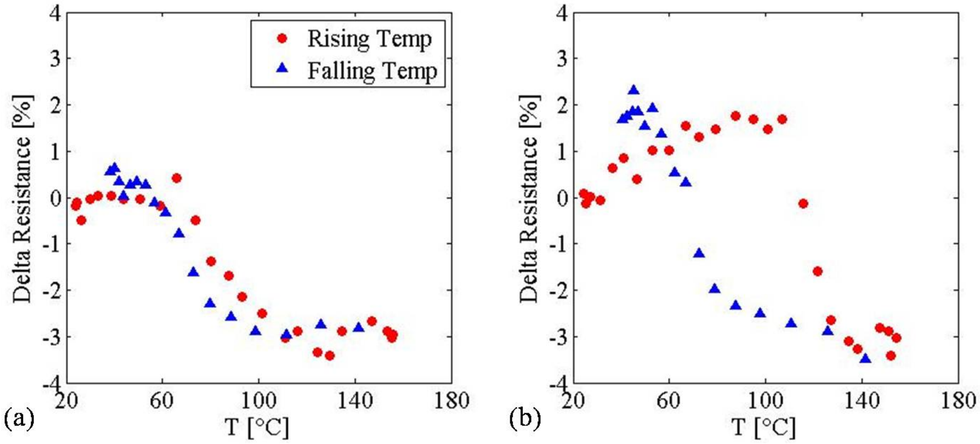

Figure 3.18: NiTi wire change in resistance versus temperature for (a) an unloaded wire and (b) a wire under a 2.7 lbs axial load.

NiTi Area Ratio	NiTi Phase	Average k [lbs/in]	Percent Stiffness Change
4.5%	Martensite	1.62×10^4	-6.0%
	Austenite	1.52×10^4	
13.4%	Martensite	6.28×10^3	5.5%
	Austenite	6.62×10^3	

Table 3.7: UAM active composite stiffness test results.

The Brinson constitutive model [2], 3.4, is used describe the thermo-mechanical behavior of the NiTi and define the volume fraction of its martensitic phase. The Brinson model calculates stress changes based upon elastic properties, 3.5, thermal properties, 3.6, and the thermo-mechanical coupling caused by transformation between austenite and both variants of martensite, 3.7. When the NiTi is fully martensitic or austenitic, the material properties for the corresponding phase are used. However if the material is subject to stress or temperatures that cause a phase transition, the value of the material properties used in the Brinson model are determined by the martensitic volume fraction. The Brinson model splits the volume fraction into two components, stress induced volume fraction, calculating the amount of detwinned martensite, and temperature induced volume fraction, shown in 3.8.

$$\Delta\sigma = E\left(\xi\right)\Delta\epsilon + \Theta\left(\xi\right)\Delta T + \Omega\left(\xi\right)\Delta\xi_s. \tag{3.4}$$

$$E\left(\xi\right) = \left(1-\xi\right)E_A + \xi E_M. \tag{3.5}$$

$$\Theta = E\left(\xi\right)\alpha. \tag{3.6}$$

$$\Omega = -E\left(\xi\right)\epsilon_L. \tag{3.7}$$

$$\xi = \xi_s + \xi_T. \tag{3.8}$$

In order to calculate volume fraction, the trend of temperature and applied stress must be known to determine which transformation, if any, the NiTi is experiencing. If a wire is initially martensitic and is subject to an increase in temperature and stress, the increasing temperature may cause an M-A transformation while the applied stress hinders the transformation by increasing the transformation temperatures. The volume fraction during the M-A transformation is defined by the Brinson model as seen in 3.9.

$$\xi\left(T,\sigma\right) = \frac{\xi_0}{2}\left[cos\left(a_A\left(T-A_s^\sigma\right)\right)+1\right], \tag{3.9}$$

where

$$a_A = \frac{\pi}{Af-As}. \tag{3.10}$$

In this case, the total volume fraction is decreasing with increasing temperature over the range of A_s^σ to A_f^σ due to phase transformation to austenite. The stress induced and temperature induced components of the volume fraction are given by 3.11 and 3.12, respectively.

$$\xi_s = \xi_{s0} - \frac{\xi_{s0}}{\xi_0}\left(\xi_0 - \xi\right) \tag{3.11}$$

$$\xi_T = \xi_{T0} - \frac{\xi_{T0}}{\xi_0}\left(\xi_0 - \xi\right) \tag{3.12}$$

If the NiTi is considered in an initially austenitic state and subject to stress, applied stress may cause an increase in ξ_s if the stress is between the critical stress levels, σ_s^{cr} and σ_f^{cr}. Detwinning of martensite begins at σ_s^{cr} and is considered complete at σ_f^{cr}. In an initially austenitic material, the critical stresses will mark the start and finish of the A-M stress induced transformation. Temperature affects the values of the critical stresses and, in addition to the magnitude of the applied stress, determines whether or not the NiTi will undergo the A-M transformation.

When $T > M_s$ and $\sigma_s^{cr} + C_M\left(T - M_s\right) < \sigma < \sigma_f^{cr} + C_M\left(T - M_s\right)$, the stress and temperature induced volume fraction are given by

$$\xi_s = \frac{1 - \xi_{s0}}{2} cos\left(\frac{\pi}{\sigma_s^{cr} - \sigma_f^{cr}}\left(\sigma - \sigma_f^{cr} - C_M\left(T - M_s\right)\right)\right) + \frac{1 + \xi_{s0}}{2} \tag{3.13}$$

and

$$\xi_T = \xi_{T0} - \frac{\xi_{T0}}{1 - \xi_{s0}}\left(\xi_s - \xi_{s0}\right). \tag{3.14}$$

When $T < M_s$ and $\sigma_s^{cr} < \sigma < \sigma_f^{cr}$, stress and temperature induce volume fractions are given by

$$\xi_s = \frac{1 - \xi_{s0}}{2} cos\left(\frac{\pi}{\sigma_s^{cr} - \sigma_f^{cr}}\left(\sigma - \sigma_f^{cr}\right)\right) + \frac{1 + \xi_{s0}}{2} \tag{3.15}$$

and

$$\xi_T = \xi_{T0} - \frac{\xi_{T0}}{1 - \xi_{s0}} \left(\xi - \xi_{s0}\right) + \Delta_{\xi_T}. \tag{3.16}$$

If $M_f < T < M_s$ and temperature is increasing, $\Delta_{\xi_T} = \frac{1-\xi_{T0}}{2} \left(cos \left(a_M \left(T - M_f\right)\right) + 1\right)$ where $a_M = \frac{\pi}{Ms-Mf}$. Otherwise, $\Delta_{\xi_T} = 0$.

3.3.2 NiTi Wire Modeling

The NiTi wire characterization experiment is modeled using both parameters obtained from the experiment, as seen in Table 3.6, and parameters obtained from literature, seen in Table 3.8. Once the volume fraction of the NiTi is determined as a function of stress and temperature, the strain of the wire is calculated by 3.17, the electrical resistivities of both phases are adjusted for temperature using their respective temperature coefficients [25], and the total NiTi resistance is calculated using the rule of mixtures and martensitic volume fraction [23] as seen in 3.18. Once resistivity is found, the total resistance of the NiTi wire is calculated by 3.19.

$$\epsilon\left(\xi, \sigma, T\right) = \frac{\sigma}{E\left(\xi\right)} - \epsilon_L \xi + \alpha_{NiTi}\left(T - T_0\right) \tag{3.17}$$

$$\rho_{NiTi}\left(\xi, T\right) = \xi\left[\rho_M + \kappa_M\left(T - T_0\right)\right] + \left(1 - \xi\right)\left[\rho_A + \kappa_A\left(T - A_f\right)\right] \tag{3.18}$$

$$R_{NiTi}\left(\xi, \sigma, T\right) = \frac{\rho_{NiTi}\left(\xi, T\right) L_0 \left(1 + \epsilon\left(\xi, \sigma, T\right)\right)}{A_{NiTi}} \tag{3.19}$$

where

$$A_{NiTi} = \frac{\pi d^2}{4}. \tag{3.20}$$

The model was used to replicate the results from the NiTi characterization experiment and can be seen in Figure 3.19. Change in resistance versus temperature was determined for a 0.015" diameter NiTi wire both under zero load and a 2.7 lbs (12 N)

Property	Value	Description
κ_A [25]	0.50 $n\Omega - m/°\text{C}$	Austenite resistivity temperature coefficient
κ_M [25]	1.75 $n\Omega - m/°\text{C}$	Martensite resistivity temperature coefficient
ϵ_L [12]	5%	NiTi recoverable strain
α_{NiTi} [23]	10.0×10^{-6} °C^{-1}	NiTi coefficient of thermal expansion
α_{Al} [16]	23.6×10^{-6} °C^{-1}	Al 6061 coefficient of thermal expansion
ρ_{Al} [16]	0.04 $\mu\Omega - m$	Al 6061 electrical resistivity
σ_s^{cr} [23]	20.3 ksi	Critical detwinning start stress
σ_f^{cr} [23]	24.7 ksi	Critical detwinning finish stress
E_A [12]	9720 ksi	Austenite elastic modulus
E_M [12]	3770 ksi	Martensite elastic modulus
E_{Al}(20 °C) [16]	9860 ksi	Al 6061 elastic modulus at 20 °C
E_{Al}(100 °C) [16]	9570 ksi	Al 6061 elastic modulus at 100 °C
E_{Al}(150 °C) [16]	9140 ksi	Al 6061 elastic modulus at 150 °C

Table 3.8: Additional material properties used for sensing and stiffness models.

axial load. The behavior of the wire resistance in response to temperature and stress is captured, showing a sharp change in resistance due to phase transformation of the wire as well as gradual increases in resistance before and after transformation due to the thermal coefficients of resistivity for each phase as well as thermal expansion of the wire. The model indicates a change in resistance of approximately 20% during transformation from martensite to austenite for both the loaded and unloaded cases. Relative to room temperature resistance, the model predicts an approximate -12% drop in resistance for the unloaded case and -11% for the 2.7 lbs axially loaded wire after completion of the M-A transofrmation.

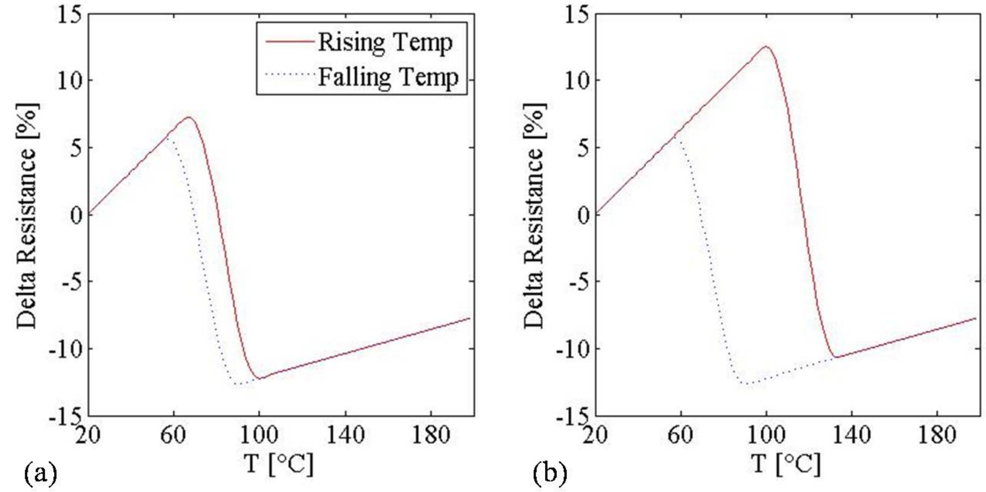

Figure 3.19: NiTi wire model change in resistance versus temperature for (a) 0 lbs axial load and (b) 2.7 lbs axial load.

3.3.3 Composite Sensing

A model for NiTi composite sensing capabilities was developed which uses the NiTi resistance equation discussed in section 3.3.2 to determine the resistance of the embedded NiTi wires. For modeling the composite matrix, the resistances of the aluminum regions are calculated through 3.21.

$$R_{Al}\left(T\right)=\frac{\rho_{Al}L\left(T\right)}{A_{Al}} \tag{3.21}$$

where

$$L\left(T\right)=\left(\alpha_{Al}\left(T-T_0\right)+1\right)L_0 \tag{3.22}$$

and

$$A_{Al}=w\times t-n\frac{\pi d^2}{4}, \tag{3.23}$$

where L_0 is original axial length, w is gauge width, t is gauge thickness, n is number of embedded wires, and d is diameter of embedded wires.

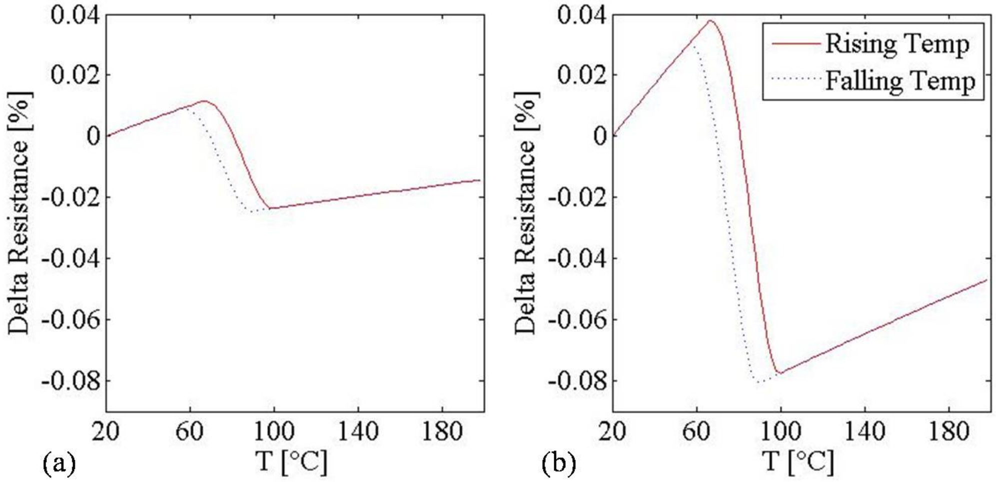

Figure 3.20: NiTi/Al UAM composite sensing model for (a) 4.5% NiTi area ratio and (b) 13.4% NiTi area ratio.

The total composite resistance is then calculated as a parallel resistor pair, 3.24, whereas the change in resistance is calculated by 3.25.

$$R_{comp}\left(\xi,\sigma,T\right)=\left[\frac{1}{R_{Al}\left(T\right)}+\frac{1}{R_{NiTi}\left(\xi,\sigma,T\right)}\right]^{-1}. \tag{3.24}$$

$$\Delta R_{comp}\left(\xi,\sigma,T\right)\%=\frac{R_{comp}\left(\xi,\sigma,T\right)-R_{comp}\left(1,\sigma,20\,^{\circ}\mathrm{C}\right)}{R_{comp}\left(1,\sigma,20\,^{\circ}\mathrm{C}\right)}. \tag{3.25}$$

The composite model was used to calculate the expected change in resistance of both UAM composites at zero applied load. As seen in the model output, Figure 3.20, the 4.5% composite is expected to have a change in resistance of approximately 0.03% while the 13.4% composite is expected to have an approximate 0.08% change in resistance when the embedded NiTi transforms from martensite to austenite.

3.3.4 Composite Stiffness

For long fiber reinforced matrices, stiffness is calculated as a rule of mixtures [3] as seen below:

$$k_{comp}\left(\xi, T\right) = \frac{E_{NiTi}\left(\xi\right) A_{NiTi} + E_{Al}\left(T\right) A_{Al}}{L}. \tag{3.26}$$

To calculate composite stiffness as a function of temperature and stress, the elastic moduli for Al 6061 and the embedded NiTi wires are first determined. The elastic modulus of Al 6061 is linearly interpolated over two temperature ranges temperature using modulus values at 20 °C, 100 °C, and 150 °C, seen in Table 3.8. The elastic modulus of NiTi is calculated as seen in 3.5.

The maximum percent change in stiffness is calculated by finding the difference in composite stiffness when the embedded NiTi is fully austenitic and when it is fully martensitic at room temperature, and then normalizing the difference by the martensitic composite stiffness at room temperature:

$$\Delta k_{comp}\left(\xi, T\right)\% = \frac{k_{comp}\left(\xi, T\right) - k_{comp}\left(1, 20\,^{\circ}\mathrm{C}\right)}{k_{comp}\left(1, 20\,^{\circ}\mathrm{C}\right)}. \tag{3.27}$$

The model results for expected stiffness change are shown in Figure 3.21 The model shows that the 4.5% NiTi composite exhibits an approximate 2% increase in stiffness during the M-A transition, however the softening of the surrounding Al matrix prevents and net increase in stiffness relative to room temperature. The 13.4% NiTi composite model shows an aproximate 7% increase in stiffness associated with the M-A transition of NiTi, resulting in a 5% increase over room temperature stiffness.

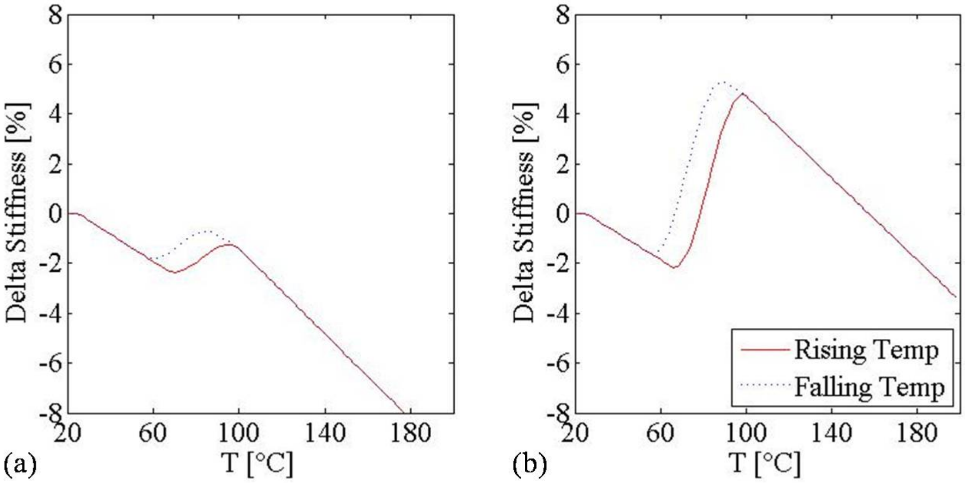

Figure 3.21: NiTi/Al UAM composite stiffness model for (a) 4.5% NiTi area ratio and (b) 13.4% NiTi area ratio.

3.4 Discussion of Results

3.4.1 UAM Composite Characterization

3.4.1.1 Al 3003H-18 Matrix

3.4.1.1.1 Shear (1-1) Testing All 1-1 UAM sample tests consisted of a predominantly linear force/displacement relationship. This indicates that samples failed in a brittle fracture mode. There is considerable deviation in the values of reported ultimate shear strength. Table 3.2 shows an average value of 7.64 ksi with a standard deviation of 1.27 ksi. With a coefficient of variance of 16.6%, the ultimate shear strength of the 1-1 UAM samples is found to be very inconsistent. The average ultimate shear strength value is also significantly lower than expected, only 47.8% of that of the solid parent material, as shown in Table 3.10.

It is possible that the low strength and deviation in strength are both due to non-optimal welding parameters. In ultrasonic welding of aluminum tapes, it has been

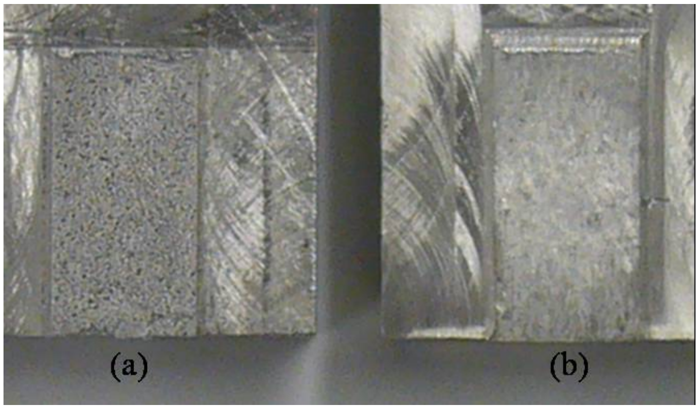

Figure 3.22: Failure surfaces of (a) UAM 1-1 sample and (b) solid Al 3003-H14 sample.

indicated that the welds can be stronger under a peel load than the bulk material when welded under the optimal parameters [20], however such results were obtained with two-tape, single weld samples. With the samples tested for this research, additional welding taking place on subsequent layers may degrade the performance of previously welded layers.

All 1-1 samples share a unique fracture surface pattern. This static-like pattern is due to the textured horn plastically deforming the tape as it is being welded. One result of this heavily textured surface is that the interface of two tapes has regions of intimate contact as well as regions of no contact during the welding process. This results in a bond that, while apparently solid on the outside, has many small voids dispersed throughout the bond area. A comparison of a UAM fracture surface to a solid aluminum sheared surface is shown in Figure 3.22. More consequences of imprinted horn texture will be further discussed in section 3.4.1.1.4.

3.4.1.1.2 Transverse Tensile (3-2) Testing All 3-2 UAM samples tests indicate a strongly linear force/displacement relationship, again indicating a brittle fracture failure. The average ultimate tensile strength of 3-2 UAM samples was found to be 4.34 ksi, approximately 15.0% of the tensile strength of solid Al 3003 H-18, as seen in Table 3.10. Standard deviation for ultimate tensile strength was found to be 410 psi. With a coefficient of variance of 9.45%, the ultimate tensile strength for 3-2 samples is more consistent than ultimate shear strength, although UAM 3-2 samples were weaker that 1-1 samples when compared to their respective solid Al 3003-H18 strengths.

The fractured interfaces of most 3-2 UAM samples look similar to the faces seen in 1-1 UAM specimens. However, the fracture surface of 3-2 sample 6 has a mill-pass pattern as seen in Figure 3.23. This is due to a procedure in the UAM process called a "flat pass." When creating a build by welding successive layers of tapes on top of each other, the integrated CNC head is programmed to mill the entire surface of the build every 0.250" of build height to remove any height discrepancies in the aluminum matrix. Height variations may occur if, for instance, matrix material is displaced by embedded materials. The flat pass ensures a level surface on which the subsequent layers can be welded. The interface of a flat pass can be easily distinguished because the distinctive horn pattern imprinted on every tape is milled off during the flat pass.

The flat pass layer in UAM 3-2 sample 6 was not a feature unique to this sample; all samples were made from the same UAM bulk build and therefore have a flat pass interface at the same build height. Since none of the other samples failed at the flat pass interface, and in fact failed at a significantly higher level in the gauge region, it

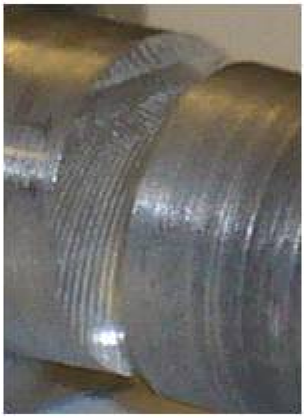

Figure 3.23: UAM 3-2 sample 6 showing an atypical fracture surface pattern.

is assumed that a process anomaly occurred in the build region from which sample 6 was made. 3-2 sample 6 is not believed to be representative of a typical UAM material and is therefore deemed an outlier and not included in any statistical analyses.

UAM 3-2 sample 3 is also not considered in any statistical analyses. This is due to the fact that there was a specimen loading error prior to testing of sample 3. The grips separated partially as load was applied allowing the sample to slip during testing and possibly subjecting it to an off-center loading. Since the loading scheme was not identical to other samples, 3-2 sample 3 is also considered an outlier.

Most 3-2 UAM samples failed close to the top grips. A comparison of the fracture locations can be seen in Figure 3.24. Heights of fractured samples were measured and shown in Table 3.9. As seen in the table, samples fractured an average of 0.198” from the top of each sample. Assuming a tape thickness of 0.006”, this indicated that all considered samples failed within a region near the 33rd tape layer from the top of the sample. It is also noted that 3-2 sample 6 did not fail in the same region but failed 0.305” from the top surface.

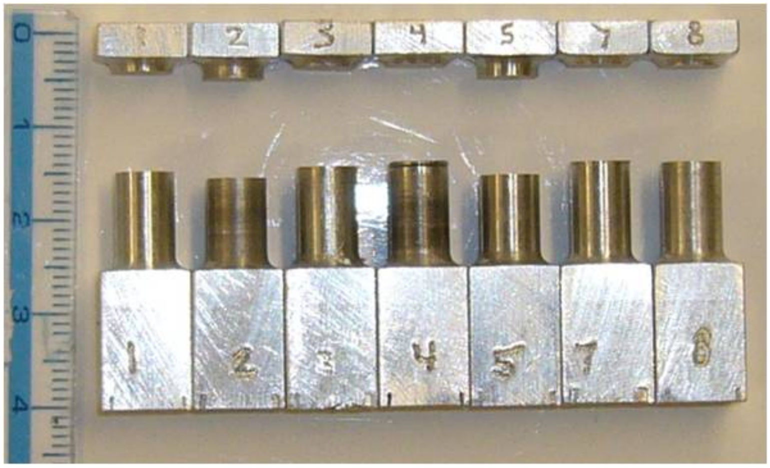

Figure 3.24: UAM 3-2 samples showing similar failure locations.

Sample	Distance from Top [in]
1	0.197
2	0.226
3	0.184
4	0.177
5	0.226
6	0.305
7	0.177
8	0.184
Average	0.198
Standard Deviation	0.023
C_v	12%

Table 3.9: Distance of failure surface from top, samples 3 and 6 not statistically considered.

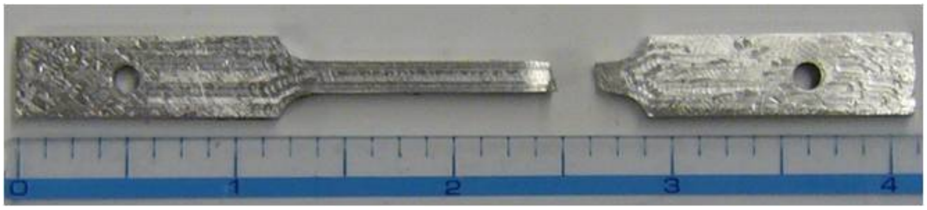

Figure 3.25: UAM 1-2 sample failure showing necking at gauge length.

This observation indicates that local mechanical properties, including ultimate tensile strength, vary with build height. An explanation for the degradation in bond strength with respect to build height is the decreased bending stiffness of the build as it becomes taller. The transverse ultrasonic oscillations will cause the build to vibrate at larger amplitudes as it is built higher, thus decreasing the effective ultrasonic amplitude at the current weld interface. Since vibration amplitude is one of the main process parameters for UAM, this reduced amplitude will likely cause a gradient of mechanical property values as a function of build height.

Similar to UAM 1-1 fracture surfaces, all 3-2 samples share a unique fracture surface pattern due to the deformation induced by the UAM horn. Both 3-2 and 1-1 fracture surfaces are analyzed and discussed in section 3.4.1.1.4.

3.4.1.1.3 Longitudinal Tensile (1-2) Testing Unlike the other UAM samples, the 1-2 samples exhibited a substantial plastic yielding region after the linear elastic region, as seen in Figure 3.15. This is typical of aluminum alloys and also indicates that failure of UAM material in the 1-2 direction occurs in a ductile mode. Further evidence of ductile failure is seen in Figure 3.25, which shows necking near the failure region in a UAM 1-2 sample.

Strength	Al 3003-H18 [ksi] [22]	UAM [ksi]	% Solid Strength
Ultimate shear (1-1 mode)	16	7.64	47.8
Ultimate tensile (3-2 mode)	29	4.34	15.0
Ultimate tensile (1-2 mode)		34.2	117.9

Table 3.10: Comparison of Al 3003-H18 UAM matrix and solid Al 3003-H18 strength.

All tested 1-2 samples exhibited a higher than expected tensile strength. Al 3003-H18 has a tensile strength of 29 ksi [22]. The average ultimate tensile strength of 1-2 UAM samples is 34.2 ksi, a 17.9% increase over the solid parent material as seen in Table 3.10. This is a departure from both the 1-1 samples and 3-2 UAM samples previously tested in which the obtained ultimate stresses were significantly lower than the parent material. The results for the longitudinal samples were also more consistent than those for other UAM samples with a coefficient of variance of 2.46%. These results suggest a strong directionality in the strength of UAM materials.

The ultimate tensile strength of 1-2 UAM samples does not exhibit the reduced strength when compared to the base material because unlike the 1-1 and 3-2 UAM specimens, the stress is transmitted almost entirely through the solid tapes that make up the build rather than through the intermittently bonded regions. Furthermore, the observed increase in tensile strength over the parent material is believed to be due to grain refinement of the aluminum tapes as a result of the UAM process. The UAM sonotrode has a texture which helps to transfer ultrasonic vibrations to the weld interface. The combination of mechanical deformations caused by sonotrode texture as well as the ultrasonic vibrations is thought to cause grain refinement in the Al tapes [15]. Through the Hall-Petch relationship, as grain size of a material decreases, hardness and strength increase.

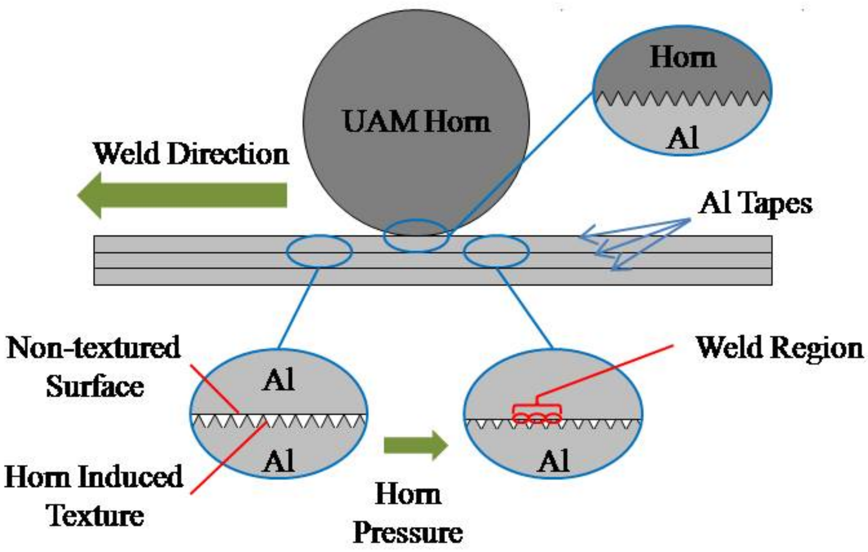
Horn
Al
UAM Horn
Weld Direction
Al Tapes
Non-textured Surface
Al
Al
Horn Induced Texture
Horn Pressure
Weld Region
Al

Figure 3.26: The UAM horn textures the top surface of each tape leaving the bottom surface to be deformed through plastic deformation due to discrete contact with the mating tape below. This intimate contact leads to bonding.

3.4.1.1.4 UAM Bond Characterization When analyzing UAM fracture surfaces, only the top surfaces of the interfaces were used. This is because the bottom surface of an interface has been fully textured by the horn where the top surface is only textured where there was intimate contact and subsequent bonding to the mating tape. This is illustrated in Figure 3.26. The resulting top surface has a visual contrast between the unbonded regions, which appear smooth except for striations made during the tape manufacturing process, and the bonded regions which have been plastically deformed due to bonding and separation from mating tapes.

Most UAM 1-1 and 3-2 fracture surfaces looked similar to those seen in Figure 3.16. Dark areas under lower magnification are the previously bonded regions, while

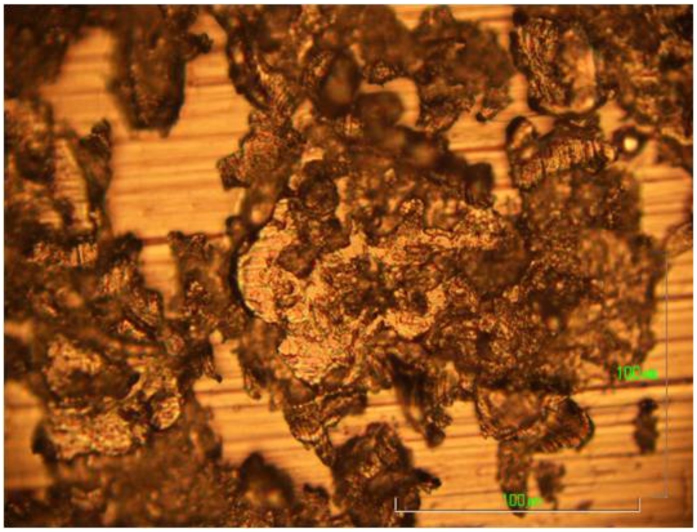

Figure 3.27: UAM 3-2 sample fracture surface showing plastic deformation and mill striations.

the lighter colored areas are unbonded regions. Under higher magnification, Figure 3.27, the plastic deformation of the dark regions is clearly seen.

All 1-1 and 3-2 sample fracture surface micrographs are images of the bottom, non-horn side, of the tape. In contrast, Figure 3.28 is a micrograph of UAM 1-1 sample 1 from the top, or horn side, of the tape. The figure shows a much more deformed surface and no visible oriented striations from the tape manufacturing process.

With this observation, it is apparent that the bond area ratio is most easily determined by observing the non-horn side of the fracture surface as there is stark contrast between the mill finish of the unbonded areas and the true fracture surface of the bonded regions. The average bond area ratio of all non-horn side micrographs is 66%, as shown in Table 3.5.

The percent bond area of a sample could be used to determining the quality of bonds produced by a specific set of UAM parameters. As the bond area ratio

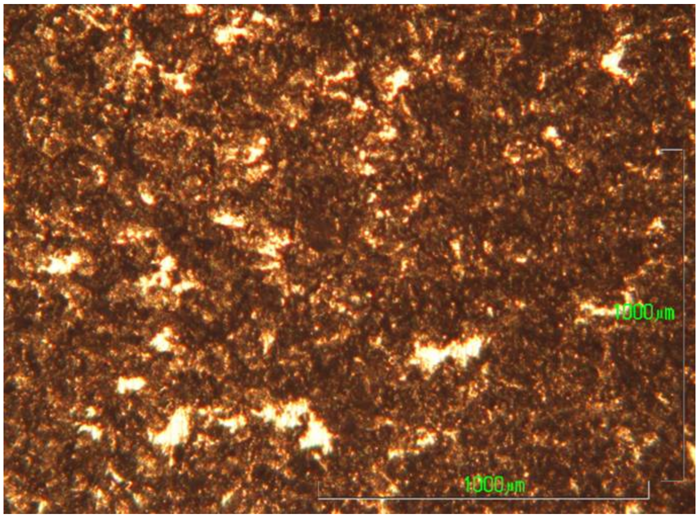

Figure 3.28: Bottom fracture surface of UAM 1-1 sample 1 showing nearly complete surface deformation due to contact with the horn.

increases, the strength of the bonds is expected to increase as well. With a coefficient of variance of 2.1%, this is a more consistent measurement of UAM bond than both transverse tensile strength and shear strength.

From the optical micrographs of UAM fracture surfaces, it is apparent that all UAM samples have voids along weld interfaces. The embedded voids can be considered as embedded cracks creating stress concentrations and causing premature failure of UAM samples. The samples most affected by the embedded voids are the 1-1 and 3-2 UAM samples. The voids in 1-1 samples cause a mode II fracture while the 3-2 samples cause a mode I fracture. The orientation of the voids and corresponding fracture modes are shown in Figure 3.29 (a) and (b) for 3-2 and 1-1 specimens, respectively. The low shear and tensile strengths of 1-1 and 3-2 UAM samples is explained by considering the stress concentration factors produced by the embedded voids. In

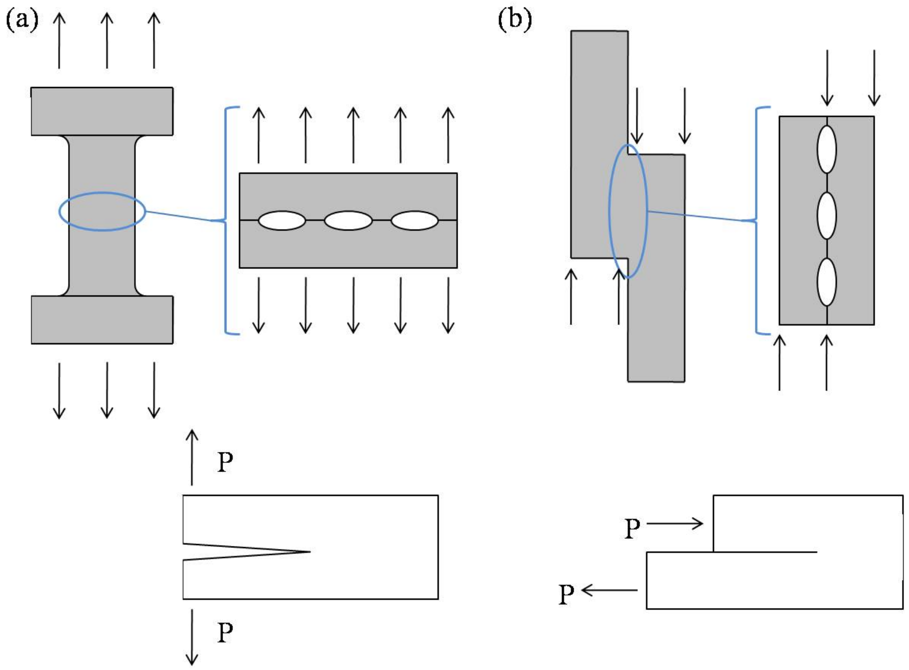

Figure 3.29: Voids in UAM samples are fracture initiation sites resulting in (a) mode I fracture in 3-2 samples and (b) mode II fracture in 1-1 samples.

contrast, the 1-2 samples have the voids along the same plane as the axial load. In this orientation the voids have little effect on the strength of the sample.

3.4.2 UAM Composite Modeling

3.4.2.1 NiTi Wire

As shown in Figure 3.19, the NiTi wire resistance model describes the overall shape of the experimental data. The model shows three distinct regions: an initially linear increase in resistance change with increasing temperature followed by a sharp drop in resistance change as the temperature increases through the transition region and a second linear region after transformation is complete. The regions are repeated in reverse upon cooling with a shift in the transition region due to the difference between the martensitic start and finish temperatures and austenitic start and finish temperatures. The first linear region shows that resistance is dominated by thermal expansion of the wire. The sharp change in resistance in the transition region is driven the transformation from martensite to austenite and subsequent large change in wire resistivity. The second linear region shows that after transformation, resistance is again dominated by thermal expansion of the wire.

While the shape of the wire response is captured by the model, the magnitude of resistance change during transformation shows an approximate -20% change as opposed to the -4% change observed in the experiment. This discrepancy may be due to the combination of material properties as determined by the NiTi characterization experiment and material properties obtained from literature sources. In order to correct the model, more experiments are required to find material properties specific to the NiTi alloy used in the UAM composites.

3.4.2.2 Composite Sensing

The NiTi resistance model was incorporated into the NiTi/Al composite model which gives the calculated composite resistance change as a function of temperature, as seen in Figure 3.20. The composite sensing model indicates that an approximate -0.04% change in resistance is expected for the 4.5% NiTi area ratio composite while the 13.4% NiTi area ratio composite is expected to experience a -0.12% change in resistance during the M-A transformation with no axial load. The sensing model shows three distinct regions similar to the NiTi wire model.

Since the NiTi wire model shows significantly more resistance change than demonstrated in the wire experiment, it is assumed that the composite sensing model also overestimates the change in resistance of the UAM composites. The model does show, however, that the resistance change is highly dependent upon the amount of NiTi embedded within the composite. This indicates that by increasing the amount of embedded wire, the sensing capabilities of the composite can be increased as well.

3.4.2.3 Composite Stiffness

The results from composite stiffness testing experiments are shown in Table 3.7. As predicted by the model, the 4.5% area ratio build experiences a decrease in stiffness after the M-A transition of the embedded wire. The 13.4% area ratio composite also correlates with the increase in stiffness predicted by the model. The 4.5% NiTi area ratio composite experiences a 6% reduction in stiffness while the 13.4% NiTi area ratio composite exhibits a 5.5% increase in stiffness.

The model results for expected stiffness change are shown in Figure 3.21. The modeling of the two different composites shows that the 4.5% area ratio build does not have a sufficient NiTi area ratio to overcome the softening of aluminum with increasing temperature. This results in a net softening of the composite soon after the completion M-A transition. The 13.4% area ratio composite is able to offset softening of the Al matrix through stiffening associated with the M-A transition of NiTi. Though the model predicts, and experiments show, that only the 13.4% NiTi area ratio composite will experience an increase over room temperature stiffness, both composites are expected to be stiffer than a solid aluminum piece of the same dimensions once the NiTi transformation begins, as seen in Figure 3.30.

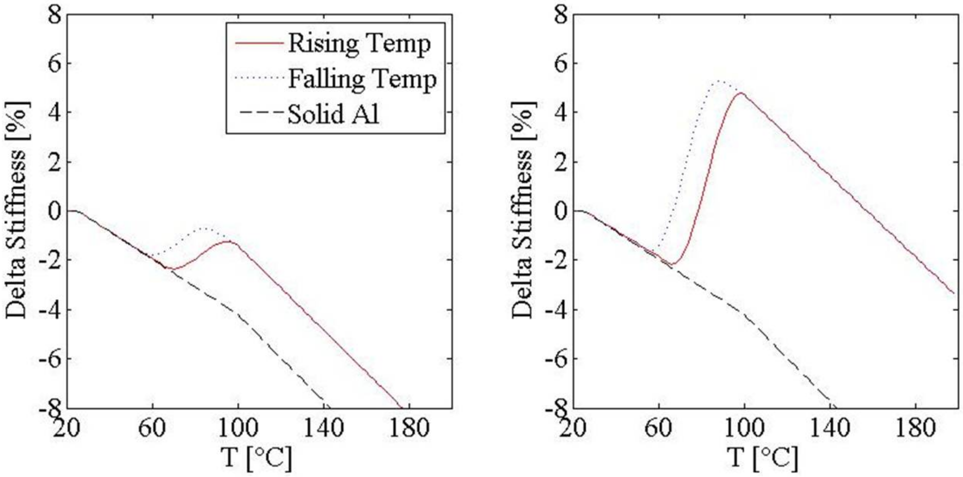

Figure 3.30: Solid Al 6061 stiffness model compared to calculated stiffness of NiTi/Al UAM (a) 4.5% NiTi area ratio composite and (b) 13.4% NiTi area ratio composite.

3.4.2.4 Composite Model Assumptions

The resistance and stiffness changes in the UAM composites were initially thought to occur from the temperature induced transformation of the embedded NiTi. However, if the assumptions made in modeling the composites are true, 1-D behavior of the NiTi wire and a perfect mechanical coupling of the wire and matrix (i.e., no relative motion) this would not allow for temperature induced phase change of the detwinned NiTi. As the Al matrix undergoes thermal expansion, additional stress would be placed on the NiTi wire, raising the transformation temperatures as stress increases. Furthermore, since the wire was embedded in the detwinned state, a transformation to austenite would require the Al matrix to undergo the same strain as the NiTi wire, approximately -5%. Straining the Al matrix by such an amount would create significant stress on both the matrix and embedded wires if they were perfectly coupled, further elevating the transition temperatures and plastically deforming the matrix.

The composite stiffness experiments show that there is a change in composite stiffness as a function of temperature, though the composite does not undergo a large amount of strain. One explanation for the observed effect is that the first assumption does not hold: the wire may be completing its phase transition by straining in a direction other than the axial direction. This would invalidate the 1-D wire assumption but would allow for the M-A transition and associated property changes.

A second explanation assumes that the assumption of perfect coupling is invalid. If the wire is allowed to transform to austenite and contract within the matrix, a full phase transition would be possible. Previous work in embedding NiTi SMA using UAM has shown that if the wire is embedded while it is in its austenite phase, stress induced martensite produces not only a axial strain, but a radial contraction that disengages the wire from the matrix [21]. With the radial strain in mind, as the wire embedded in the UAM composites is heated and transforms to austenite, the diameter will expand as the axial length contracts. This radial expansion may create enough contact between the wires and matrix to allow for improved mechanical coupling when the wire is in its austenitic phase. This improved couping would allow the NiTi wire to help support the axial load and create an increase in the stiffness of the composite. This hypothesis both allows the recovery of detwinning strain and increased stiffness after transformation.

An alternative explanation allows for perfect mechanical coupling but restricts the transformation of the wire. As the composite is heated, the different coefficients of thermal expansion of the NiTi and Al matrix create and internal stress in the composite. This results in compressive stresses in the matrix while putting the embedded wires in tension, elevating the transformation temperatures. Though the wires do not transform in this explanation, as temperature increases, the stress on the wires increases as they attempt to transform. This creates internal compressive stresses acting on the composite matrix, counteracting the externally applied stresses and reducing overall deflection, thus creating a decrease in stiffness as a function of temperature.

CHAPTER 4

CONCLUSIONS AND FUTURE WORK

This research has focused on developing and characterizing methods for joining NiTi to common structural alloys and creating NiTi/Al composites. Additional effort was given to characterizing the NiTi/Al composites in terms of their strain sensing and stiffness tuning capabilities. Laser and TIG welding, fusion based processes, were investigated for joining NiTi to 304 SS while USS was used to investigate joining NiTi to Al 2024 and O1 tool steel in addition to 304 SS. A new manufacturing process, UAM, was also investigated as a method to create metal matrix composites by embedding NiTi in an Al 6061 matrix. The following sections summarize the conclusions and future work of each of the investigated processes.

4.1 Laser Welding

Laser welding has proven to be a successful method of joining NiTi and 304 SS. Through this research, the use of Ni filler to create viable fusion joints between NiTi and ferrous materials has been expanded. Cracking is still an issue with laser tube welding, however, with more precise work pieces and adjustment of laser parameters as well as varying the amount of Ni filler, an optimal set of process parameters can be found that will consistently create crack-free joints.

Once viable welds are created, process parameters can be further studied by testing the strength of the joints. Torsional and tensile joint strength are key evaluation criteria for a given NiTi laser weld tubular joint. The next step in characterizing the laser welds is quantifying and modeling the effect of the joining process on the thermo-mechanical behavior of the joined NiTi. The effect of the joining process on the NiTi is dependent upon the size of the HAZ. While preliminary optical characterization of the HAZ was performed, microhardness maps of sample sections will give a more accurate description of the extent of the HAZ.

Also, in addition to laser parameters and the amount of Ni filler, the effect of Post Weld Heat Treatment (PWHT) should be investigated as a possible method of regaining cold work lost through the joining process. The effect of PWHT on joint strength also requires additional research.

4.2 Tungsten Inert Gas Welding

Though this research failed to provide a viable TIG weld between NiTi and 304 SS, this process should not be abandoned. Analysis of the failed joints can be performed to observe what intermetallics formed and where failure originated. Using this information, a new joint design could be used to create a viable TIG weld. Other methods, such as Ni plating on the 304 SS pieces, Ta, or V interlayers should also be investigated as ways of creating NiTi/304 SS TIG joints.

Once viable joints are created, characterization similar to that planed for laser welds should be done including strength testing, HAZ characterization, and thermo-mechanical characterization of the NiTi. The ubiquity of TIG welding combined with a reliable way to fusion weld large pieces of NiTi to ferrous materials could allow for widespread use of NiTi in many areas of design and manufacturing.

4.3 Ultrasonic Soldering

The lap shear tests have indicated that USS is best suited to joining NiTi to Al 2024. This material pair had the highest ultimate shear strength of all NiTi containing joints and the lowest coefficient of variance indicating that it is the most repeatable joint to create. In addition, USS can be used to create consistent joints between NiTi and itself. For all USS joints, proper surface preparation is paramount in creating strong, consistent bonds.

The results from lap shear testing were adapted to create a purpose designed joint for NiTi tubes. More torsion testing is required to refine the manufacturing process and create a more consistent tubular solder joint. In addition to more torsional strength testing, system testing needs to be performed to determine if the joint is able to withstand the stresses and additional heat associated with shape memory based actuation of the attached NiTi tube. A more robust joint may also be possible by having a purpose built soldering tip specifically designed to cause cavitation on concave surfaces, such as the torsion saddles.

Additional modeling is also required to estimate the stresses in the solder joints due to differential thermal expansion of the NiTi and structural materials. Also, current joints can be further analyzed to observe what types of compounds form as the result of alloying between the base metal and solder.

4.4 Ultrasonic Additive Manufacturing

4.4.1 Matrix Characterization

The mechanical testing of the UAM matrix has well characterized the anisotropic nature of the material's strength. Also, presence of voids dispersed throughout the bond region has given a new perspective on failure of UAM parts. By reducing the voids in the bond regions, the strength of the UAM matrix is predicted to increase both due to increased bonding area and a reduction in stress concentration points.

The strength testing performed only predicts the strength of a matrix of the Al 3003-H18 made with the same process parameters. A fundamental understanding of how each parameter affects the resulting matrix has yet to be achieved. A parametric study of the UAM process is required to obtain the best bond possible. Such a study would be required for each new material used in constructing UAM matrices.

4.4.2 Active Composites

UAM was successfully used to embed 0.008" diameter wires, an increase of 100% of previously embedded fibers. This was made possible through use of the 10 kW UAM test bed system at EWI. With the increased power it may be possible to embed larger diameter wires or foils in a metal matrix.

By embedding the NiTi wires, active composites were created which were able to produce a 6.0% increase in stiffness by increasing composite temperature. The stiffness of the composite was modeled using the Brinson constitutive model for 1-D SMAs to determine the phase and subsequent mechanical properties of the embedded NiTi wire.

Modeling indicates that the same composite can be used for strain sensing allowing for a composite that can be structural in addition to acting as a sensor and actuator. Models of the active composite suggest that by adding more NiTi, the stiffness change of the composite can be significantly increased. Future work will focus on creating composites with higher NiTi area ratios as well as embedding twinned martensitic and austenitic NiTi. Additional testing and modeling will be performed to characterize both stiffness change and sensing capability of the next generation of NiTi/Al UAM composites.

While the models have closely represented the stiffness of the NiTi/Al UAM composites, more investigation is required to determine the nature of the NiTi/Al interface as well how the NiTi is affected by the UAM process. Both issues can be studied through a combination of microscopic analysis as well as macroscopic mechanical tests. In addition to the NiTi/Al interface, the active composite models can be more finely honed by further experimental characterization of the NiTi alloy used to create the NiTi/Al matrices.

APPENDIX A

FIXTURE, SAMPLE, AND TESTING JIG DRAWINGS

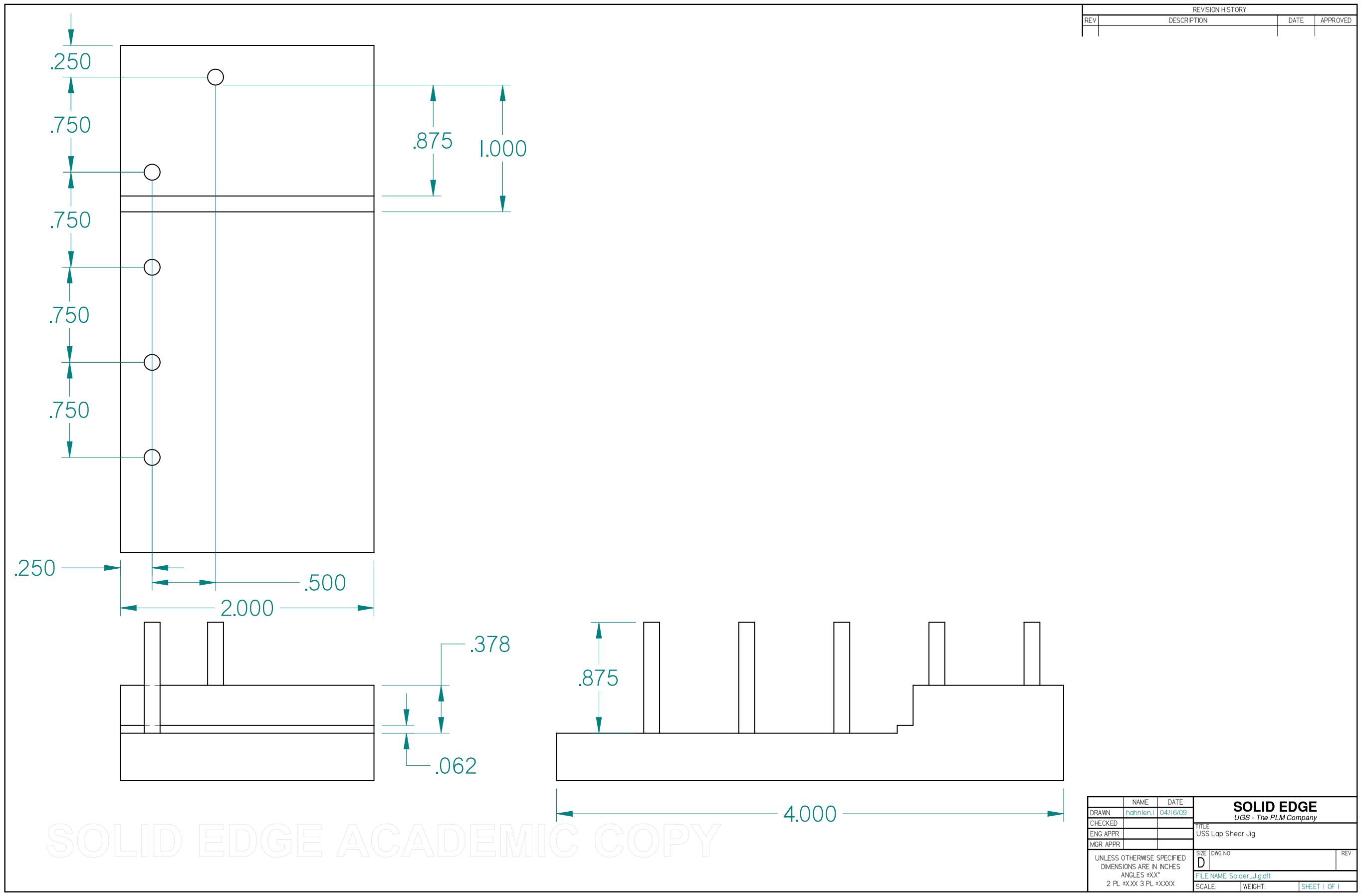
REVISION HISTORY
REV
DESCRIPTION
DATE
APPROVED
.250
.750
.750
.750
.750
.875
1.000
.250
.500
2.000
.378
.062
.875
4.000
SOLID EDGE ACADEMIC COPY
NAME
DATE
DRAWN
hahnlen.l
04/16/09
CHECKED
ENG APPR
MGR APPR
UNLESS OTHERWISE SPECIFIED
DIMENSIONS ARE IN INCHES
ANGLES ±X.X°
2 PL ±X.XX 3 PL ±X.XXX
SOLID EDGE
UGS - The PLM Company
TITLE
USS Lap Shear Jig
SIZE
D
DWG NO
REV
FILE NAME: Solder_Jig.dft
SCALE:
WEIGHT:
SHEET 1 OF 1

Figure A.1: Ultrasonic soldering fixture used to create consistent USS joints with a nominal thickness of 0.003”. All dimensions in inches.

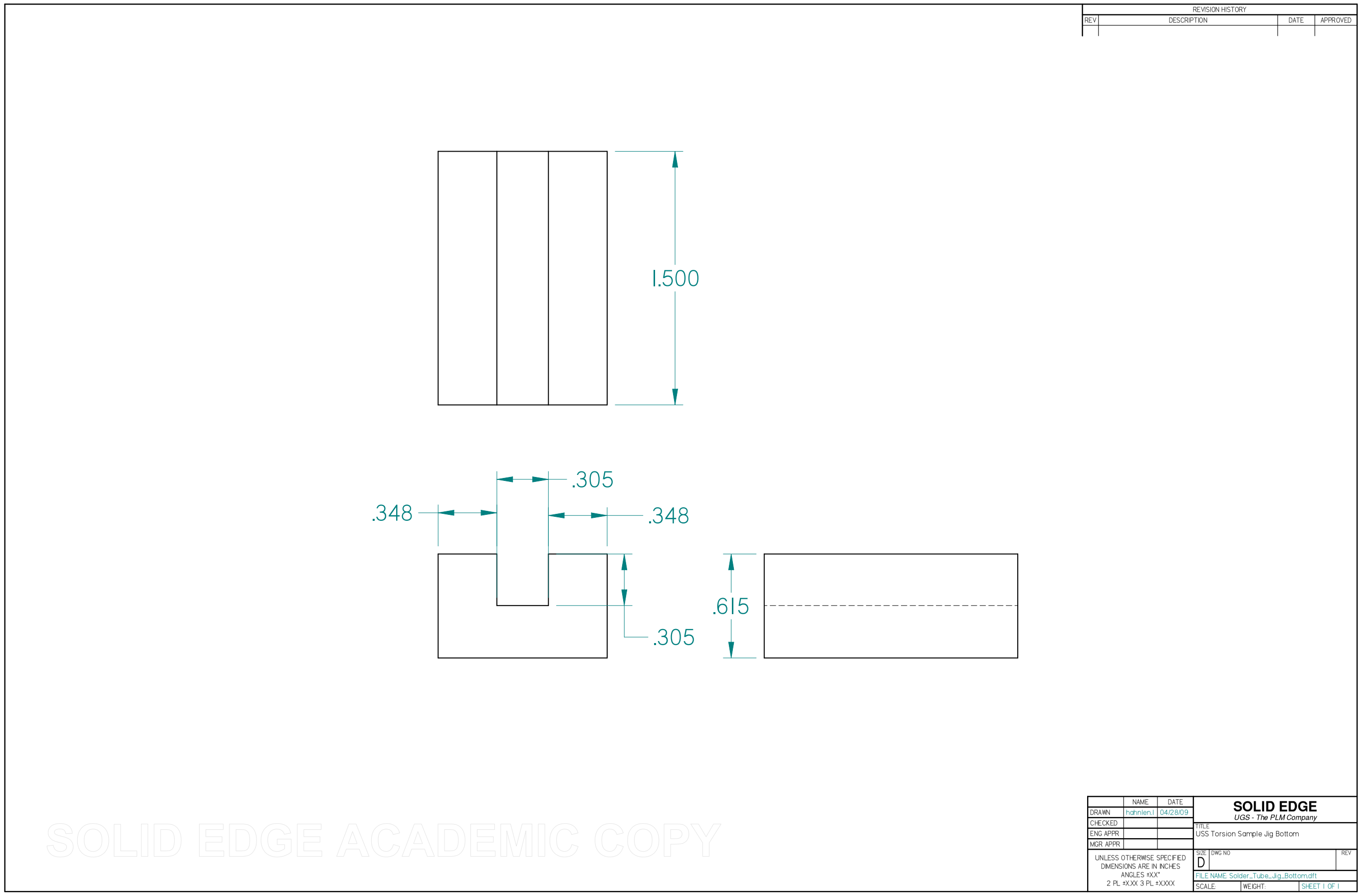
REVISION HISTORY
REV
DESCRIPTION
DATE
APPROVED
1.500
.305
.348
.348
.305
.615
SOLID EDGE ACADEMIC COPY
NAME
DATE
DRAWN
hahnlen.l
04/28/09
CHECKED
ENG APPR
MGR APPR
UNLESS OTHERWISE SPECIFIED
DIMENSIONS ARE IN INCHES
ANGLES ±X.X°
2 PL ±X.XX 3 PL ±X.XXX
SOLID EDGE
UGS - The PLM Company
TITLE
USS Torsion Sample Jig Bottom
SIZE
D
DWG NO
REV
FILE NAME: Solder_Tube_Jig_Bottom.dft
SCALE:
WEIGHT:
SHEET 1 OF 1

Figure A.2: Bottom half of USS torsion sample cooling fixture. All dimensions in inches.

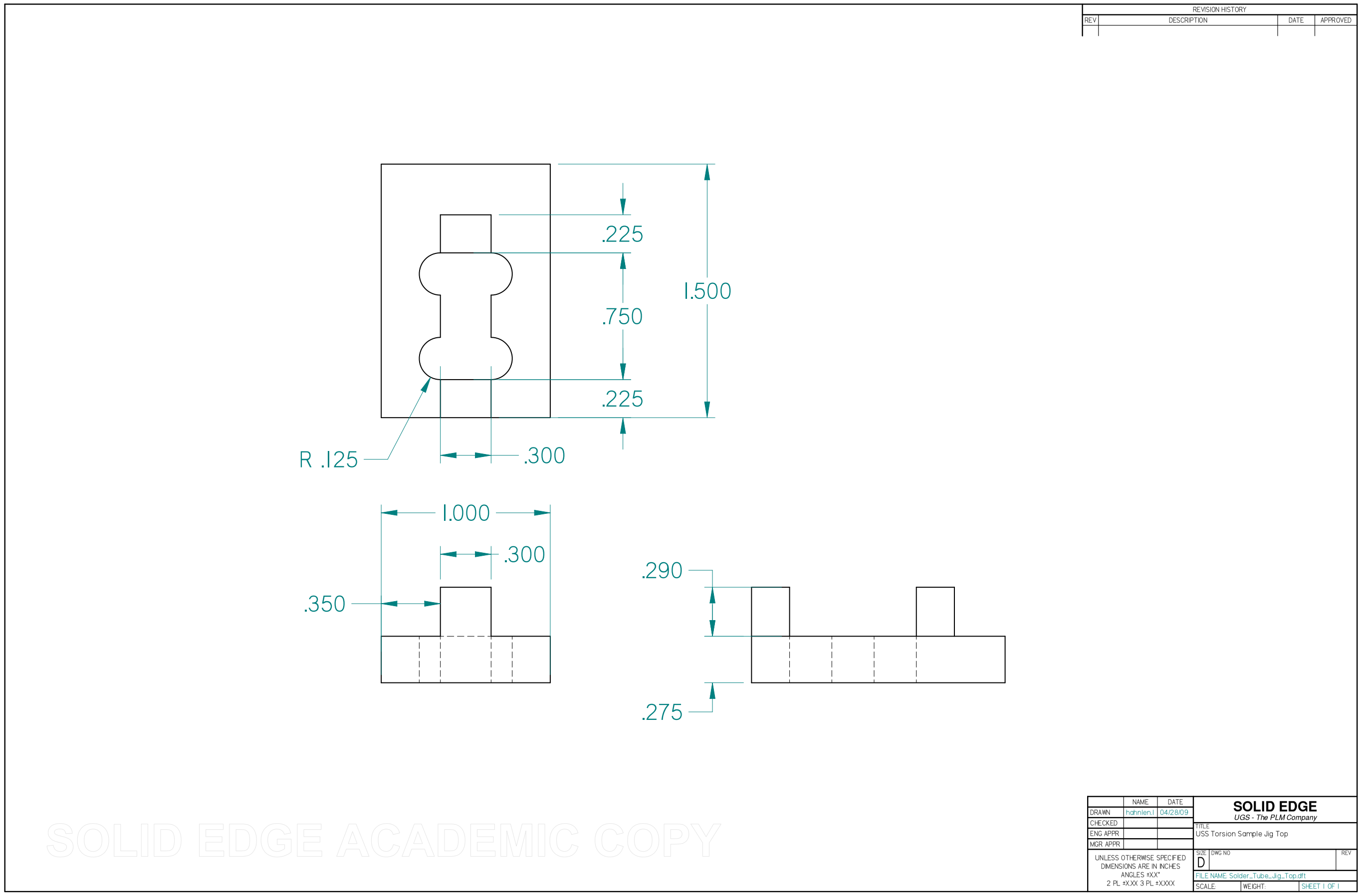
REVISION HISTORY
REV
DESCRIPTION
DATE
APPROVED
.225
.750
.225
1.500
R .125
.300
1.000
.300
.350
.290
.275
SOLID EDGE ACADEMIC COPY
NAME
DATE
DRAWN
hahnlen.l
04/28/09
CHECKED
ENG APPR
MGR APPR
UNLESS OTHERWISE SPECIFIED
DIMENSIONS ARE IN INCHES
ANGLES ±X.X°
2 PL ±X.XX 3 PL ±X.XXX
SOLID EDGE
UGS - The PLM Company
TITLE
USS Torsion Sample Jig Top
SIZE
D
DWG NO
REV
FILE NAME: Solder_Tube_Jig_Top.dft
SCALE:
WEIGHT:
SHEET 1 OF 1

Figure A.3: Top half of USS torsion sample cooling fixture. All dimensions in inches.

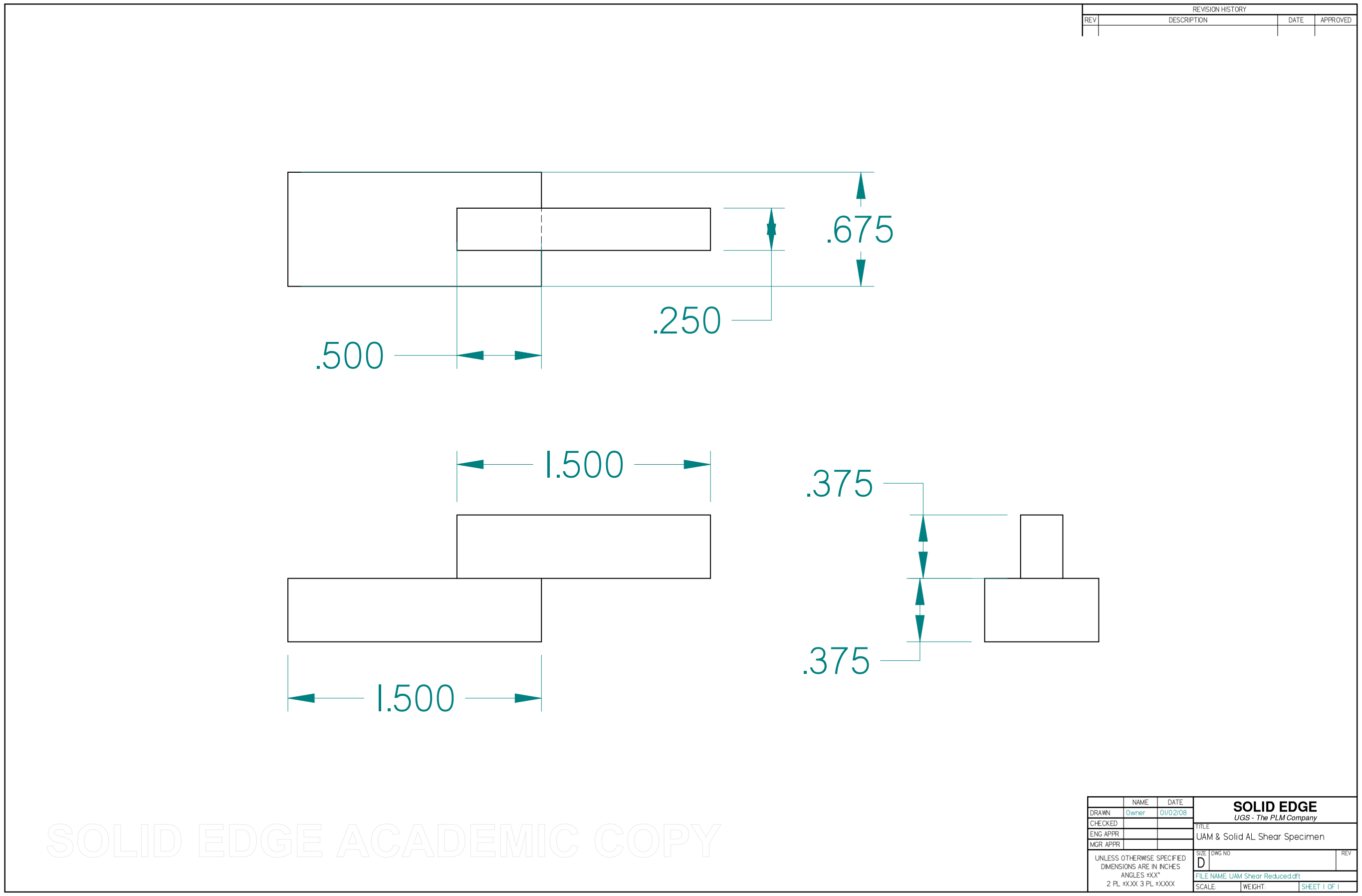

REVISION HISTORY
REV
DESCRIPTION
DATE
APPROVED
.675
.250
.500
1.500
.375
.375
1.500
NAME
DATE
DRAWN
Owner
01/02/08
CHECKED
ENG APPR
MGR APPR
UNLESS OTHERWISE SPECIFIED
DIMENSIONS ARE IN INCHES
ANGLES ±X.X°
2 PL ±X.XX 3 PL ±X.XXX
SOLID EDGE
UGS - The PLM Company
TITLE
UAM & Solid AL Shear Specimen
SIZE
D
DWG NO
REV
FILE NAME: UAM Shear Reduced.dft
SCALE:
WEIGHT:
SHEET 1 OF 1

SOLID EDGE ACADEMIC COPY

Figure A.4: Nominal dimensions for reduced area UAM 1-1 samples. All dimensions in inches.

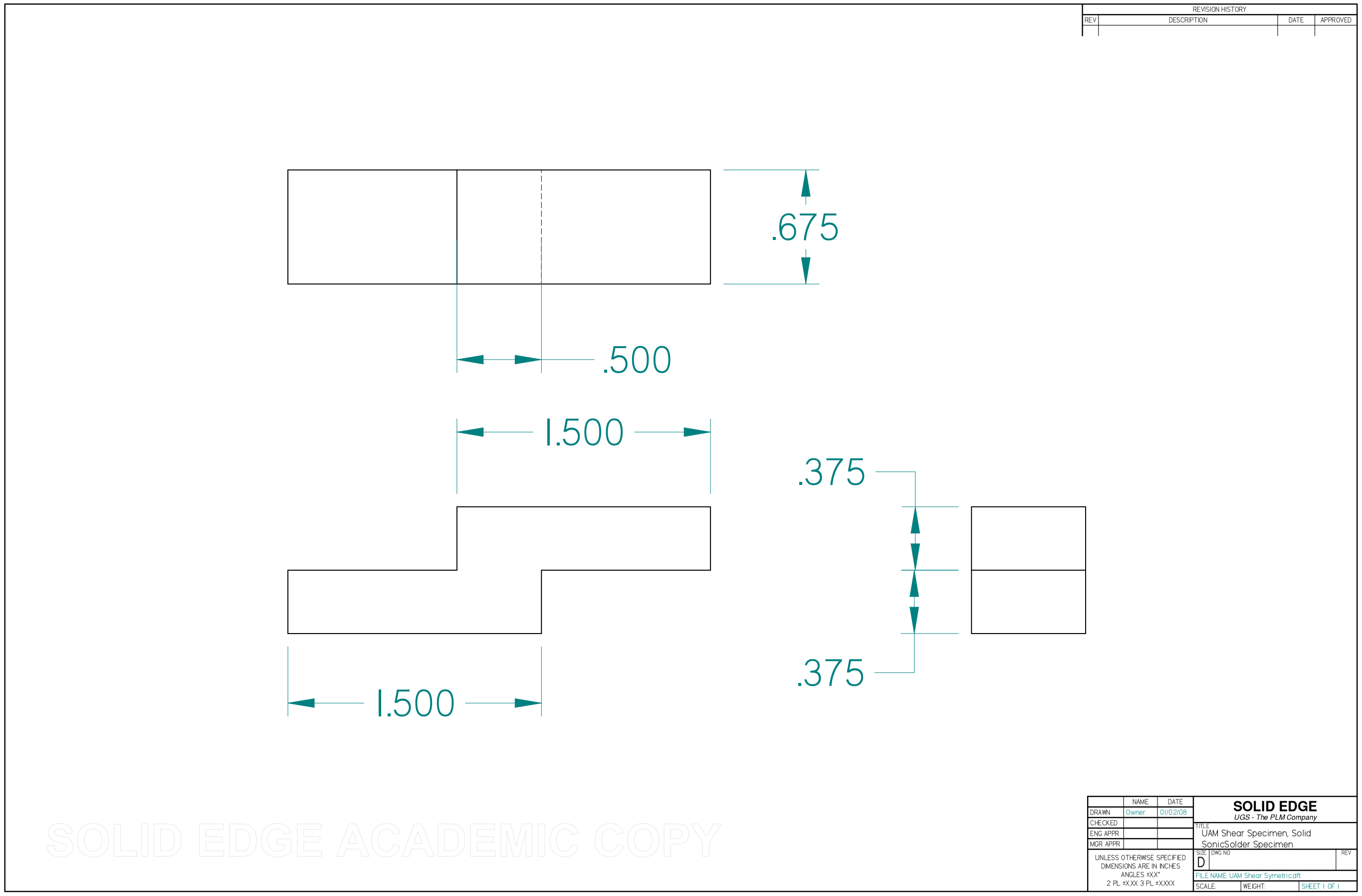
REVISION HISTORY
REV
DESCRIPTION
DATE
APPROVED
.675
.500
1.500
.375
.375
1.500
SOLID EDGE ACADEMIC COPY
NAME
DATE
DRAWN
Owner
01/02/08
CHECKED
ENG APPR
MGR APPR
UNLESS OTHERWISE SPECIFIED
DIMENSIONS ARE IN INCHES
ANGLES ±X.X°
2 PL ±X.XX 3 PL ±X.XXX
SOLID EDGE
UGS - The PLM Company
TITLE
UAM Shear Specimen, Solid
SonicSolder Specimen
SIZE
D
DWG NO
REV
FILE NAME: UAM Shear Symetric.dft
SCALE:
WEIGHT:
SHEET 1 OF 1

Figure A.5: Nominal dimensions for bulk shear sample, lap shear samples, and UAM 1-1 samples. All dimensions in inches.

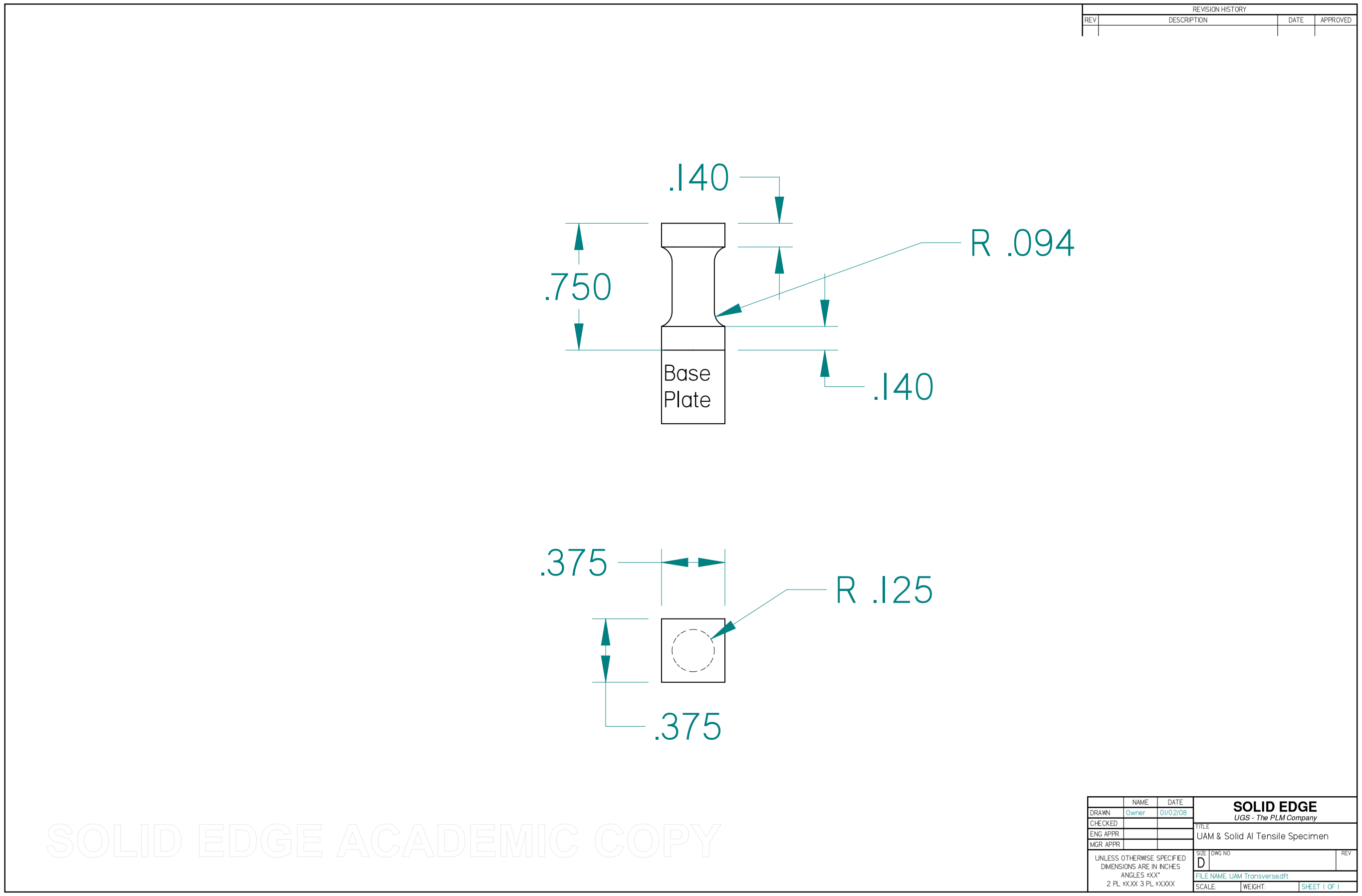
REVISION HISTORY
REV
DESCRIPTION
DATE
APPROVED
.140
R .094
.750
Base
Plate
.140
.375
R .125
.375
SOLID EDGE ACADEMIC COPY
NAME
DATE
DRAWN
Owner
01/02/08
CHECKED
ENG APPR
MGR APPR
UNLESS OTHERWISE SPECIFIED
DIMENSIONS ARE IN INCHES
ANGLES ±X.X°
2 PL ±X.XX 3 PL ±X.XXX
SOLID EDGE
UGS - The PLM Company
TITLE
UAM & Solid Al Tensile Specimen
SIZE
D
DWG NO
REV
FILE NAME: UAM Transverse.dft
SCALE:
WEIGHT:
SHEET 1 OF 1

Figure A.6: Nominal dimensions for UAM 3-2 samples. All dimensions in inches.

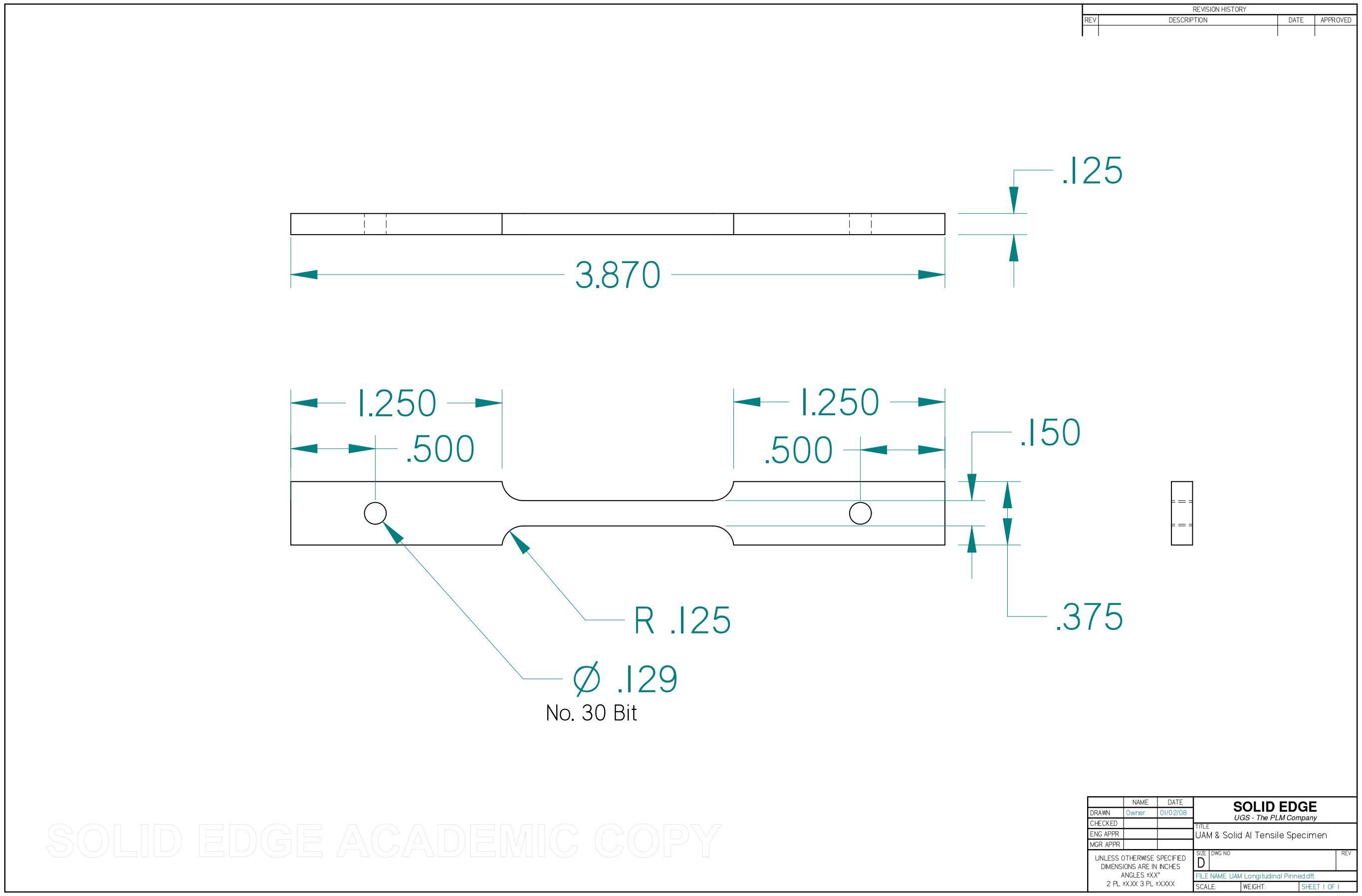
REVISION HISTORY
REV
DESCRIPTION
DATE
APPROVED
.125
3.870
1.250
.500
1.250
.500
.150
.375
R .125
∅ .129
No. 30 Bit
SOLID EDGE ACADEMIC COPY
NAME
DATE
DRAWN
Owner
01/02/08
CHECKED
ENG APPR
MGR APPR
UNLESS OTHERWISE SPECIFIED
DIMENSIONS ARE IN INCHES
ANGLES ±X.X°
2 PL ±X.XX 3 PL ±X.XXX
SOLID EDGE
UGS - The PLM Company
TITLE
UAM & Solid Al Tensile Specimen
SIZE
D
DWG NO
REV
FILE NAME: UAM Longitudinal Pinned.dft
SCALE:
WEIGHT:
SHEET 1 OF 1

Figure A.7: Nominal dimensions for UAM 1-2 samples. All dimensions in inches.

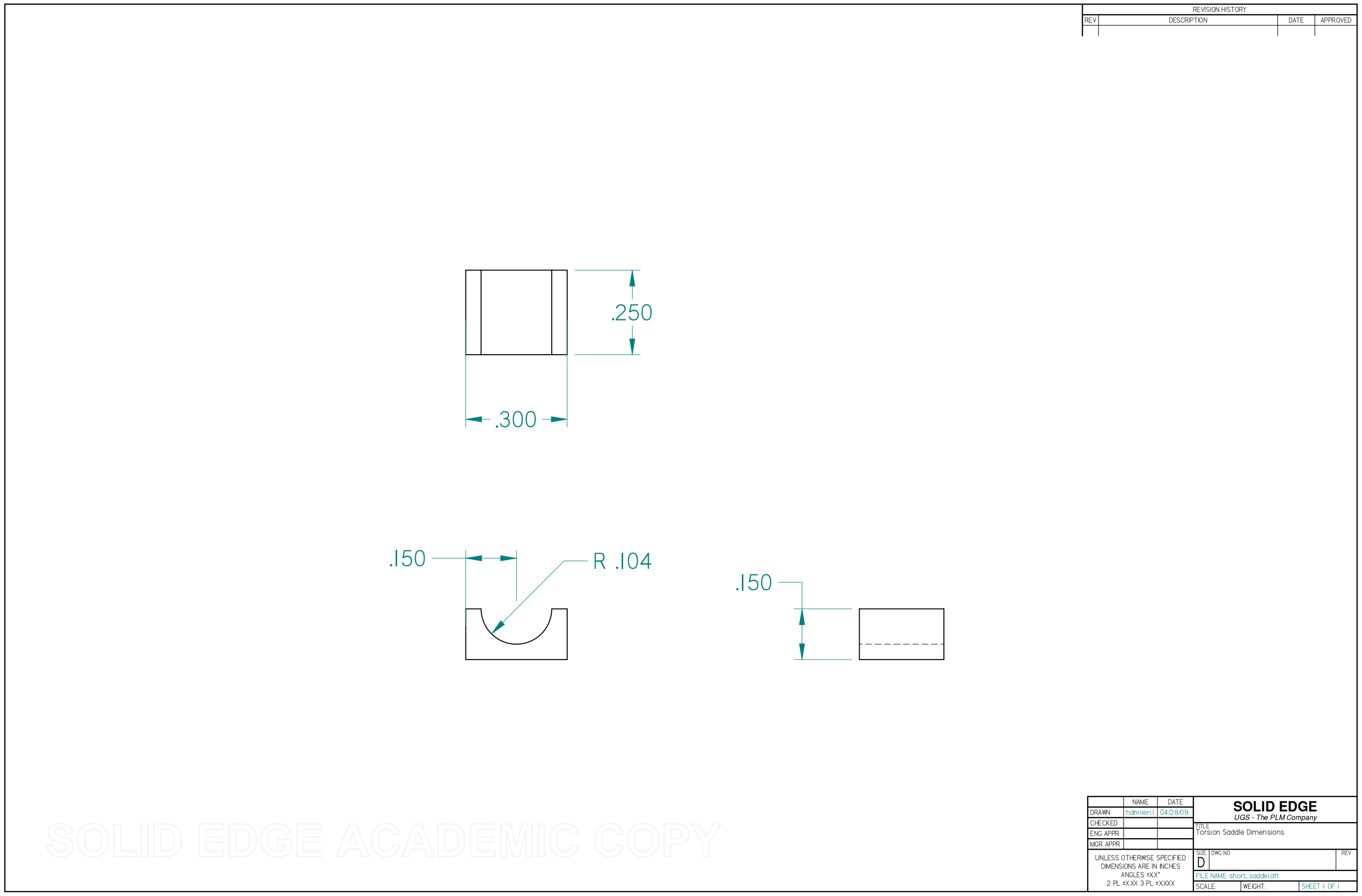
REVISION HISTORY
REV
DESCRIPTION
DATE
APPROVED
.250
.300
.150
R .104
.150
SOLID EDGE ACADEMIC COPY
NAME
DATE
DRAWN
hahnlen.l
04/28/09
CHECKED
ENG APPR
MGR APPR
UNLESS OTHERWISE SPECIFIED
DIMENSIONS ARE IN INCHES
ANGLES ±X.X°
2 PL ±X.XX 3 PL ±X.XXX
SOLID EDGE
UGS - The PLM Company
TITLE
Torsion Saddle Dimensions
SIZE
D
DWG NO
REV
FILE NAME: short_saddel.dft
SCALE:
WEIGHT:
SHEET 1 OF 1

Figure A.8: USS Al 2024 torsion short saddle. All dimensions in inches.

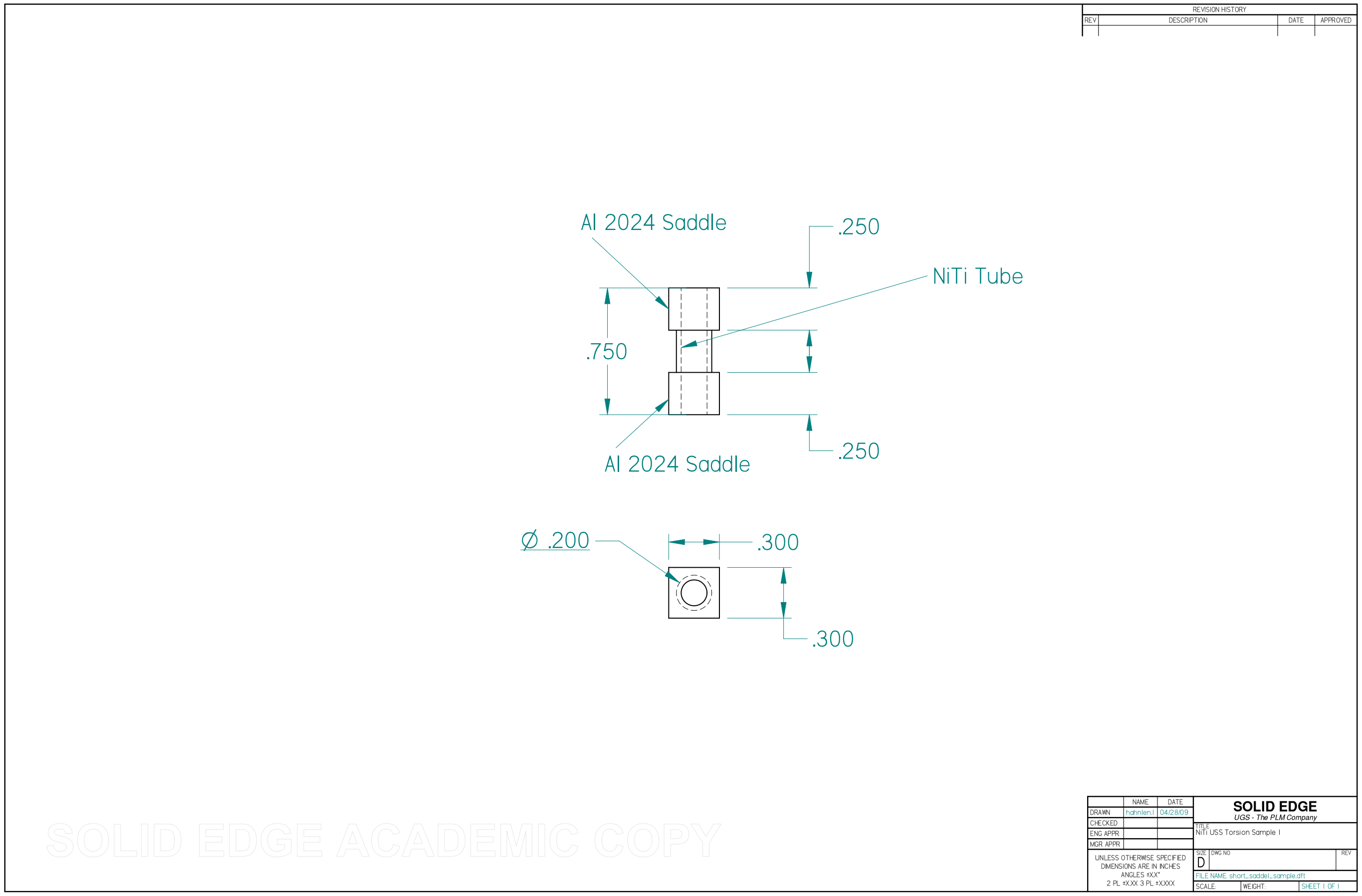
REVISION HISTORY
REV
DESCRIPTION
DATE
APPROVED
Al 2024 Saddle
.250
NiTi Tube
.750
.250
Al 2024 Saddle
Ø .200
.300
.300
SOLID EDGE ACADEMIC COPY
NAME
DATE
DRAWN
hahnlen.l
04/28/09
CHECKED
ENG APPR
MGR APPR
UNLESS OTHERWISE SPECIFIED
DIMENSIONS ARE IN INCHES
ANGLES ±X.X°
2 PL ±X.XX 3 PL ±X.XXX
SOLID EDGE
UGS - The PLM Company
TITLE
NiTi USS Torsion Sample I
SIZE
D
DWG NO
REV
FILE NAME: short_saddel_sample.dft
SCALE:
WEIGHT:
SHEET 1 OF 1

Figure A.9: USS NiTi/Al 2024 torsion sample with short saddles. All dimensions in inches.

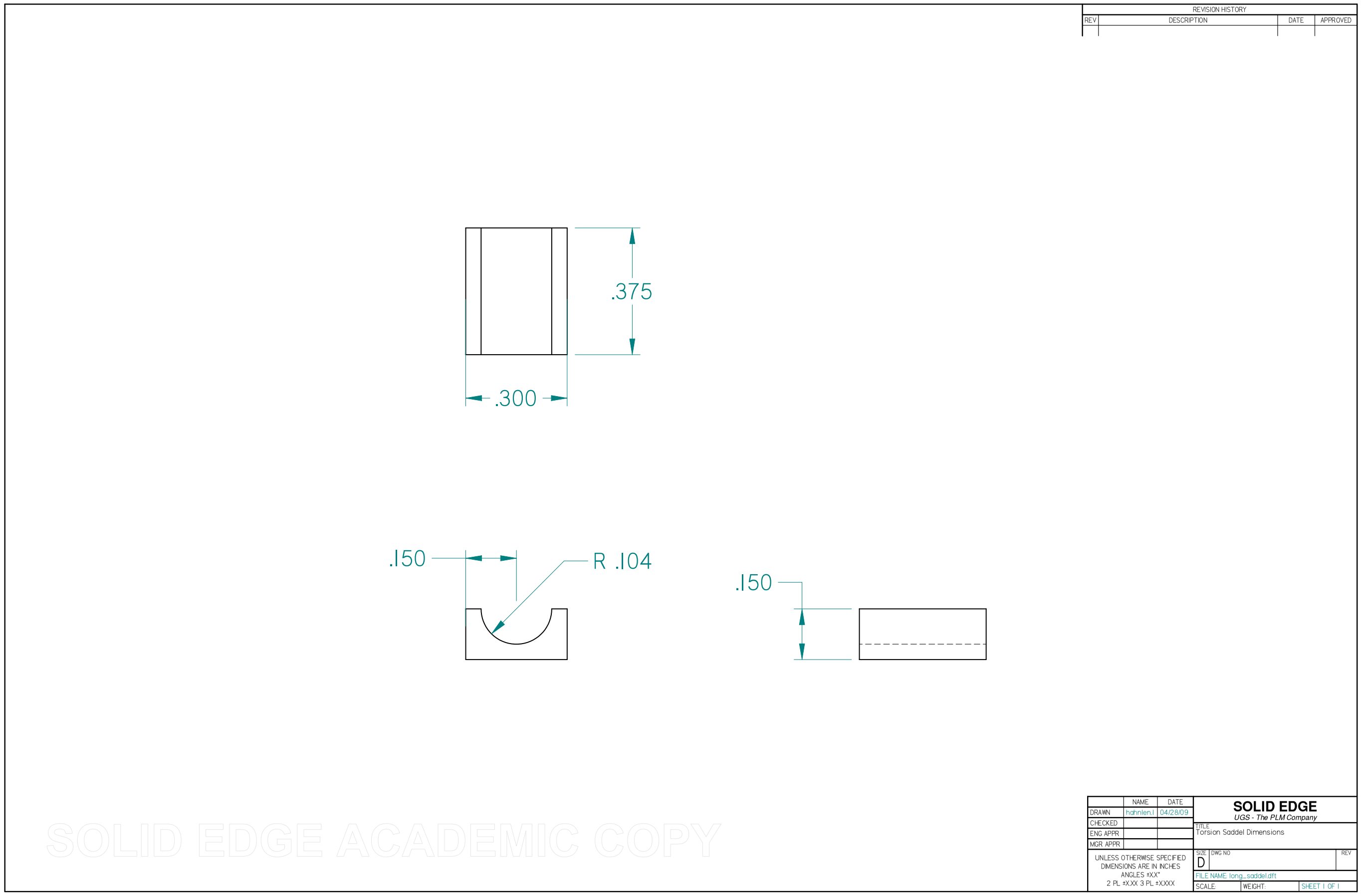
REVISION HISTORY
REV
DESCRIPTION
DATE
APPROVED
.375
.300
.150
R .104
.150
SOLID EDGE ACADEMIC COPY
NAME
DATE
DRAWN
hahnlen.l
04/28/09
CHECKED
ENG APPR
MGR APPR
UNLESS OTHERWISE SPECIFIED
DIMENSIONS ARE IN INCHES
ANGLES ±X.X°
2 PL ±X.XX 3 PL ±X.XXX
SOLID EDGE
UGS - The PLM Company
TITLE
Torsion Saddel Dimensions
SIZE
D
DWG NO
REV
FILE NAME: long_saddel.dft
SCALE:
WEIGHT:
SHEET 1 OF 1

Figure A.10: USS Al 2024 torsion long saddle. All dimensions in inches.

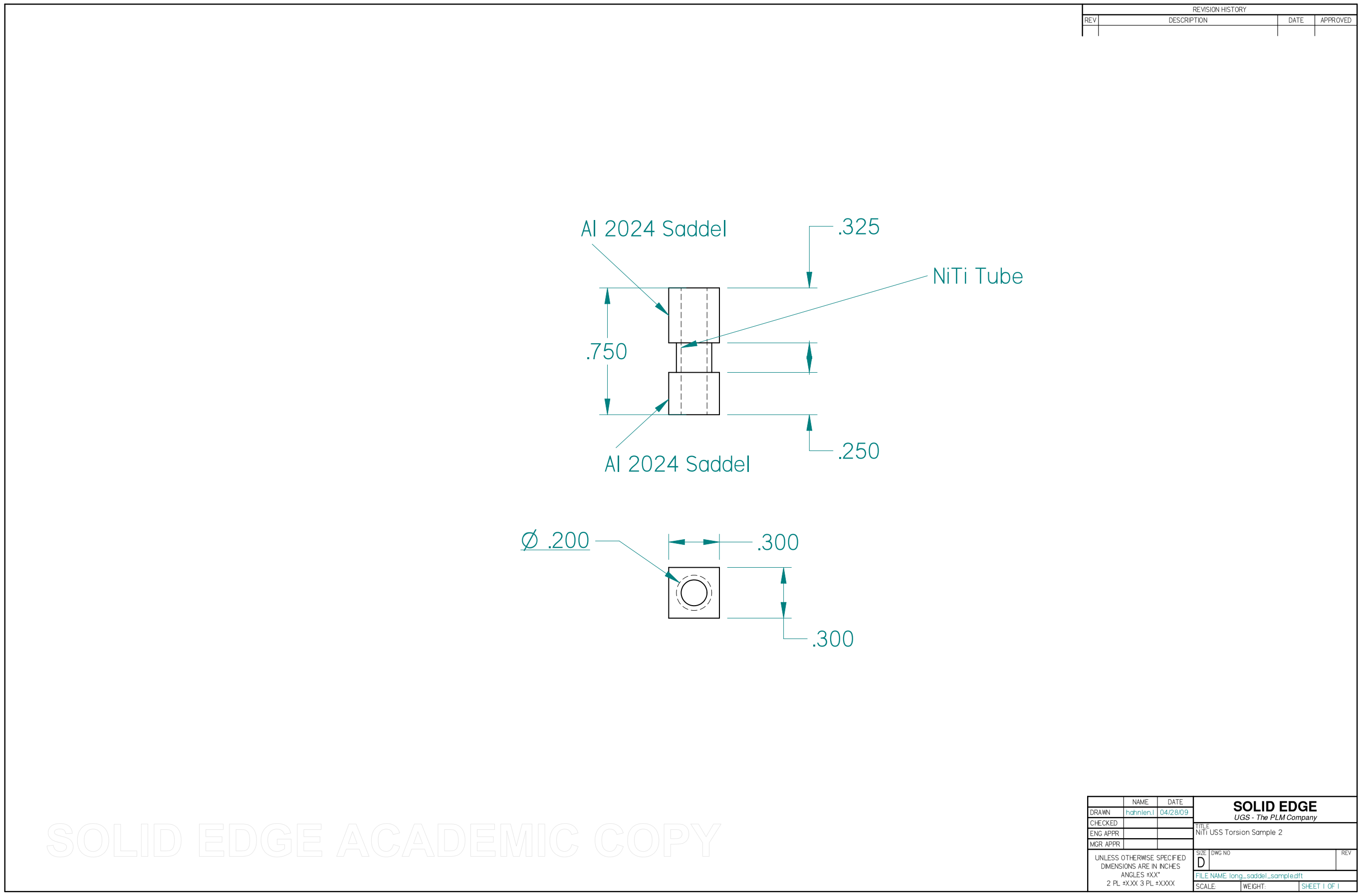
REVISION HISTORY
REV
DESCRIPTION
DATE
APPROVED
Al 2024 Saddel
.325
NiTi Tube
.750
Al 2024 Saddel
.250
Ø .200
.300
.300
SOLID EDGE ACADEMIC COPY
NAME
DATE
DRAWN
hahnlen.l
04/28/09
CHECKED
ENG APPR
MGR APPR
UNLESS OTHERWISE SPECIFIED
DIMENSIONS ARE IN INCHES
ANGLES ±X.X°
2 PL ±X.XX 3 PL ±X.XXX
SOLID EDGE
UGS - The PLM Company
TITLE
NiTi USS Torsion Sample 2
SIZE
D
DWG NO
REV
FILE NAME: long_saddel_sample.dft
SCALE:
WEIGHT:
SHEET 1 OF 1

Figure A.11: USS NiTi/Al 2024 torsion sample with long saddles. All dimensions in inches.

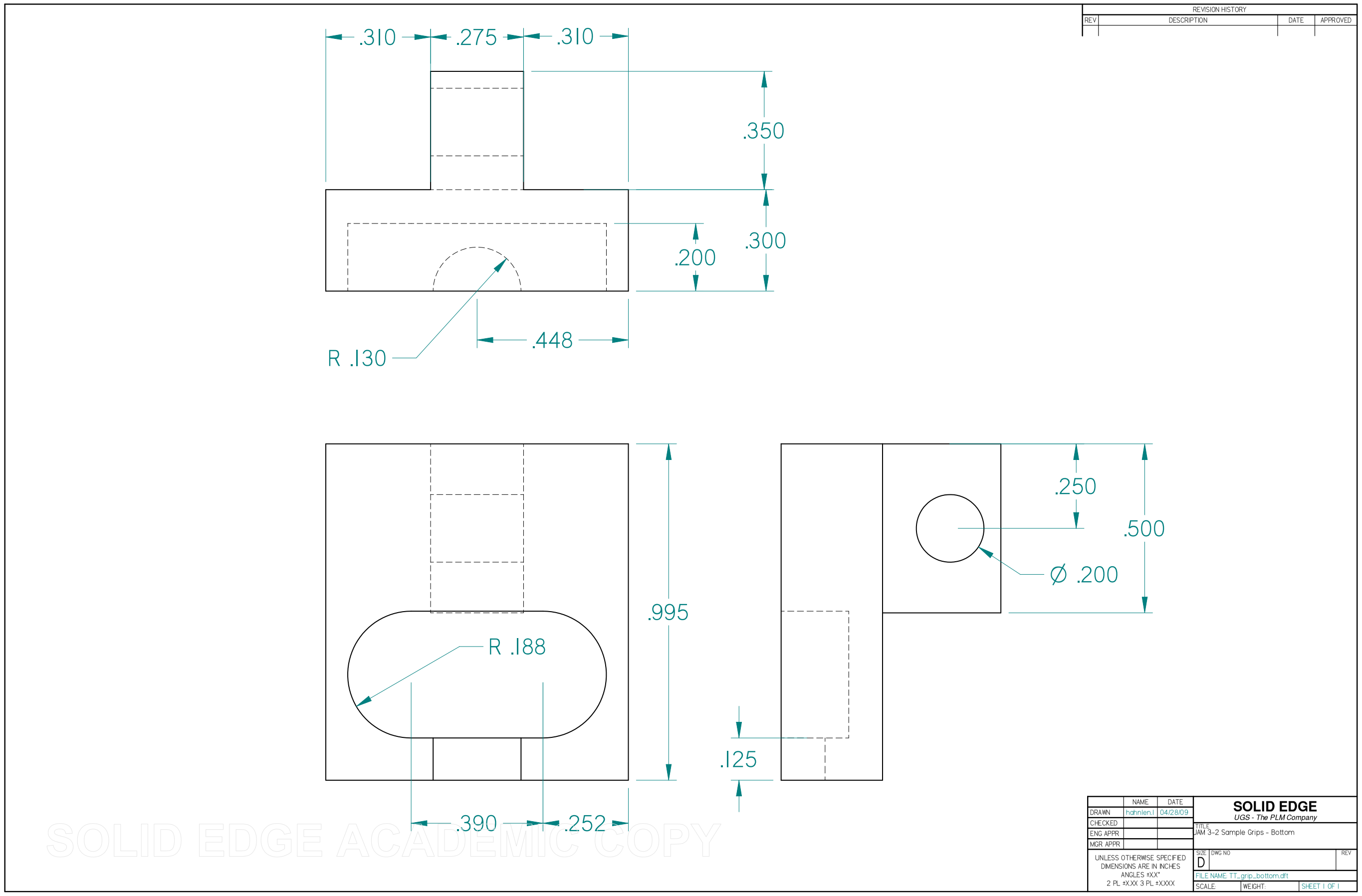
REVISION HISTORY
REV
DESCRIPTION
DATE
APPROVED
.310
.275
.310
.350
.300
.200
R .130
.448
.995
R .188
.390
.252
.125
.250
.500
Ø .200
NAME
DATE
DRAWN
hahnlen.l
04/28/09
CHECKED
ENG APPR
MGR APPR
UNLESS OTHERWISE SPECIFIED
DIMENSIONS ARE IN INCHES
ANGLES ±X.X°
2 PL ±X.XX 3 PL ±X.XXX
SOLID EDGE
UGS - The PLM Company
TITLE
UAM 3-2 Sample Grips - Bottom
SIZE
D
DWG NO
REV
FILE NAME: TT_grip_bottom.dft
SCALE:
WEIGHT:
SHEET 1 OF 1

SOLID EDGE ACADEMIC COPY

Figure A.12: Tensile test bottom grip use for bulk solder and UAM 3-2 tests. All dimensions in inches.

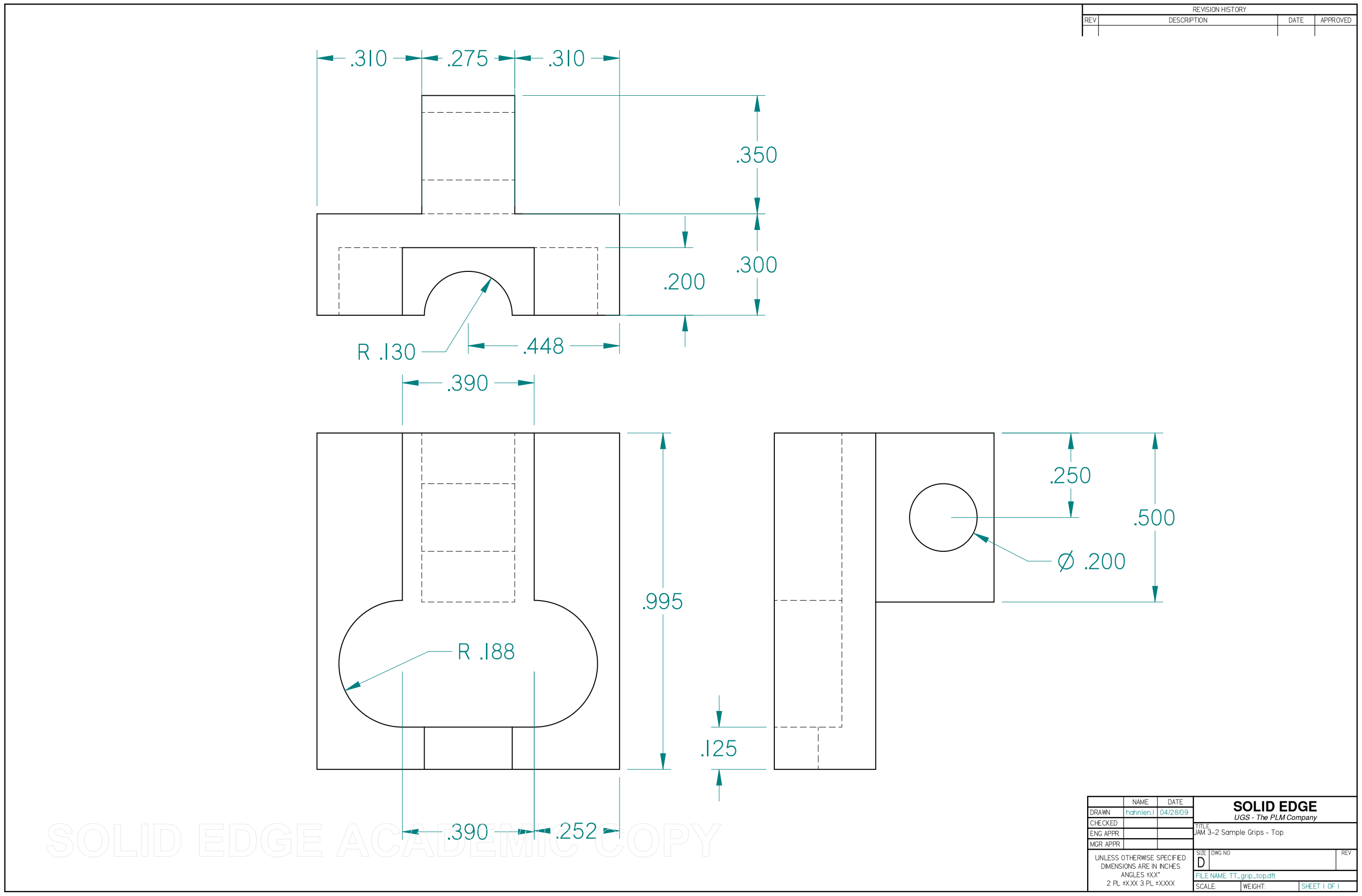
REVISION HISTORY
REV
DESCRIPTION
DATE
APPROVED
.310
.275
.310
.350
.300
.200
R .130
.448
.390
.995
R .188
.390
.252
.125
.250
.500
Ø .200
SOLID EDGE ACADEMIC COPY
NAME
DATE
DRAWN
hahnlen.l
04/28/09
CHECKED
ENG APPR
MGR APPR
UNLESS OTHERWISE SPECIFIED
DIMENSIONS ARE IN INCHES
ANGLES ±X.X°
2 PL ±X.XX 3 PL ±X.XXX
SOLID EDGE
UGS - The PLM Company
TITLE
UAM 3-2 Sample Grips - Top
SIZE
D
DWG NO
REV
FILE NAME: TT_grip_top.dft
SCALE:
WEIGHT:
SHEET 1 OF 1

Figure A.13: Tensile test bottom grip use for bulk solder and UAM 3-2 tests. All dimensions in inches.

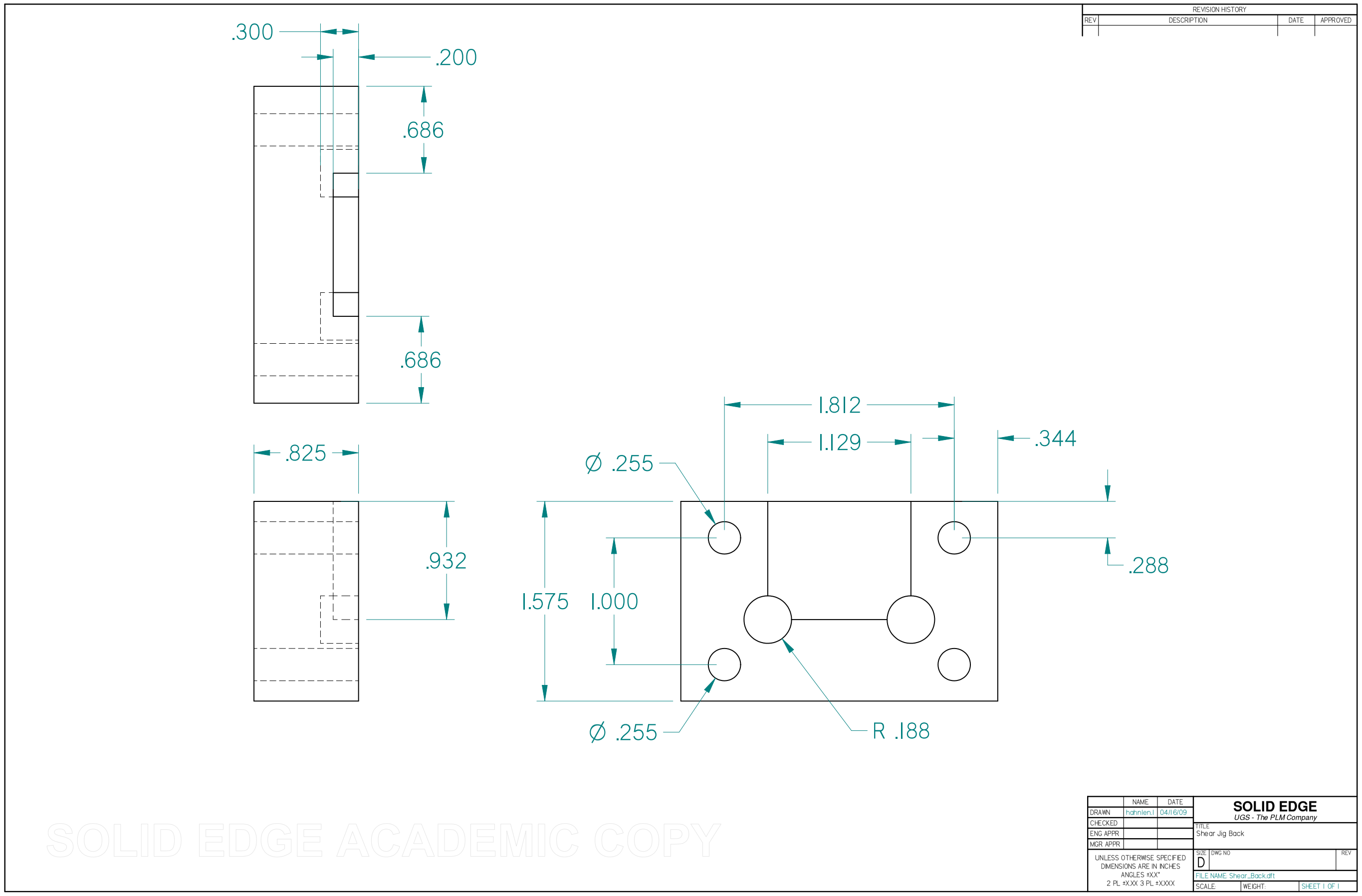
REVISION HISTORY
REV
DESCRIPTION
DATE
APPROVED
.300
.200
.686
.686
.825
.932
1.812
1.129
.344
.288
Ø .255
Ø .255
1.575
1.000
R .188
SOLID EDGE ACADEMIC COPY
NAME
DATE
DRAWN
hahnlen.l
04/16/09
CHECKED
ENG APPR
MGR APPR
UNLESS OTHERWISE SPECIFIED
DIMENSIONS ARE IN INCHES
ANGLES ±X.X°
2 PL ±X.XX 3 PL ±X.XXX
SOLID EDGE
UGS - The PLM Company
TITLE
Shear Jig Back
SIZE
D
DWG NO
REV
FILE NAME: Shear_Back.dft
SCALE:
WEIGHT:
SHEET 1 OF 1

Figure A.14: Shear testing jig back half used for bulk solder, USS lap shear, and UAM tests. All dimensions in inches.

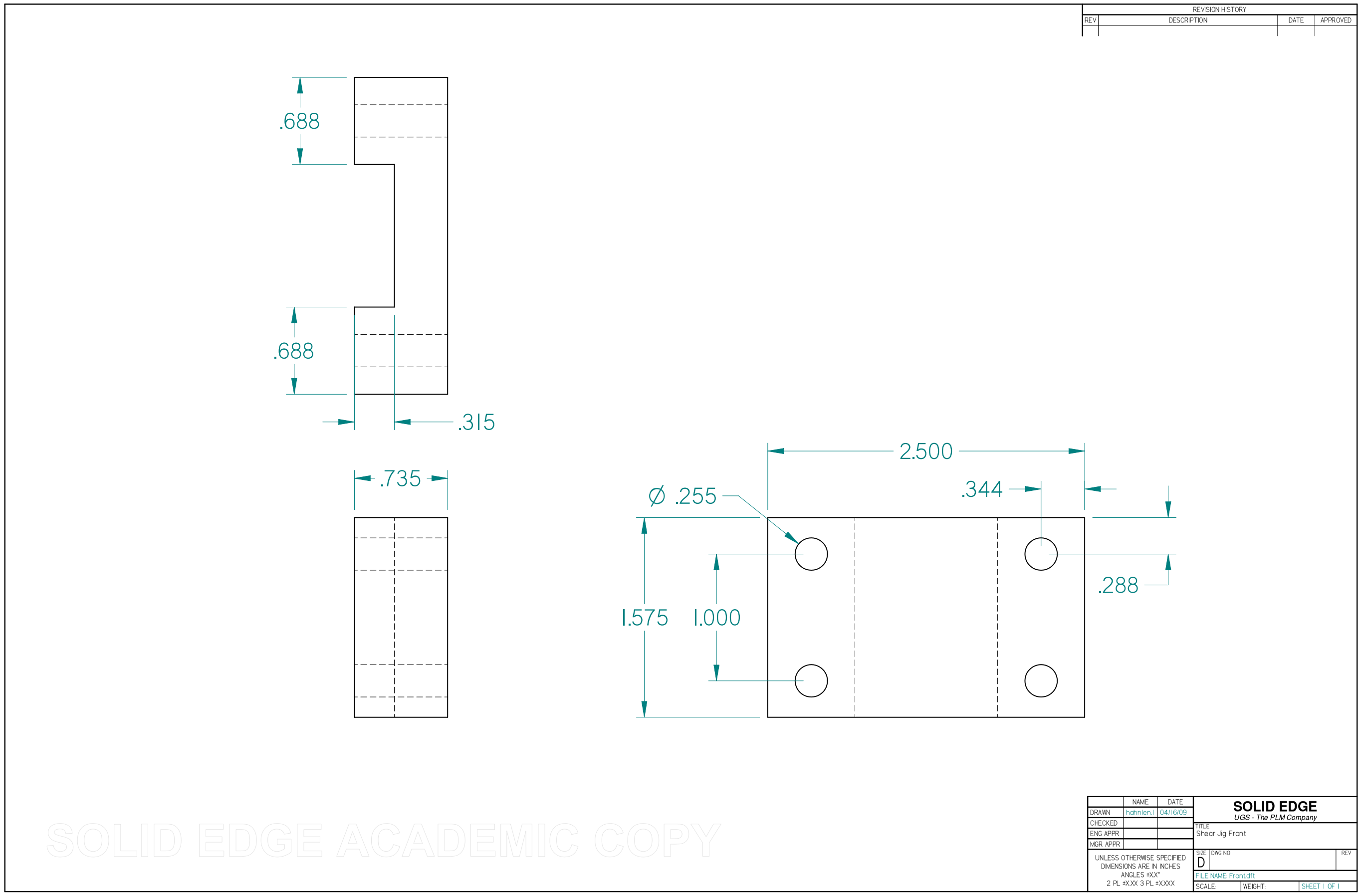
REVISION HISTORY
REV
DESCRIPTION
DATE
APPROVED
.688
.688
.315
.735
2.500
.344
Ø .255
.288
1.575
1.000
SOLID EDGE ACADEMIC COPY
NAME
DATE
DRAWN
hahnlen.l
04/16/09
CHECKED
ENG APPR
MGR APPR
UNLESS OTHERWISE SPECIFIED
DIMENSIONS ARE IN INCHES
ANGLES ±X.X°
2 PL ±X.XX 3 PL ±X.XXX
SOLID EDGE
UGS - The PLM Company
TITLE
Shear Jig Front
SIZE
D
DWG NO
REV
FILE NAME: Front.dft
SCALE:
WEIGHT:
SHEET 1 OF 1

Figure A.15: Shear testing jig front half used for bulk solder, USS lap shear, and UAM tests. All dimensions in inches.

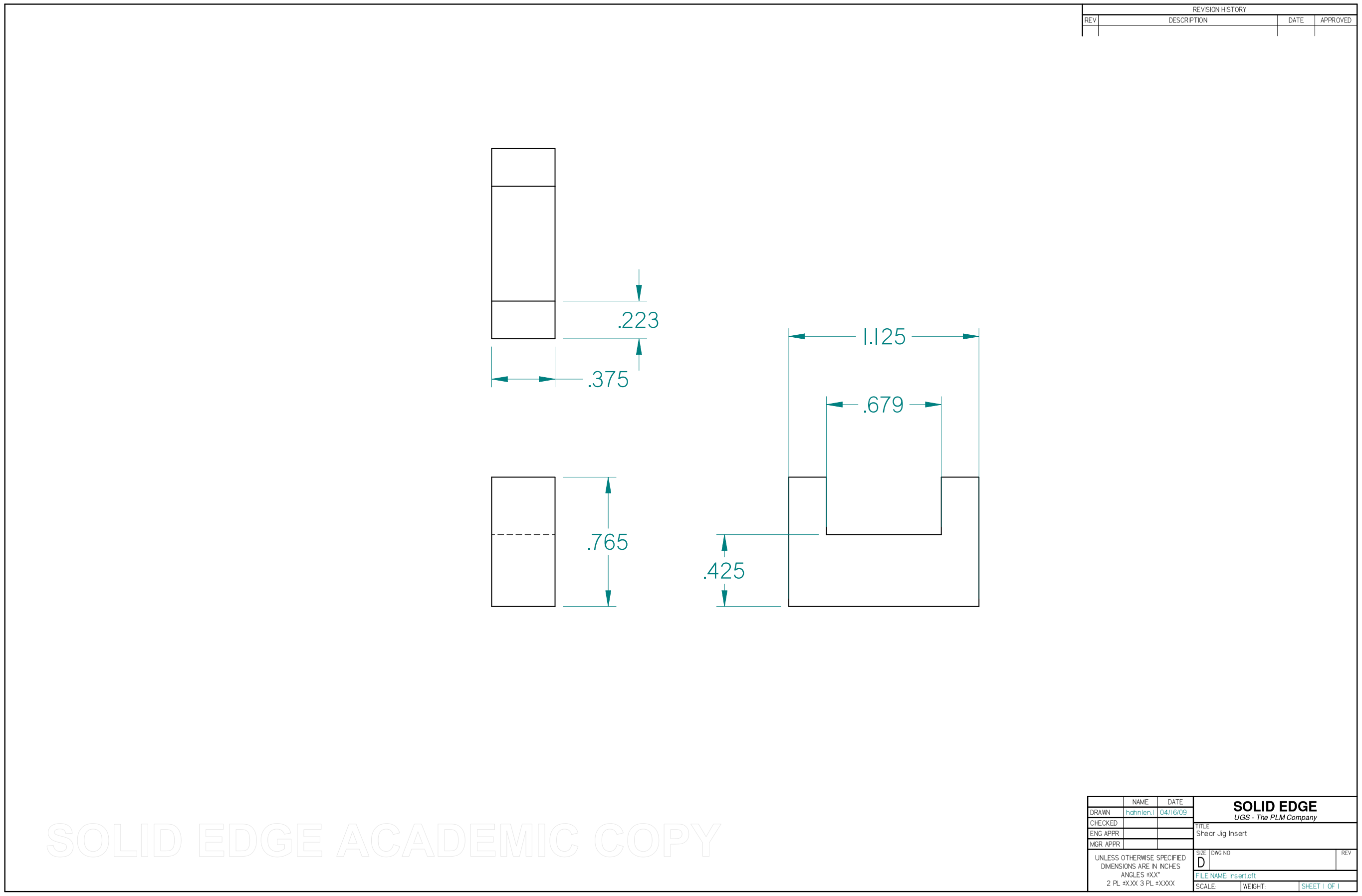
REVISION HISTORY
REV
DESCRIPTION
DATE
APPROVED
.223
.375
I.I25
.679
.765
.425
SOLID EDGE ACADEMIC COPY
NAME
DATE
DRAWN
hahnlen.l
04/16/09
CHECKED
ENG APPR
MGR APPR
UNLESS OTHERWISE SPECIFIED
DIMENSIONS ARE IN INCHES
ANGLES ±X.X°
2 PL ±X.XX 3 PL ±X.XXX
SOLID EDGE
UGS - The PLM Company
TITLE
Shear Jig Insert
SIZE
D
DWG NO
REV
FILE NAME: Insert.dft
SCALE:
WEIGHT:
SHEET 1 OF 1

Figure A.16: Shear testing jig, insert used to ensure proper fit of shear sample. All dimensions in inches.

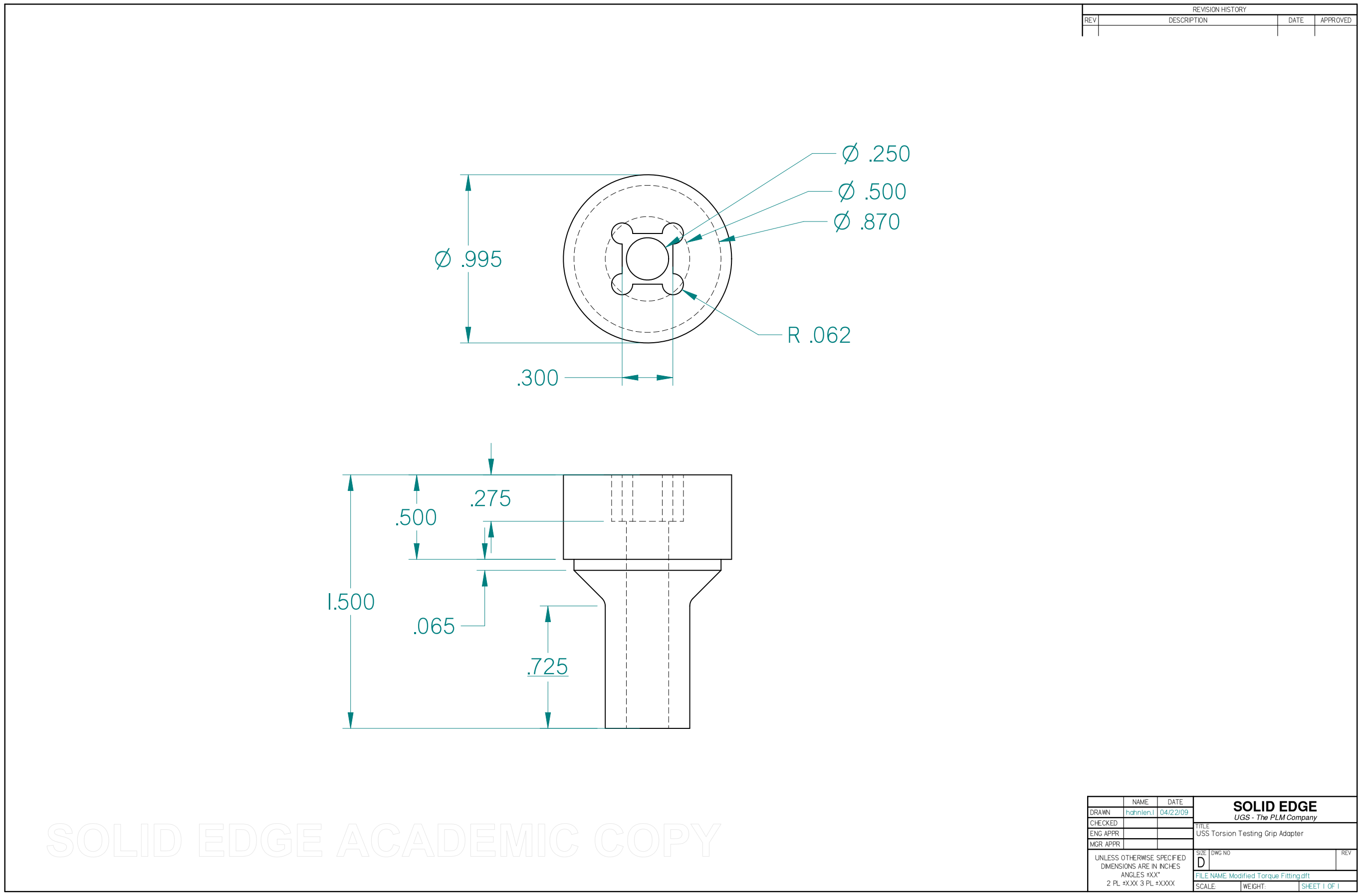
REVISION HISTORY
REV
DESCRIPTION
DATE
APPROVED
Ø .250
Ø .500
Ø .870
Ø .995
R .062
.300
.275
.500
1.500
.065
.725
SOLID EDGE ACADEMIC COPY
NAME
DATE
DRAWN
hahnlen.l
04/22/09
CHECKED
ENG APPR
MGR APPR
UNLESS OTHERWISE SPECIFIED
DIMENSIONS ARE IN INCHES
ANGLES ±X.X°
2 PL ±X.XX 3 PL ±X.XXX
SOLID EDGE
UGS - The PLM Company
TITLE
USS Torsion Testing Grip Adapter
SIZE
D
DWG NO
REV
FILE NAME: Modified Torque Fitting.dft
SCALE:
WEIGHT:
SHEET 1 OF 1

Figure A.17: Torsion testing grip adapter for USS torsion samples. All dimensions in inches.

APPENDIX B

NITI/304 SS LASER WELD SECTION MICROGRAPHS

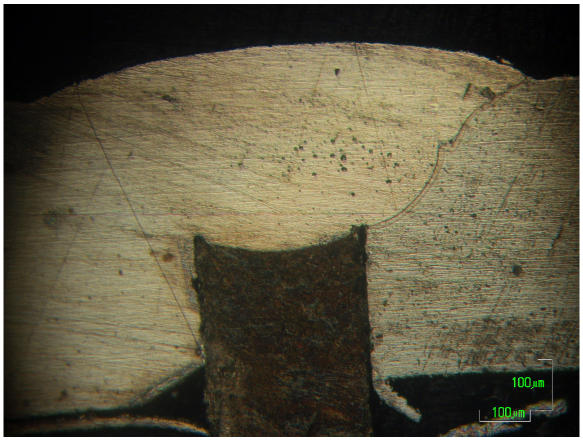
100µm
100µm

Figure B.1: Laser weld sample 1a micrograph.

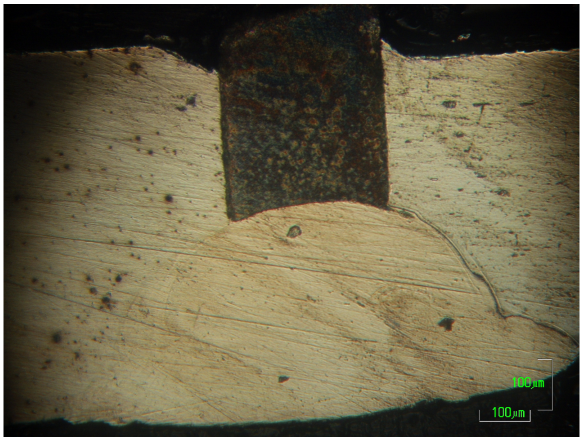
100µm
100µm

Figure B.2: Laser weld sample 1b micrograph.

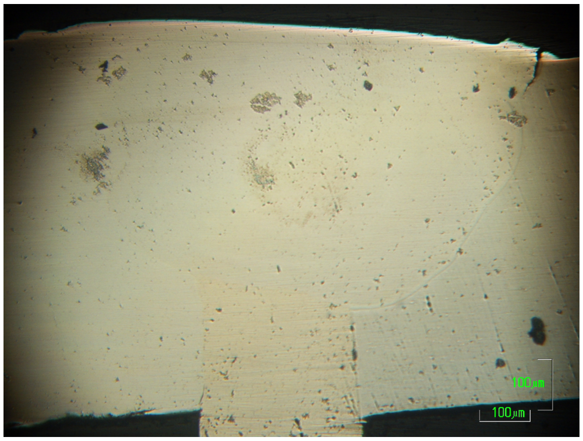
100μm
100μm

Figure B.3: Laser weld sample 2a micrograph.

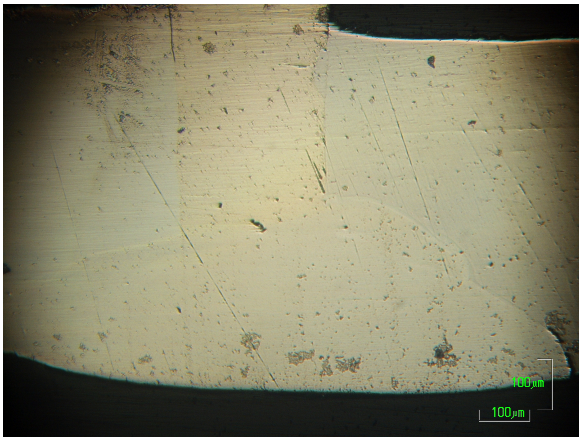
100μm
100μm

Figure B.4: Laser weld sample 2b micrograph.

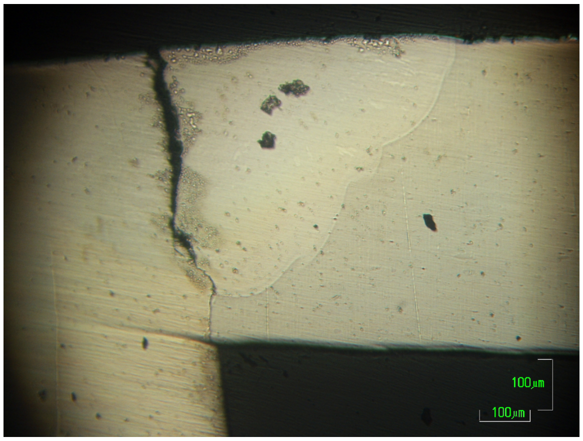
100µm
100µm

Figure B.5: Laser weld sample 3a micrograph.

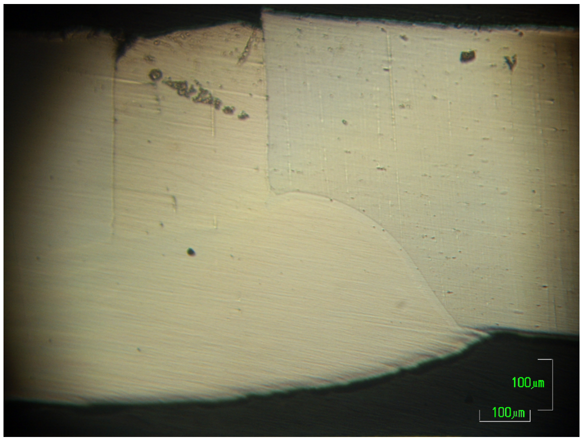
100µm
100µm

Figure B.6: Laser weld sample 3b micrograph.

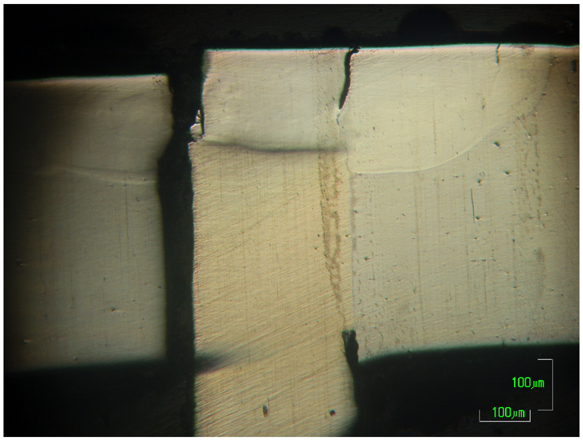
100µm
100µm

Figure B.7: Laser weld sample 4a micrograph.

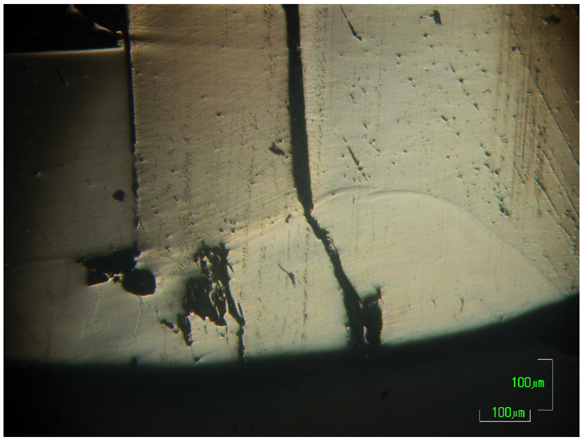
100µm
100µm

Figure B.8: Laser weld sample 4b micrograph.

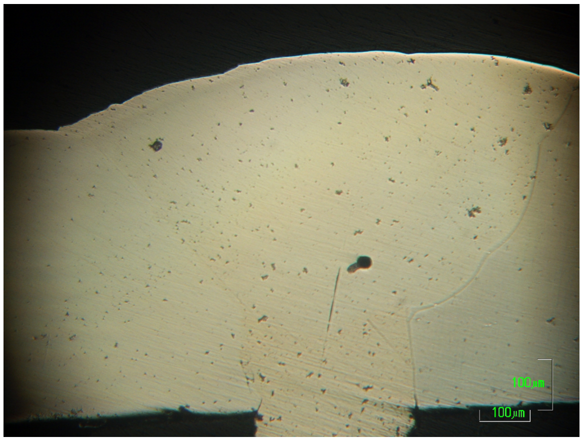
100µm
100µm

Figure B.9: Laser weld sample 5a micrograph.

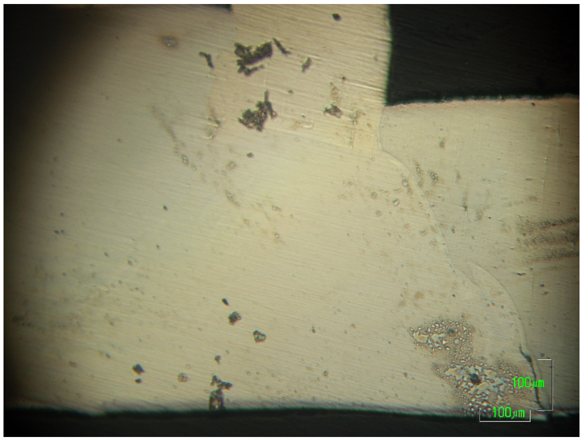
100µm
100µm

Figure B.10: Laser weld sample 5b micrograph.

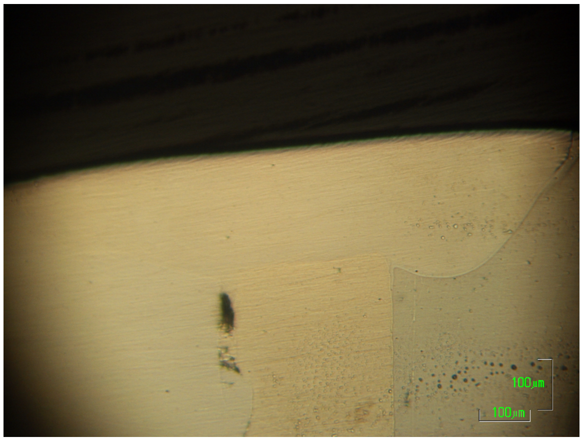
100µm
100µm

Figure B.11: Laser weld sample 6a micrograph.

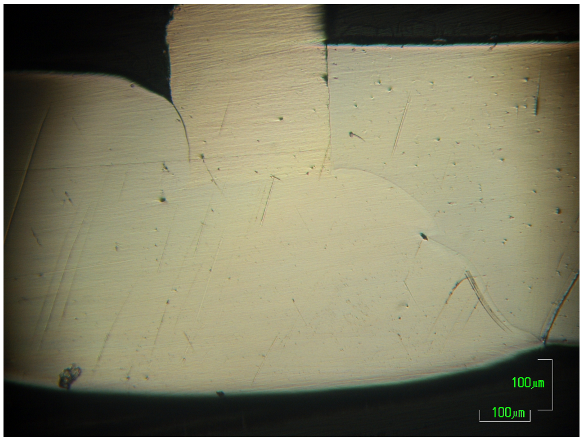
100µm
100µm

Figure B.12: Laser weld sample 6b micrograph.

APPENDIX C

USS FORCE VERSUS DISPLACEMENT PLOTS

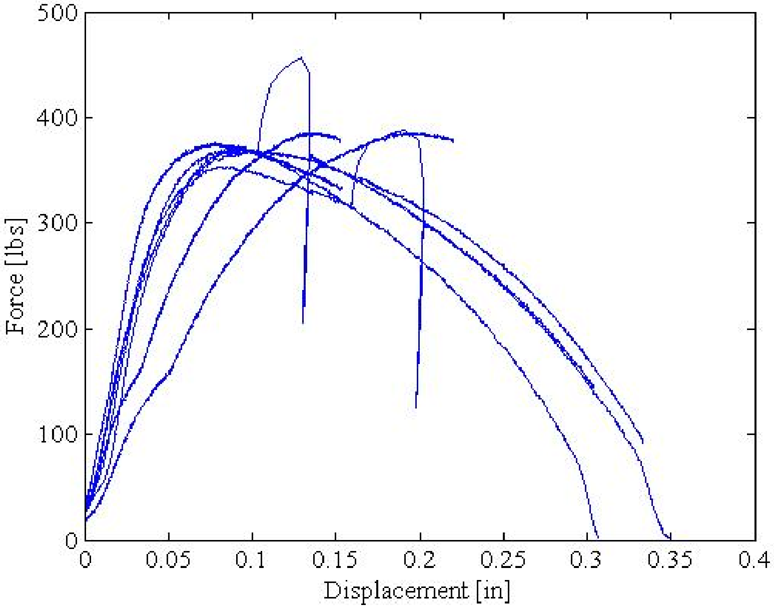

Figure C.1: Solid SonicSolder^{TM} force versus displacement sample comparison plots.

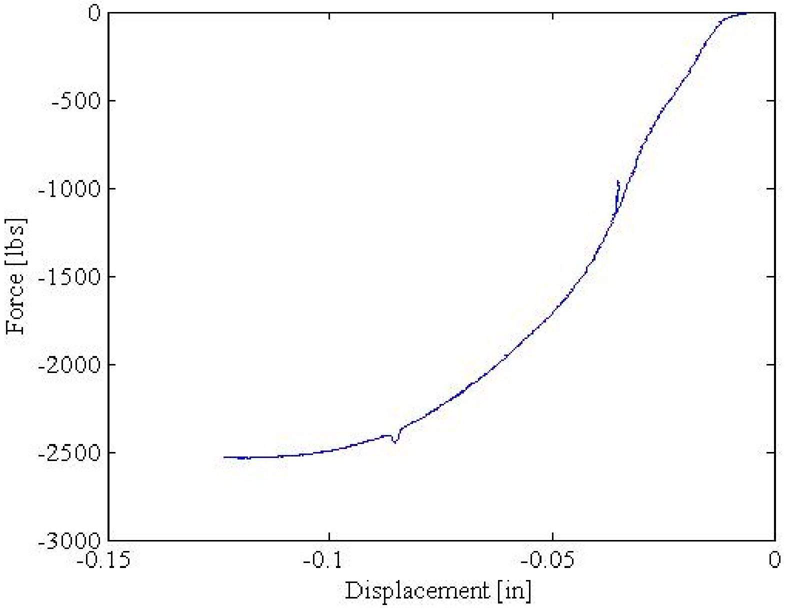

Figure C.2: Solid SonicSolder^{TM} shear sample force versus displacement plot.

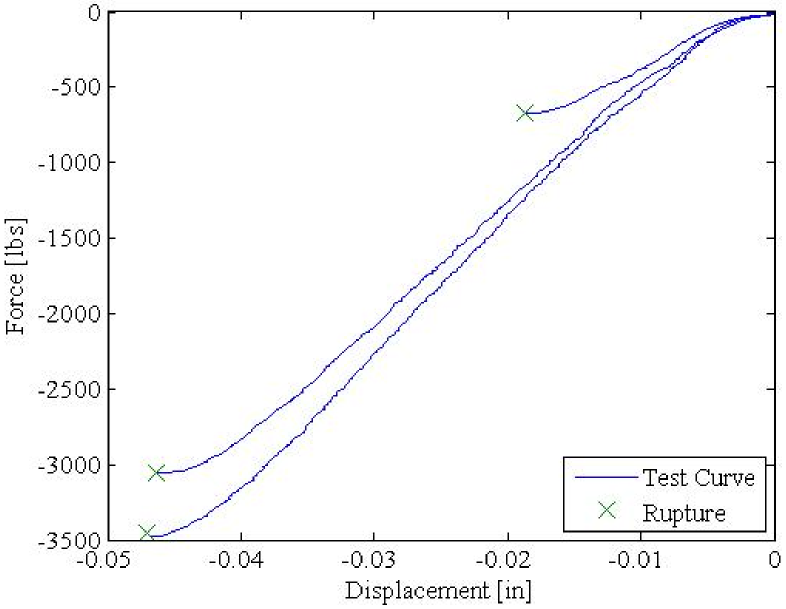

Figure C.3: USS Al 2024 lap shear force versus displacement comparison plots. No surface treatment.

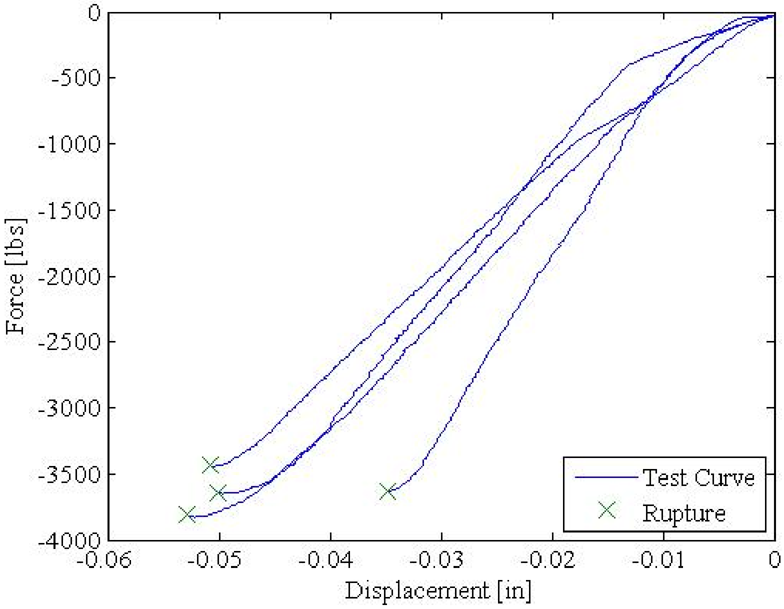

Figure C.4: USS Al 2024 lap shear force versus displacement comparison plots. Joined after 50 μm SiC grit blast and methanol rinse.

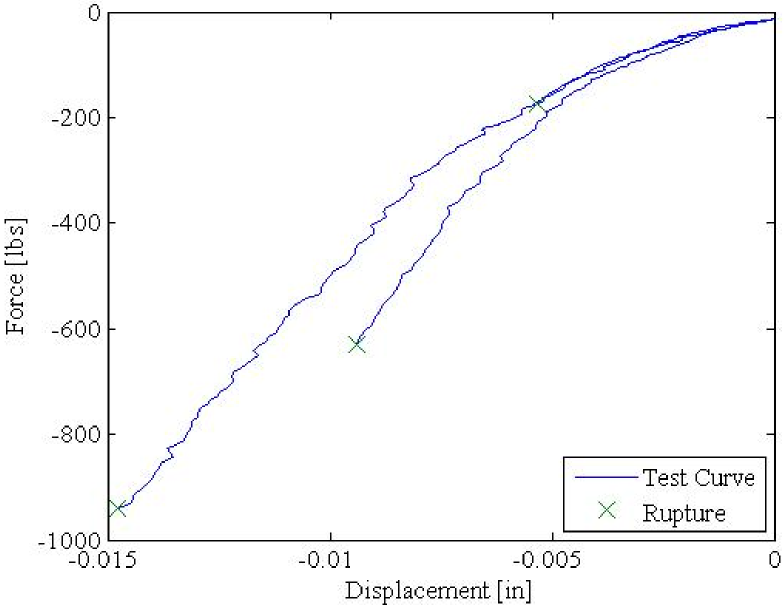

Figure C.5: USS O1 tool steel lap shear force versus displacement comparison plots. No surface treatment.

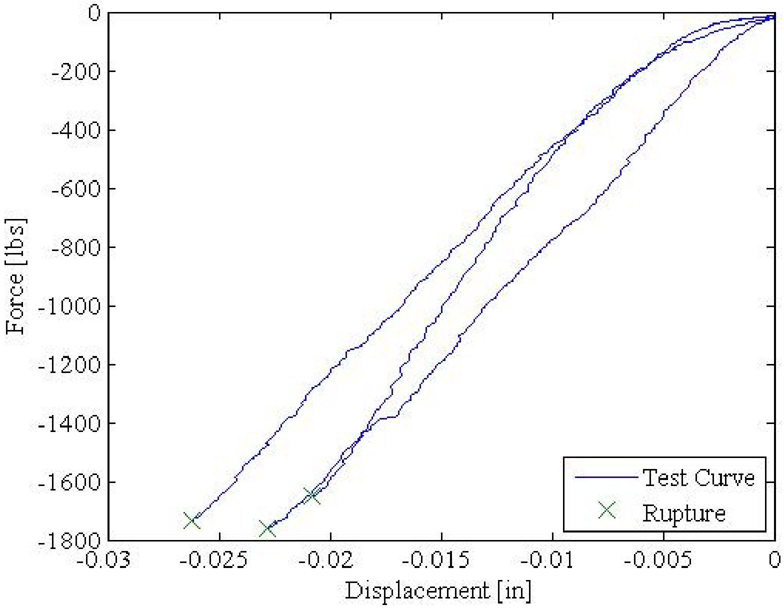

Figure C.6: USS O1 tool steel lap shear force versus displacement comparison plots. Joined after 50 μm SiC grit blast and methanol rinse.

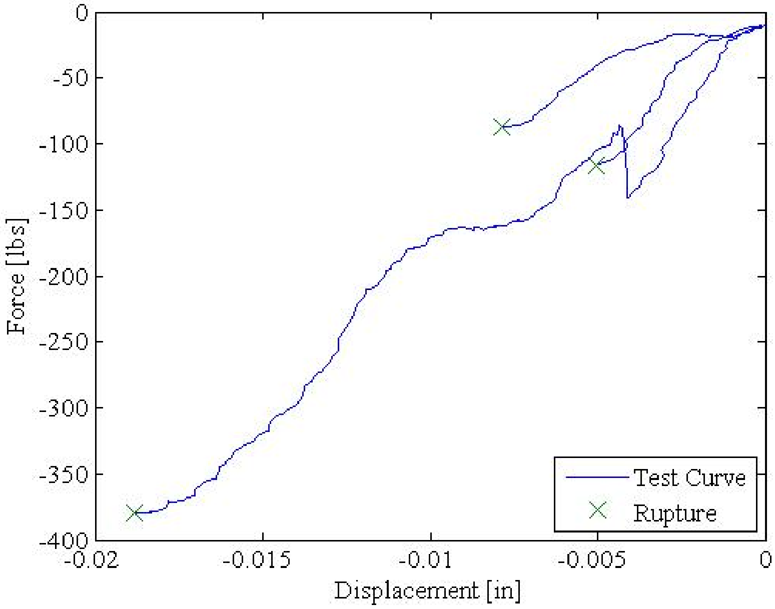

Figure C.7: USS 304 SS lap shear force versus displacement comparison plots. No surface treatment.

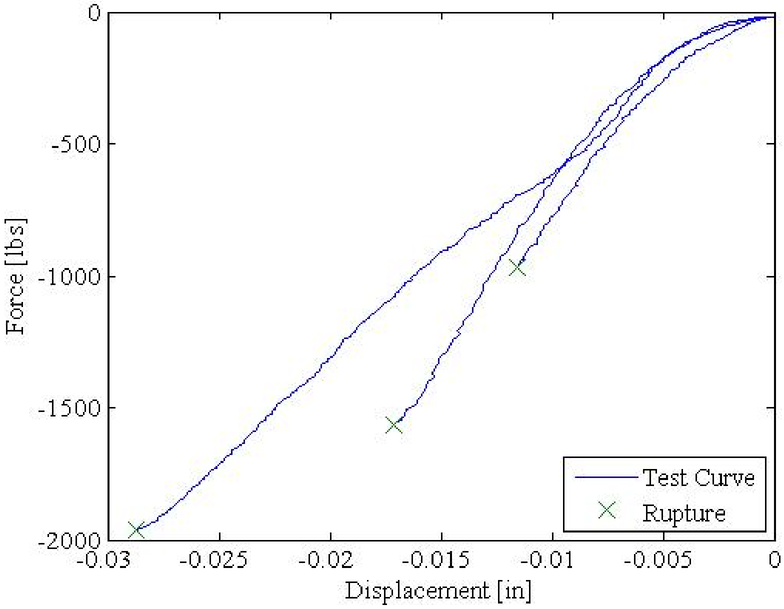

Figure C.8: USS 304 SS lap shear force versus displacement comparison plots. Joined after 50 μm SiC grit blast and methanol rinse.

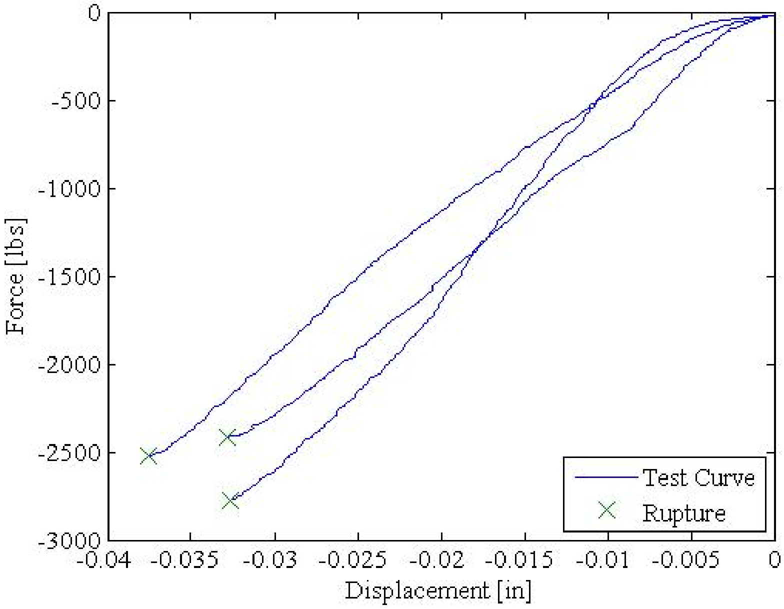

Figure C.9: USS NiTi/Al 2024 lap shear force versus displacement comparison plots. Joined after 50 μm SiC grit blast and methanol rinse.

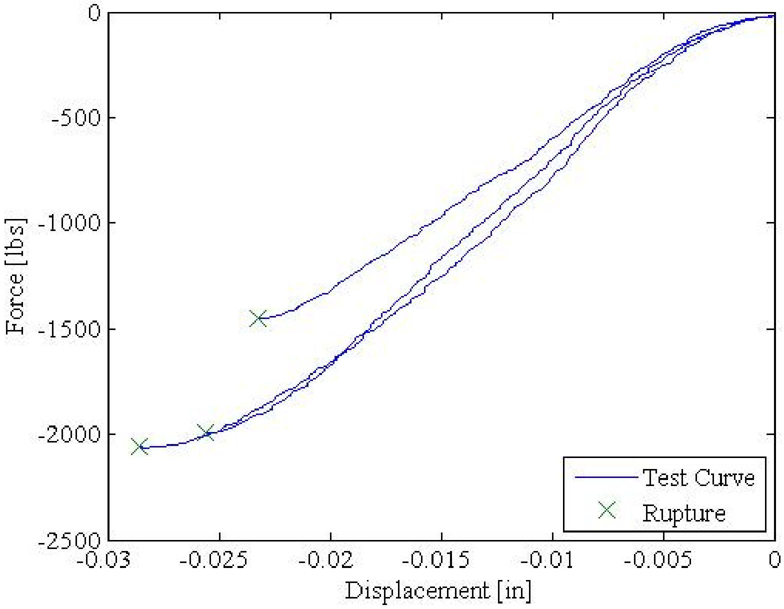

Figure C.10: USS NiTi/O1 tool steel lap shear force versus displacement comparison plots. Joined after 50 μm SiC grit blast and methanol rinse.

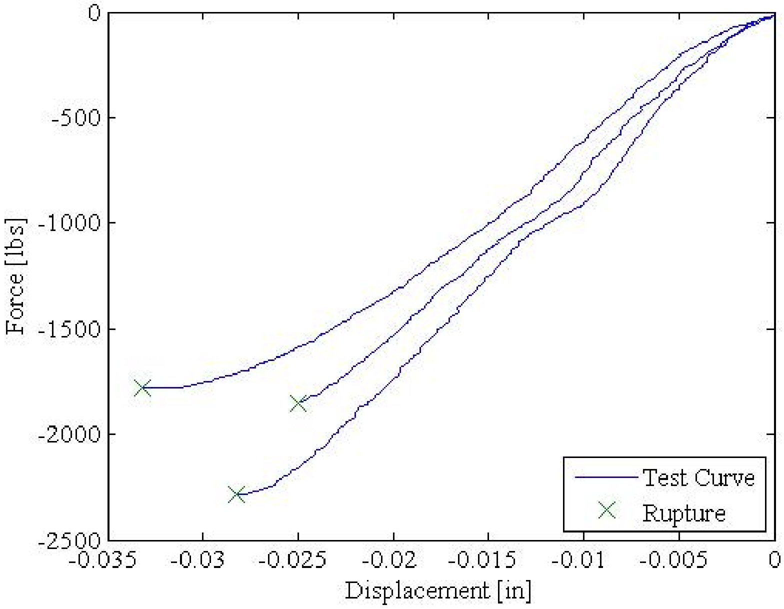

Figure C.11: USS NiTi/304 SS lap shear force versus displacement comparison plots. Joined after 50 μm SiC grit blast and methanol rinse.

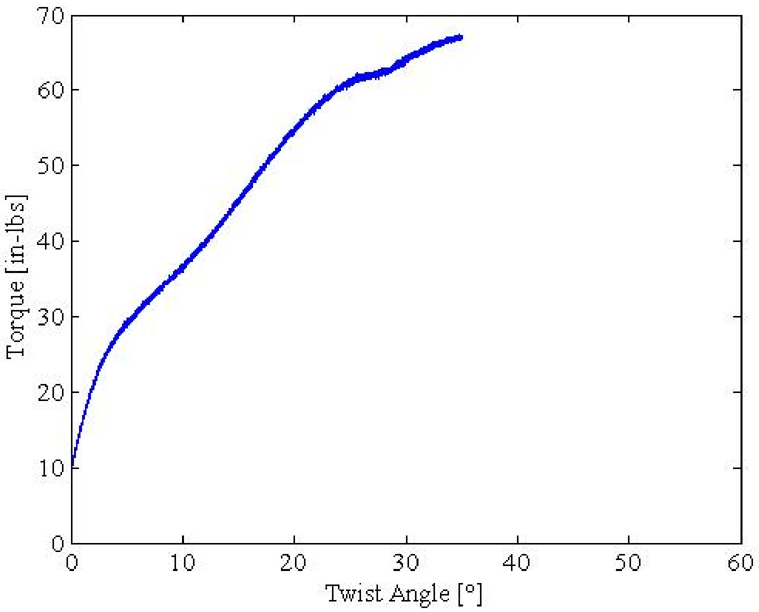

Figure C.12: USS NiTi/Al 2024 torsion joint 1 angular displacement versus torque plot 1.

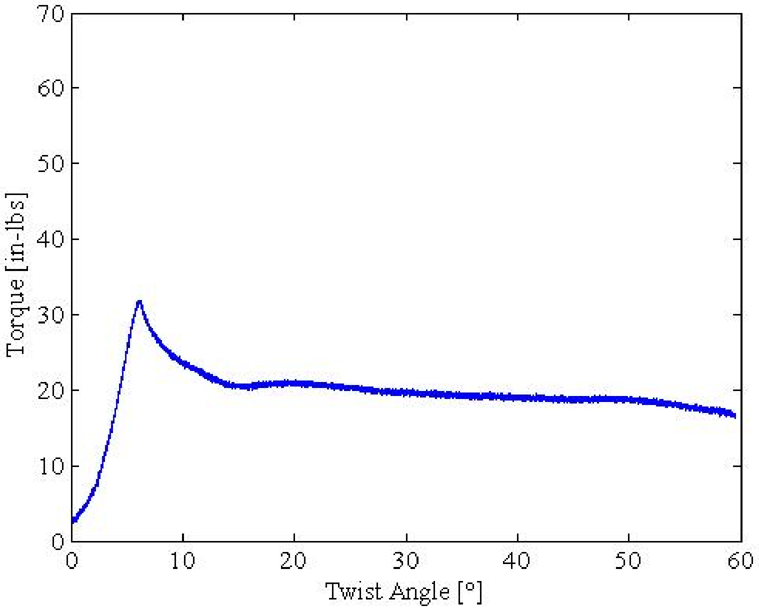

Figure C.13: USS NiTi/Al 2024 torsion joint 1 angular displacement versus torque plot 2.

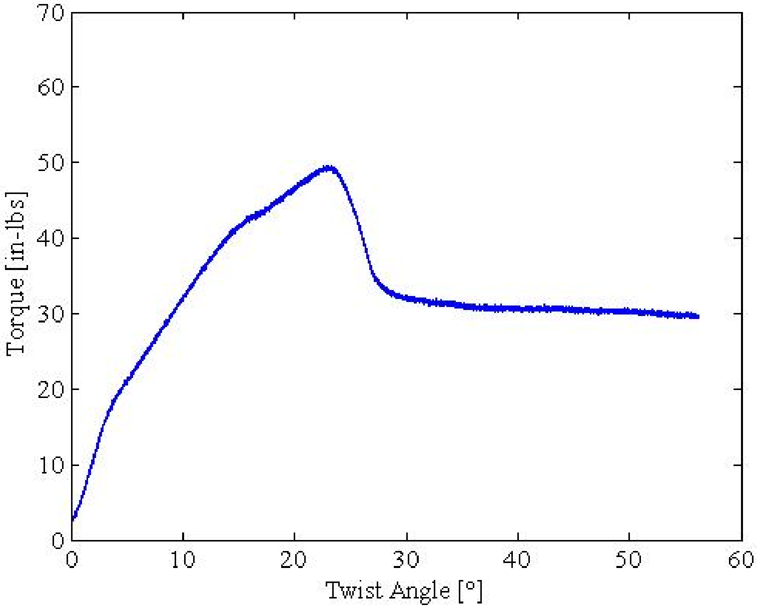

Figure C.14: USS NiTi/Al 2024 torsion joint 2 angular displacement versus torque plot.

APPENDIX D

UAM FORCE VERSUS DISPLACEMENT PLOTS

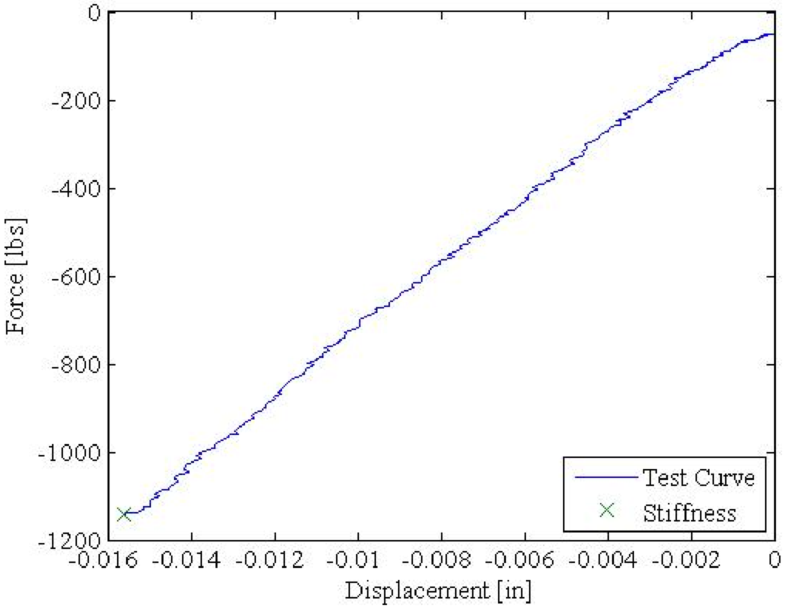

Figure D.1: UAM 1-1 sample 1 force versus displacement plot.

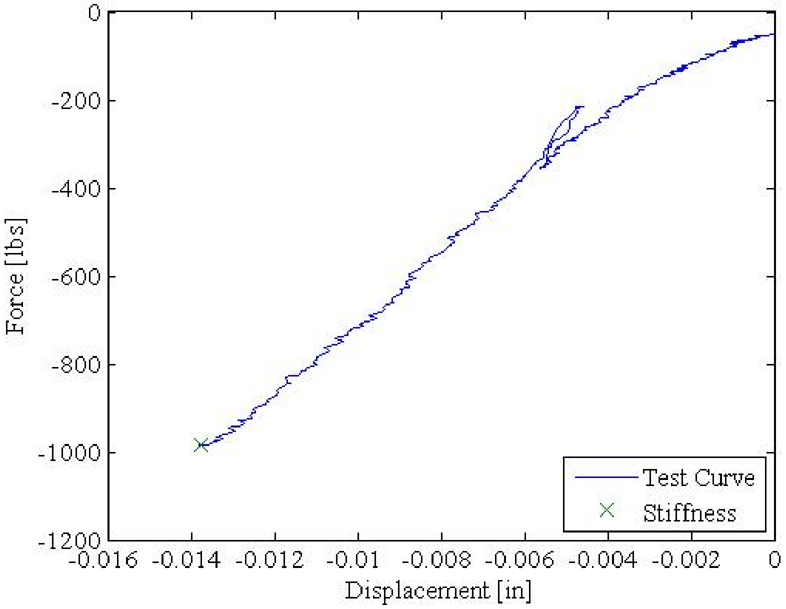

Figure D.2: UAM 1-1 sample 2 force versus displacement plot.

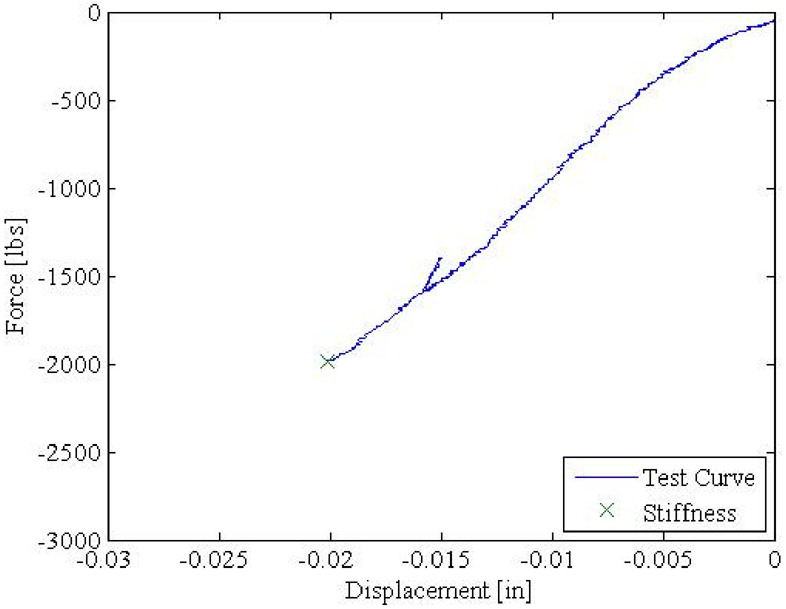

Figure D.3: UAM 1-1 sample 3 force versus displacement plot.

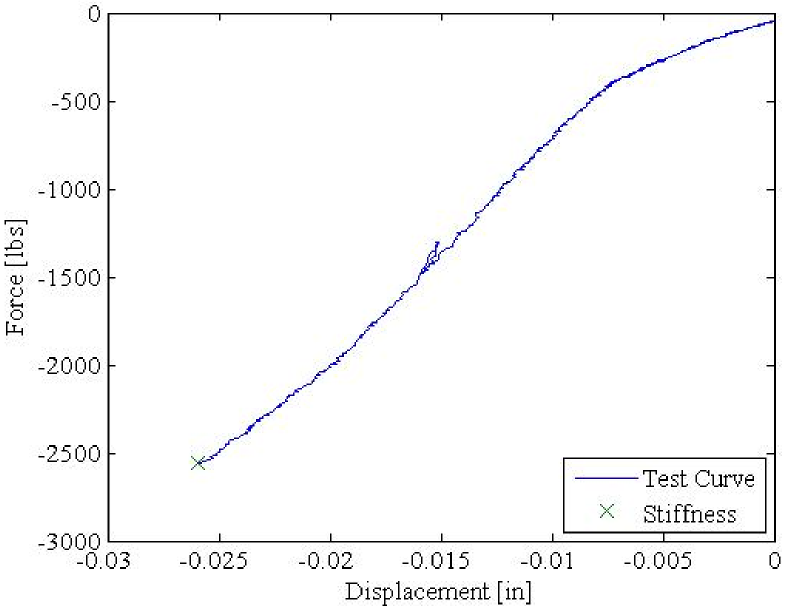

Figure D.4: UAM 1-1 sample 4 force versus displacement plot.

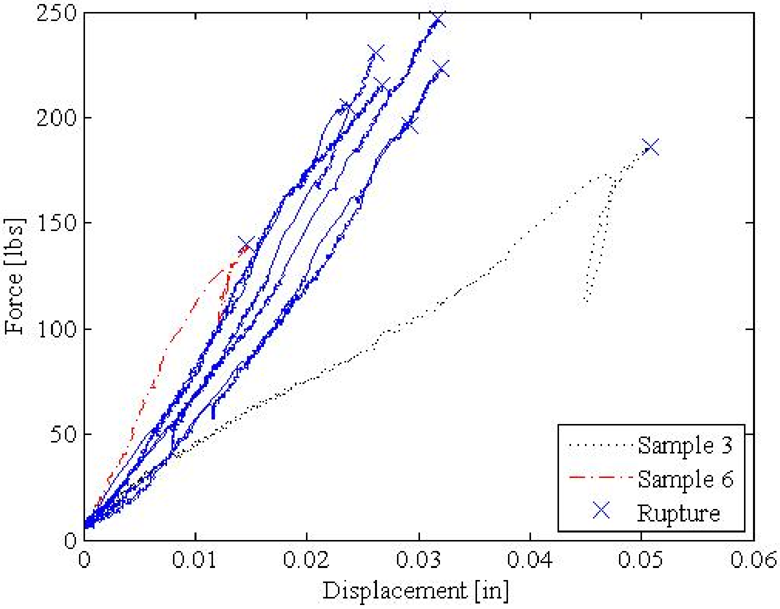

Figure D.5: UAM 3-2 force versus displacement sample comparison plots.

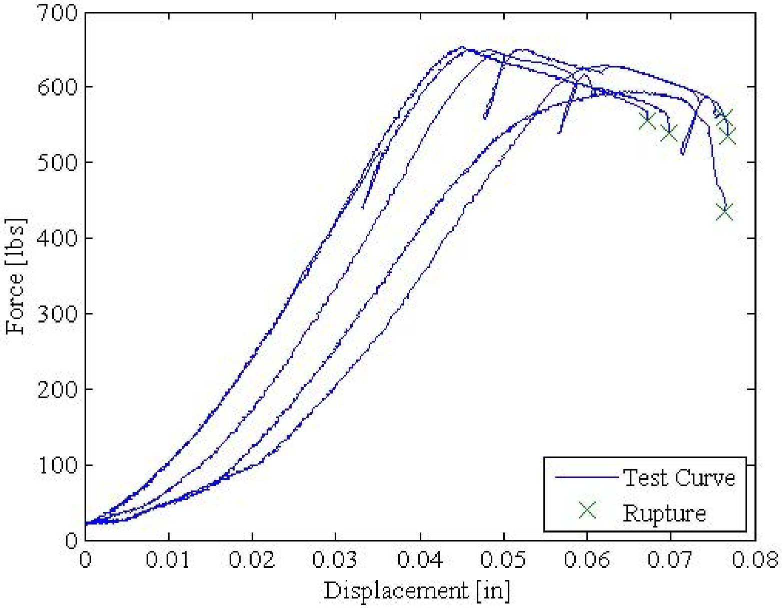

Figure D.6: UAM 1-2 force versus displacement sample comparison plots.

BIBLIOGRAPHY

[1] B. Allen. *Soldering Handbook: A Practical Manual for Industry and the Laboratory.* Iliffe Books Ltd., 1969.

[2] L. Brinson. One dimensional constitutive behavior of shape memory alloys. *Journal of Intelligent Material Systems & Structures*, 4(2):229–242, 1993.

[3] T. Clyne and P. Withers. *An Introduction to Metal Matrix Composites.* Cambridge University Press, 1993.

[4] AK Steel Corporation. 304/304l stainless steel, 2007.

[5] Erik E. Oberg, F. Jones, H. Horton, and H. Ryffel. *Machinery's Handbook.* Industrial Press, 27th edition, 2004.

[6] A. Falvo, F. Furgiuele, and C. Maletta. Laser welding of a niti alloy: Mechanical and shape memory behaviour. *Materials Science and Engineering A*, 412:235–240, 2005.

[7] K. Graff. *New Developments in Advanced Welding.* Woodhead Publishing Limited, 2005.

[8] P. Hall. US patent: Soldering alloy, December 2003.

[9] P. Hall. US patent: Composite medical device having a titanium or titanium based alloy section and a ferrous metal section, June 2005.

[10] P. Hall. US patent: Method of welding titanium and titanium based alloys to ferrous metals, April 2005.

[11] ALCOA Mill Products Inc. Alloy 2024 sheet and plate, 2009.

[12] Dynalloy Inc., 2008.

[13] Battelle Memorial Institute. Metallic materials properties development and standardization (MMPDS-04), 2008.

[14] ASTM International. A 681-08: Standard specification for tool steel alloy, 2008.

[15] K. Johnson. *Interlaminar Subgrain Refinement in Ultrasonic Consolidation.* PhD thesis, Loughborough University, Loughborough, UK, 2008.

[16] J. Kaufman. Aluminum alloy database. Knovel.com, 2004.

[17] C. Kong and R. Soar. Fabrication of metal-matrix composites and adaptive composites using ultrasonic consolidation process. *Materials Science and Engineering A*, 412:12–18, 2005.

[18] C. Kong, R. Soar, and P. Dickens. Characterisation of aluminium alloy 6061 for the ultrasonic consolidation process. *Materials Science and Engineering A*, 363:99–106, 2003.

[19] C. Kong, R. Soar, and P. Dickens. A model for weld strength in ultrasonically consolidated components. In *Proceedings of IMechE*, volume 219, pages 83–91, 2004.

[20] C. Kong, R. Soar, and P. Dickens. Optimum process parameters for ultrasonic consolidation of 3003 aluminium. *Journal of Materials Processing Technology*, 146:181–187, 2004.

[21] C. Kong, R. Soar, and P. Dickens. Ultrasonic consolidation for embedding sma fibres within aluminium matrices. *Composite Structures*, 66:421–427, 2004.

[22] M. Kutz, editor. *Handbook of Material Selection.* John Wiley and Sons, 2002.

[23] D. Lagoudas. *Shape Memory Alloys.* Science and Business Media, LLC, 2008.

[24] SAES Smart Materials. Nitinol data, 2009.

[25] H. Matsumoto. Electrical resistivity of niti with a high transformation temperature. *Journal of Materials Science Letters*, 11:367–368, 1992.

[26] US National Institutes of Health. ImageJ. Website, 2009.

[27] G. Reddy, A. Rao, and T. Mohandas. Role of electroplated interlayer in continuous drive friction welding of AA6061 to AISI 304 dissimilar metals. *Science and Technology of Welding and Joining*, 13(7):619–628, 2008.

[28] M. Sahin. Joining of stainless-steel and aluminum materials by friction welding. *International Journal of Advanced Manufacturing Technology*, 41:487–497, 2009.

[29] E. Siggard. Investigative research into the structural embedding of electrical and mechanical systems using ultrasonic consolidation. Master's thesis, Utah State University, Logan, UT, 2007.

[30] American Welding Society, editor. *Brazing Handbook.* American Welding Society, 5th edition, 2007.

[31] S. Srinivasan. EWI sonicsolder, 2009.

[32] P. Vianco. *Soldering Handbook.* American Welding Society, 2nd edition, 1999.

[33] E. De Vries. *Mechanics and Mechanisms of Ultrasonic Metal Welding.* PhD thesis, The Ohio State University, Columbus, OH, 2004.

[34] G. Wang. "Welding of nitinol to stainless steel". In *Proceedings of the International Conference on Shape Memory and Super Elastic Technologies*, pages 131–136, 1997.

[35] K. Weinert and V. Petzoldt. Machining of niti based shape memory alloys. *Materials Science and Engineering A*, 378:180–184, 2004.

[36] M. Wu. "Fabrication of nitinol materials and components". In *Proceedings of the International Conference on Shape Memory and Superelastic Technologies*, pages 258–292, 2001.

[37] W. Young and R. Budynas. *Roark's Formulas for Stress and Strain.* McGraw-Hill, 7th edition, 2002.

[38] Zhu, Fino, and Pelton. "Oxidation of nitinol". In *Proceedings of the International Conference on Shape Memory and Superelastic Technologies*, pages 258–292, 2003.

[39] P. Zimprich, A. Betzwar-Kotas, G. Khatibi, B. Wiess, and H. Ipser. "Size effects in small scaled lead-free solder joints". *Journal of Materials Science: Materials in Electronics*, 19(4):383–388, 2008.